

Dissertation in Astronomy
submitted to the
Combined Faculties of the Natural Sciences and Mathematics
of the Ruperto-Carola-University of Heidelberg, Germany,
for the degree of
Doctor of Natural Sciences

Put forward by
M.Sc. *Sladjana Knežević*
born in Zaječar, Serbia

Oral examination: 17.10.14

An Integral View of Shocks

Sladjana Knežević
Max-Planck-Institut für Astronomie

Referees: Dr. Glenn van de Ven
Prof. Luca Amendola

Zusammenfassung

Gegenstand der vorliegenden Doktorarbeit sind Balmer-dominierte Schockfronten in der Umgebung von (Super-)Novae. Diese sind durch starke Wasserstoffemissionslinien mit einer schmalen ($\sim 10 \text{ km s}^{-1}$) und einer breiten ($\sim 1000 \text{ km s}^{-1}$) Komponente gekennzeichnet. Das Studium dieser Schockfronten ist wichtig zur Verbesserung von Abstandsmessungen zu (Super-)Novae, sowie für das Verständnis ihrer Evolution, ihres Einflusses auf die interstellare Materie, und die Erzeugung kosmischer Strahlung in Supernovaüberresten. Im Speziellen werden zwei historisch bekannte Supernovaüberreste, SN 1006 und SN 1572 (Tycho), unter Nutzung hochauflöster spektrophotometrischer Abbildungen untersucht. Durch Analyse der Dispersion und Intensität der beiden $H\alpha$ -Linienkomponenten wurden Hinweise auf suprathemale Protonen – Vorläufer hochenergetischer Protonen der kosmischen Strahlung – gefunden. Sie beeinflussen die Bestimmung der Schockgeschwindigkeit und führen zur Unterschätzung des Abstandes zum Supernovaüberrest. Im Fall von SN 1572 indizieren unsere Beobachtungen eine zusätzliche mittelbreite ($\sim 100 \text{ km s}^{-1}$) Linienkomponente, was der Schockfront vorauseilende Atome impliziert. Darüberhinaus ist die schmale Komponente typischerweise breiter als die maximal erwarteten 20 km s^{-1} und zeigt oft ein Doppelmaximum, was durch vorauseilende kosmische Strahlung oder die Schockfrontgeometrie erklärt werden kann. Der letzte Teil der Arbeit beschreibt die Nutzung räumlich hochauflösende Spektrographen bei der Untersuchung von Novaüberresten, hier des klassischen Typs SH Ser. Die Weiterentwicklung von Schockfrontmodellen die nichtthermale Prozesse berücksichtigen, und ihr Vergleich mit den in dieser Arbeit präsentierten Daten, werden signifikante Fortschritte bei der Bestimmung der Eigenschaften hadronischer kosmischer Strahlung ermöglichen.

Abstract

The subject of this thesis are Balmer-dominated shocks around (super)novae. These are characterized by strong hydrogen emission lines with a narrow ($\sim 10 \text{ km s}^{-1}$) and a broad ($\sim 1000 \text{ km s}^{-1}$) component. Studying shock physics is important for improving distance estimates to (super)novae, for understanding their evolution and impact on the interstellar medium, and for obtaining insights into the cosmic ray origin in the remnants of supernovae. Two historical supernova remnants, SN 1006 and SN 1572 (Tycho), are investigated using high-resolution spectrophotometric imaging. Analyzing the widths and intensities of the narrow and broad $H\alpha$ -line components, evidence of suprathermal protons – seeds of high-energy cosmic ray protons – is found in SN 1006. Those cause an underestimation of the estimated shock velocity and, hence, the distance to the remnant. In SN 1572, our observations indicate an additional intermediate-width ($\sim 100 \text{ km s}^{-1}$) component, implying the presence of a broad-neutral precursor. Moreover, the narrow component is typically broader than the maximally expected 20 km s^{-1} and is sometimes even double-peaked, which might be due to a cosmic-ray precursor or the shock geometry. The last part of the thesis outlines how high-spatial resolution spectrographs can be used to study and better understand outflow mechanisms of novae, here of a classical nova FH Ser. Further development of shock models that include non-thermal physics, and their application to the data presented in this thesis, are expected to provide important constraints on hadronic cosmic ray properties.

To my father

CONTENTS

1	INTRODUCTION	1
1.1	CLASSIFICATION OF SNe	2
1.2	SN EXPLOSION	2
1.3	SNe TYPE Ia	5
1.3.1	CONDITIONS FOR THERMONUCLEAR RUNAWAY	6
1.3.2	EXPLOSION MODELS	8
1.3.3	PROGENITOR MODELS	9
1.3.4	OBSERVATIONAL TESTS OF PROGENITOR MODELS	10
1.4	EVOLUTION OF SNRs	11
1.5	COSMIC RAYS	13
1.5.1	CR ACCELERATION IN SNRs	16
1.5.2	OBSERVATIONAL SIGNATURES OF CR ACCELERATION IN SNRs	19
	OUTLINE OF THE THESIS	24
2	OPTICAL SHOCKS AROUND SNRs	25

ABSTRACT	25
2.1 BALMER-DOMINATED SHOCKS	25
2.2 NARROW $H\alpha$ -LINE PROFILES AND PRECURSORS	28
2.2.1 POST-SHOCK EFFECTS	29
2.2.2 PRE-SHOCK EFFECTS	29
2.3 BROAD $H\alpha$ -LINE PROFILES	32
2.4 SHOCK MODELS	33
2.4.1 VAN ADELSBERG ET AL.'S MODEL	35
2.4.2 MORLINO ET AL.'S MODELS	36
2.5 SPECTRO-PHOTOMETRIC TECHNIQUES FOR STUDYING OPTICAL SHOCKS	40
2.5.1 LONG-SLIT SPECTROSCOPY	40
2.5.2 FABRY-PÉROT INTERFEROMETRY	41
2.5.3 INTEGRAL-FIELD SPECTROSCOPY	42
2.5.4 COMPARISON OF DIFFERENT TECHNIQUES	43
2.6 SUMMARY	45
3 BDSs AROUND SN 1006	47
ABSTRACT	47
3.1 INTRODUCTION	47
3.2 INTEGRAL-FIELD SPECTROSCOPIC OBSERVATIONS AND DATA REDUCTION	48
3.3 DATA ANALYSIS	51
3.3.1 ACCURACY OF THE $H\alpha$ -LINE FITTING	54
3.3.2 HELIOCENTRIC DISTANCE TO SN 1006	57
3.4 DISCUSSION	57
3.5 SUMMARY	58

3.6	APPENDIX	59
4	BDSs AROUND TYCHO'S SNR	65
	ABSTRACT	65
4.1	INTRODUCTION	65
4.2	OBSERVATIONS & DATA REDUCTION	67
4.3	TYCHO'S 'KNOT G'	69
	4.3.1 PREVIOUS NARROW COMPONENT $H\alpha$ OBSERVATIONS OF 'KNOT G'	69
	4.3.2 $GH\alpha$ FAS $H\alpha$ OBSERVATIONS OF 'KNOT G'	70
4.4	TYCHO'S NORTHEASTERN FILAMENT	72
4.5	DISCUSSION	75
4.6	FUTURE WORK	76
4.7	SUMMARY	78
4.8	APPENDIX	79
5	BDSs AROUND CLASSICAL NOVA FH SER	85
	ABSTRACT	85
5.1	INTRODUCTION	85
	5.1.1 LIGHT CURVES AND SPEED CLASSES	86
	5.1.2 NOVA OUTBURST SPECTRUM	88
5.2	VIMOS-IFU OBSERVATIONS OF FH SER	89
	5.2.1 CENTRAL OBJECT EMISSION OF FH SER	92
	5.2.1.1 Geometry of a nova ejection	94
	5.2.1.2 Density and velocity profiles	98
	5.2.2 THE OUTER RIM EMISSION OF FH SER	102

5.2.2.1	Models of classical nova shells	103
5.2.2.2	VIMOS-IFU observations of FH Ser remnant's shell	104
5.3	SUMMARY	106
5.4	APPENDIX	107
6	SUMMARY AND OUTLOOK	109
	ACKNOWLEDGEMENTS	113
	BIBLIOGRAPHY	115

Supernovae (SNe) are one of the most fascinating and most energetic events in the Universe. They are very bright, sometimes even outshining their host galaxies. Some SNe were visible with the naked eye even during daylight. In 1572 astronomer Tycho Brache saw a sudden, very bright flash on the sky of the brightness of the planet Venus, which remained visible for the next two years. Believing that he saw a new born star, he gave it the name Stella Nuova. Today we know that SNe¹ actually represent violent deaths of stars.

These severe explosions are believed to be caused by either nuclear fusion in a degenerate star, or by the collapse of the core of a massive star. A SN launches a huge amount of stellar material into space with a velocity of order of $10\,000\text{ km s}^{-1}$, which drives a shock wave and creates a supernova remnant (SNR). The remnant nebulae are observed across almost all wavelengths. The total energy released in an explosion (10^{51} – 10^{53} erg) is equivalent to the energy radiated by the Sun during its 10 billion year lifetime. The importance of SNe is seen throughout many different phenomena in our Universe, from their role in cosmology in probing the accelerating expansion of the Universe, to understanding the chemical evolution of our Galaxy by providing elements heavier than oxygen. Also, SNe are believed to be accelerators of cosmic rays (CRs), high energy charged particles (mostly ions) that continuously strike the Earth. There is no a better way to highlight the significance of SNe than citing Carl Sagan: "The nitrogen in our DNA, the calcium in our teeth, the iron in our blood, the carbon in our apple pies were made in the interiors of collapsing stars. We are made of star stuff."

¹The name supernova was coined by Walter Baade and Fritz Zwicky in 1931.

In this Chapter, we will review the current understanding of three important and still open questions in the field of SNe:

- What are the progenitors of SNe?
- What is the explosion mechanism?
- Where and how are CRs produced in SNRs?

1.1 CLASSIFICATION OF SNE

SNe are traditionally divided into two major groups: type I and type II (SNe I and SNe II later in the text). The spectra of SNe I lack hydrogen lines, while these lines are present in the spectra of SNe II² (see Figure 1.1). The two SNe types have different light curves: whereas SNe I light curves exhibit sharp peak with a steep post-maximum decline, while less sharp peaks and more gradual decrease after the maximum are characteristic for SNe II (Figure 1.2). These two major groups are divided into more refined spectroscopic and photometric subclasses. In the first weeks after the explosion, the spectra of SNe Ia exhibit strong absorption silicon lines at 615 nm, SNe Ib show strong helium lines, whereas SNe Ic lack both hydrogen and helium lines. SNe II are very diverse group. They can be divided into two photometric subclasses: SNe II-L with the light curves decreasing almost linearly after the maximum, and SNe II-P having the plateau as a consequence of the hydrogen recombination in their expanding envelopes. Moreover, there are SNe Iib which show little presence of hydrogen in the spectra, and SNe IIn with the presence of narrow emission lines, which links them to SNe Ia that interact with the circumstellar material. At first, this classification of SNe was purely empirical. It was later on related to different explosion mechanisms, where it was believed that thermonuclear explosion is the common mechanism for type I and gravitational collapse of very massive stars, i.e., core-collapse for type II SNe (see Section 1.2). The current theory relates SNe Ia to thermonuclear explosions of white dwarfs in close binary systems, while all type II and Ib and Ic SNe are linked to core-collapse SNe.

1.2 SN EXPLOSION

Depending on the masses of their progenitors, stars can evolve into one of the three final stages: white dwarf (WD), neutron star and black hole. If the core stellar mass at the end of the main sequence phase is lower than the Chandrasekhar (Ch) mass ($\lesssim 1.4M_{\odot}$), a WD will be formed. In

²This classification is based on the early (within few weeks after the explosion) spectra.

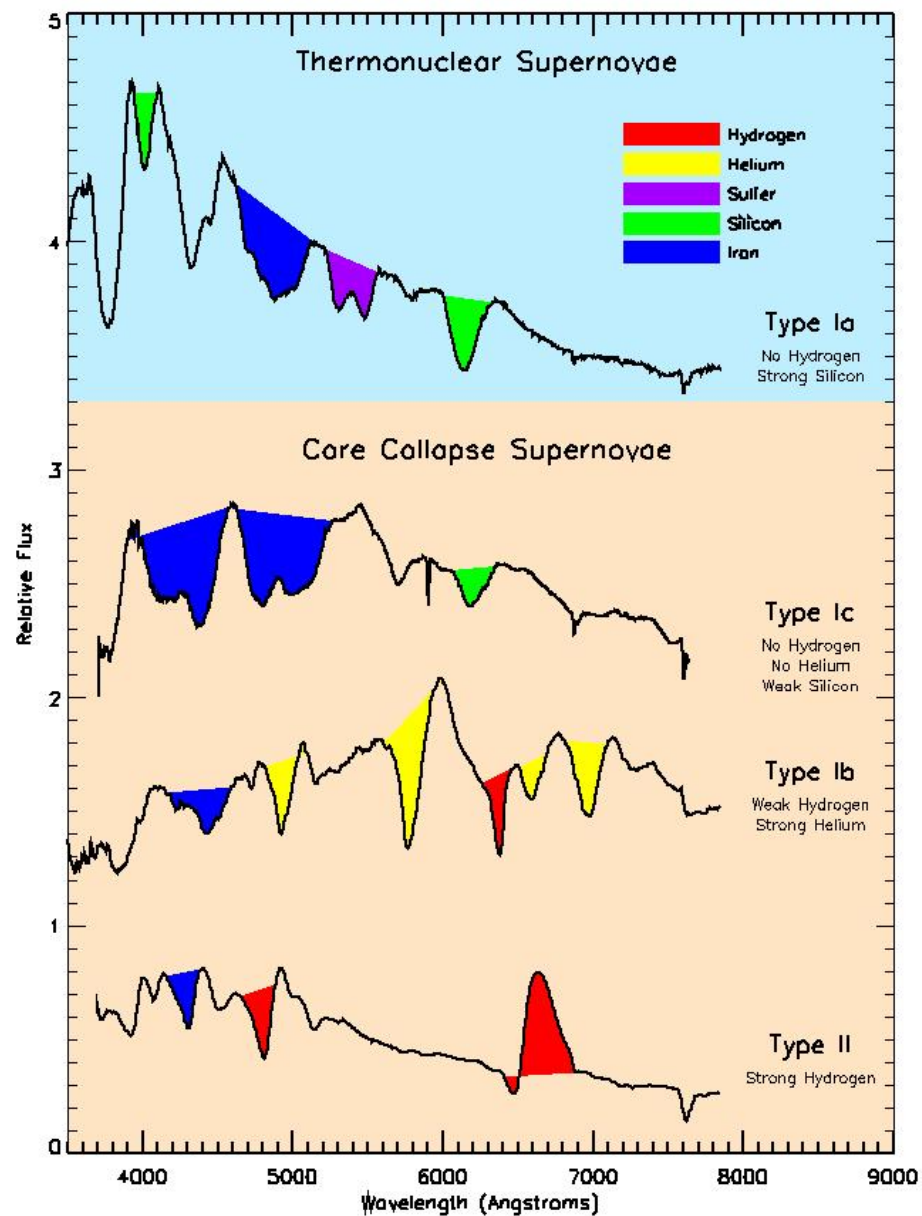


Figure 1.1: Spectral classification of SNe with the clear indication of their characteristic features. Type Ia shows strong silicon lines, type Ib strong helium lines while they are less or not prominent at all in the type Ic. Strong hydrogen lines are characteristic for type II SNe. Credit: <http://supernova.lbl.gov/~dnkasen/tutorial/>.

case the mass is higher than the Ch limit, but lower than Oppenheimer-Volkoff limit ($\lesssim 3M_{\odot}$), the star will create a neutron star. In the case when the mass is higher than the Oppenheimer-Volkoff limit, we will have the formation of a black hole. It is widely believed that gravitational collapse of the most massive stars and the formation of some neutron stars and black holes

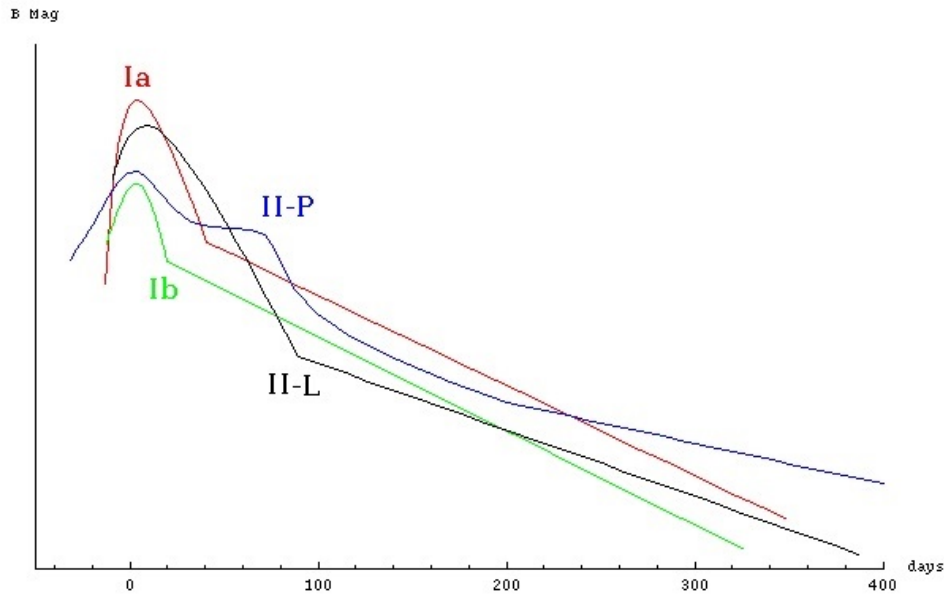
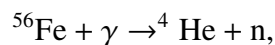


Figure 1.2: SNe light curves for types Ia, Ib, II-L and II-P shown according to the blue magnitudes. SNe I have sharper peaks and steeper luminosity decline after the curve maximum than SNe II. Credit: Filippenko (1997).

are followed by a SN explosion. However, SN explosion can also happen to WDs in close binary systems (CBSs) which together with the former imply two different mechanisms of the SN explosion: gravitational collapse and thermonuclear explosion.

The explosion mechanism of massive stars is **gravitational collapse** of their non-degenerate cores. When the nuclear burning in the core reaches a critical mass (Ch limit) of iron, the most stable element, nuclear fusion can not produce enough energy to stop the core collapse. The temperature continues to increase and becomes very high ($\sim 10^{10}$ K) so that the iron starts photodissociation (Fowler & Hoyle 1964)



and electrons and protons combine into neutrons creating a very dense core, which makes its contraction to start slowing down. The outer layers of a star, where the collapse is still happening, fall on the core and bounce off creating the wave which becomes a shock while propagating through the low dense medium. Thermonuclear reactions start on the shock front as well as behind it and eventually blow apart the star, releasing its gravitational energy in the form of neutrinos ($\sim 10^{53}$ erg) and the kinetic energy of the outer layers ($\sim 10^{51}$ erg). In superdense cores created in a gravitational collapse matter becomes nontransparent for neutrinos which are then absorbed by the core and increase its temperature until the neutronization starts. Colgate &

White (1966) proposed a neutrino-transport process where neutrinos give the energy to the core's envelope and cause the bounce and SN. A modification of this theory given by Woosley & Weaver (1986) is better known today as delayed detonation. However, the process of transformation from implosion to the explosion of the core is still matter of debate.

Thermonuclear (TN) explosion, originally proposed by Hoyle & Fowler (1960) as an explosion mechanism for the SN type Ia, considers deflagration of a carbon-oxygen (CO) WD in a CBS. When one of the stars in a CBS has already evolved into a WD, it will start accreting material from its companion and forming the accretion disk once the companion leaves its main sequence phase and fills the Roche's lobe. Mass accretion increases the pressure and temperature in the shell on the WD surface, TN reactions start and eventually blow off the accretion disk. This mechanism explains the classical and recurrent novae. If the accretion is fast and WD is massive enough so that accretion can drive its mass close to the Ch limit, gravitational collapse in the core increases temperature, initiate first carbon and then oxygen burning, and TN explosion destroys the whole star. The outward nuclear burning front forms heavy nuclei, in particular nickel Ni which decays as



This decay explains the characteristic light curves of SN Ia, i.e. its Ni peak and Co tail.

Unlike core-collapse SNe, SNe Ia are modest sources of UV radiation and do not significantly ionize the interstellar medium (ISM). The research presented in this thesis focuses on studying optical shocks around SNe Ia which show dominant Balmer lines of hydrogen atoms (see Chapter 2). Therefore, we will review SNe Ia explosion physics and progenitors furthermore.

1.3 SNE TYPE IA

Unlike SN explosions of massive stars which end their lives close to their birth places, SNe Ia often appear far from the the star forming regions and in elliptical galaxies where extinction is lower. As explosions of WDs with Ch mass, they should be homogeneous phenomenon and about the same luminosity ($\sim 5 \times 10^9 L_{\odot}$). The high luminosities and relatively low scatter in light curves make SNe Ia best cosmological distance indicators. As such, they are used for determining cosmological parameters which led to the discovery of accelerating expansion of the Universe caused by yet unknown source called dark energy (Riess et al. 1998; Perlmutter et al. 1999). Next, SNe Ia are important for studying galactic chemical evolution as they are main contributors of iron to their host galaxies.

SNe Ia appear in young, but also old stellar populations implying a time delay between star formation and SN explosion. Observations reveal that luminosities of SNe Ia differ in different populations, with more luminous SNe in young and less luminous SNe in old populations. Super-luminous SNe Ia occur in metal poor environments with low mass host galaxies, while sub-luminous SNe Ia occur in non star-forming host galaxies with large stellar masses, such as elliptical galaxies. The SNe Ia birthrate in galaxies is convolution of the delay time distributions with the star formation history. The observed birthrate in the Milky Way is around $3 \times 10^{-3} \text{ yr}^{-1}$ (Cappellaro & Turatto 1997) and can be used to constrain the progenitor models of SNe Ia. There are two favored progenitor models: single degenerate (SD), where the core accretes material from a non-degenerate companion, and double-degenerate (DD), where two CO WDs merge having total mass larger than Ch limit. It turns out that the DD model can pretty easily explain the observed birthrates, while SD models account for only 2/3 of the observations (Wang & Han 2012). Among all, SNe Ia are known as accelerators of CRs which is of particular interest of this research and will be explained later (Section 1.5).

1.3.1 CONDITIONS FOR THERMONUCLEAR RUNAWAY

As mentioned above, TN reactions can trigger shock waves which drive the CO WD apart and produce SN Ia. This explosive event requires the temperature ($T \approx 10^9 \text{ K}$) where the energy generation rate becomes equal to the heat conduction rate – a situation called a TN *runaway*. However, a WD experiencing runaway can not only result in a SN Ia, but also in a *nova*, where the runaway takes place only in the outermost layers that have been accreted from a companion donor star in a CBS, and not in the entire WD. Whether a nova or SN Ia will occur is determined by the physical conditions of the system: the WD mass and luminosity, as well as the composition of the accreted material and the rate at which it is accreted. For example, for a SN Ia to occur, the WD needs to reach the Ch -mass limit, and requires specific conditions to avoid a nova outburst at earlier times. The properties of the WD and its accreted envelope also affect the onset time, energy production and other details of the TN reaction. We will elaborate on them in what follows.

Mass of a WD defines the amount of the accreted material which is inversely proportional to the WD's mass when all other parameters remain constant. A less massive WD has a smaller surface gravity which is responsible for compressing and heating the bottom layers of a newly formed accreted envelope. Weaker surface gravity implies lower gas degeneracy and the temperature may not even reach 10^8 K and TN runaway cannot be triggered. On the other hand, a high mass WD reaches faster the critical pressure that balances the radiation pressure, i.e., TN runaway can start with lower critical mass of an envelope.

$$P_{\text{crit}} = \frac{GM_{\text{WD}}M_{\text{crit}}}{4\pi R_{\text{WD}}^4} \sim 10^{20} \frac{\text{dyne}}{\text{cm}^2}$$

However, smaller critical mass can easily lead to a nova outburst instead of an SN explosion.

WD luminosity is also very important since the heat from the underlying WD also heats the nuclear burning layers. Lower luminous WD (cooler WD's interior) less efficiently heats its accreted envelope delaying the start of nuclear reactions, and WD can accrete more material. High luminous WD (hotter interior) initiates nuclear burning easier, the amount of the accreted material becomes smaller, and an outburst occurs earlier with a smaller ejected mass as a result. For a narrow range of luminosity values (near $10^{37} \text{ ergs}^{-1}$), the accretion rate can become equal to the burning material rate and we will have steady burning of hydrogen. No TN runaway would occur, no mass would be lost in an outburst, and the WD's mass could grow to Ch-limit (van den Heuvel et al. 1992) becoming a candidate for a SN Ia progenitor.

Chemical composition of the accreted material constrains opacity in the nuclear burning region. More metal rich accreted material will increase the opacity, more heat is trapped in this region, and the temperature increases faster. Lower metallicity of accreted material reduces opacity, increases the rate of radiative heat transport out of the nuclear burning layers implying very slow temperature growth in those layers. This would lead to a more massive accreted envelope and a more violent explosion eventually. Also, mixing of accreted material with WD's core material during the accretion process is important because it increases metallicity and opacity in the burning layers.

The reactions important in powering TN runaway are p-p chain and CNO cycles. These reactions are characteristic for different stages of the TN runaway. WD spends most of the time in the accretion phase during which hydrogen is burned in p-p chain when the temperature is around 10^7 K . CNO and hot CNO cycles are characteristic for the final stages of TN runaway. With temperature increase to around 10^8 K burning reactions of carbon and oxygen start, and thus CNO cycle. In CNO cycle we have two types of reactions, proton capturing with the strong dependence on temperature and β^+ decay independent of temperature. At lower temperatures β^+ decay dominates, where the produced energy depends only on half-lives of the unstable nuclei and the initial number of C, N, O, Ne, Mg in the envelope. For temperatures much higher than 10^8 K , proton capture starts to dominate and we have transition to hot CNO cycle through nitrogen-proton capture which leads to heavier element production. After the ignition of TN runaway, one has to include into calculations convection which can bring unstable β^+ nuclei to the envelope surface before their decay. In the very beginning the envelope is very thin and convection is unimportant. Energy released from β^+ decays helps the ejection of the material. Depending on the enrichments the released energy at the surface can be from 10^{13} to $10^{15} \text{ erg g}^{-1}\text{s}^{-1}$.

1.3.2 EXPLOSION MODELS

It is still unclear how (super)nova explosion happens, because it is computationally very hard to include the contribution of all physical processes of interest, especially since most of those processes, i.e., nucleosynthesis, radiation transport, convection and shock physics, are very complex. There are some suggested models (Hillebrandt & Niemeyer 2000) that seem to be able to reproduce SNe Ia spectra, light curves and nucleosynthesis. All the models are based on two mechanisms, **deflagration** and **detonation**. The strength of thermal pressure created by nuclear burning sets the difference between them. Very high thermal pressure forms shock wave which is generally supersonic, and ignites the fuel by compressional heating. This form of a shock is called detonation. Its speed depends on the energy released per unit mass. On the other hand, very weak thermal pressure would create subsonic shock, called deflagration. In this case, we have a combustion front that heats up the fuel before it is overrun by a thin reaction layer where the fuel is consumed and energy generated. Unlike detonation, deflagration allows the medium to expand before it is burned, and therefore turbulent velocity fluctuations of the fuel may strongly affect deflagration itself. It is unclear where exactly flame ignition happens and whether there are multiple ignition points. The flame is expected to form once the burning time scale becomes much smaller than the convection time scale, which happens at $T=1.5\times 10^9$ K when C and O burn instantaneously. Convective process which is assumed to cause net cooling and delay thermonuclear runaway is the so called URCA process. When ion's nucleus absorbs a lepton, the whole system can be convectively transported away from the star's core and suffer β decay by emitting neutrino. Convection then carries the element back to the core and the process repeats many times. The ignition outside the central core, i.e., at many unconnected points, is believed to produce more intermediate mass elements (IME) which are required to explain the light curve peak.

Considering two mentioned mechanisms, there are four explosion models suggested. First, we have **prompt detonation** where supersonic wave destroys the whole star. However, it fails to produce enough IME due to no pre-expansion prior burning and CO are almost completely burned into iron-peak group elements. Also, fast **pure turbulent deflagration** overproduces neutron rich iron-peak group elements, while slow would not even cause a runaway. Even multipoint ignition where more material burns at lower densities and more energy is released, can not successfully reproduce the observations. The most favored scenario is **delayed detonation**, where we have turbulent deflagration transition to detonation. It occurs in the late phase of a Ch-mass WD explosion, where we first have a slow flame, with the velocity of 1% of the sound speed, which pre-expands the star, and then change to a supersonic combustion front around density of 10^7 gcm⁻³ which produces the required amount of IME. So far, this is the only model which satisfies all the constrains given by SN Ia spectra, light curves and nucleosynthesis. The fourth model, **double detonation** model, where the accreted hydrogen burns into helium causing the

envelope detonation, and later on we have detonation of a sub-Chandrasekhar CO WD, was first proposed by Taam (1980) and Nomoto (1982). However, it is still unclear if this model can successfully reproduce SN Ia properties. It is also important to say that we have considered here only models which can reproduce normal SN Ia spectra, i.e., models based on Ch mass limit. Some mentioned models might be able to explain sub-luminous SN Ia for example, which are order of magnitude fainter than normal SN Ia, and thus need less IME produced.

1.3.3 PROGENITOR MODELS

Even though SNe Ia are believed to be TN explosions of CO WDs when they reach a mass near the Ch limit, the nature of the progenitors is still unclear. SD and DD are two possible scenarios.

In the **SD scenario** (Whelan & Iben 1973) CO WD in a close binary system (CBS) accretes material from a non-degenerate companion. This scenario leaves three different possible channels of accretion:

- *WD+He star channel* where a WD accretes He-rich material from a He star. Short time delays of less than 0.1 Gyr seems to be well explained by this channel.
- *WD+MS channel* where a WD accretes H-rich material from a main sequence (MS) star or a star slightly evolved away from the MS. This channel well explains 0.1–1 Gyr time delays.
- *WD+RG channel* where a donor star is a red giant (RG). This channel explains time delay greater than 1 Gyr.

Increasing the mass of a WD by accretion is, actually, not an easy task. It works only for a very narrow parameter range in which WD can accrete material and burn it in a stable manner. The process depends on the mass-transfer rate and its evolution with time. Too low mass-transfer rate can cause unstable nuclear burning that eventually leads to a nova explosion where all accreted material is ejected. On the other side, if the rate is too high, i.e., a WD cannot accrete all the material transferred from the donor star, the system will enter into a common envelope (CE) phase where most of the transferred mass will be filling and overflowing the WDs Roche lobe. Now the friction between the immersed binary and the envelope will make the stars spiral towards each other until enough orbital energy has been released to trigger a disk-like outflow (Paczynski 1976). The spiral-in phase is not long enough for sufficient matter accretion by the WD. In order to enlarge the parameter space for producing SNe Ia and avoid CE phase, it is assumed that non-accreted material is lost from the binary system in an optically thick wind. However, this

assumption requires a low-metallicity threshold of $Z \approx 0.002^3$ that has not been found in observations.

In the **DD scenario** (Iben & Tutukov 1984) a SN explosion is a result of two CO WDs (in some cases even three, e.g., Eta Carinae) where the total mass of the merger product is equal or larger than the Ch mass. The lack of H and He emission in the spectra of SNe Ia is easily explained by this model. Also, the predicted merger frequency is quite high and corresponds to the observed SNe Ia birthrate (Badenes & Maoz 2012). Two CO WDs orbiting each other cause a periodic distortion of the spacetime continuum around them, i.e., generate a gravitational wave. A gravitational wave carries energy and angular momentum away from the binary system causing a shrinking of their orbit. When the less massive WD fills its Roche lobe, it forms a disk around the more massive WD before being accreted. The problem with this model is that TN reactions may start at the disk-dwarf interface forming a carbon-burning front that propagates inward. This may transform CO into O-Ne-Mg which then collapses and form a neutron star by electron capture on ^{24}Mg . Also, relatively wide range of allowed WD masses are not favored in explaining similarities between most SNe Ia.

1.3.4 OBSERVATIONAL TESTS OF PROGENITOR MODELS

Detection of circumstellar material (CSM) is believed to reveal the nature of the progenitor systems. While both, SD and DD models, can end having a CE phase and eject CSM, the presence of hydrogen lines in the spectrum is expected only in the SD model, and thus the presence of these lines can unambiguously set the difference between the two progenitor models. It is important to say that the way to distinguish CSM and ISM spectra is by looking into time-variability of line strengths, where one would expect no or negligible variation in the case of ISM, and an increase in line strength with time for CSM. The existence of CSM itself is traced mostly through narrow NaID absorption lines. High optical spectral resolution of Palomar Transient Factory (PTF) has discovered a complex circumstellar environment of SN PTF 11kx. Blueshifted ($\sim -65 \text{ km s}^{-1}$), narrow ($\sim 10 \text{ km s}^{-1}$), absorption lines of NaID, FeII, TiII, HeI, and hydrogen Balmer lines were detected in its CSM (Dilday et al. 2012). Recent Silverman et al. (2013) late-time spectral observations (124–680^d past the maximum) has confirmed that PTF 11kx is SNe Ia with a strong CSM interaction, and argued to arise from a symbiotic nova progenitor, i.e., SD model.

Best confirmation of the SD model would be discovery of the companion (mass-donor star) in the area of explosion. This expectation is supported by simulations of SN ejecta interaction with the companion star (Pakmor et al. 2008; Liu et al. 2012). The potential companion should be at the

³For a lower metallicity than this threshold, the optical depth of the wind is small and the binary system goes through a CE phase before reaching Ch mass.

distance of the remnant, moving away from its center with an enhanced velocity, gained from the orbital velocity in the binary system before the explosion. The companion's spectrum might also show signs of the iron-peak elements enrichment from the supernova ejecta, but also an increase in its luminosity over time would be expected. Ruiz-Lapuente et al. (2004) might have found a companion star of Tycho's SNR (SN 1572), a subgiant star Tycho G (G2IV). The potential companion is at the same distance as the remnant, close to its center, with the radial velocity well above the typical ones ($\geq 30 \text{ km s}^{-1}$) for the distance of the remnant, and with a high proper motion. Later on González Hernández et al. (2009) reported a Ni surface enrichment of the same star. However, as argued in Kerzendorf et al. (2009, 2013), all the observed characteristics do not exclude that Tycho G is just a star passing by, but the probability for something like that is very low (Bedin et al. 2014). The extensive search for companions of the remnant SNR 0509-67.5 in Large Magellanic Cloud (Schaefer & Pagnotta 2012; Edwards et al. 2012), and the remnant SN 1006 in our Galaxy (González Hernández et al. 2012; Kerzendorf et al. 2012) reported on no surviving companion found so far.

Kinematic and morphological properties of the evolved remnants can also provide information on their progenitors. Density, temperature and ionization structure evolution of remnants can be estimated by performing simulations of different SN ejecta profiles, i.e., different explosion mechanisms, interacting with the ISM. Kepler's SNR (SN 1604) with a substantial nitrogen overabundances (compared to solar abundances) in its northeastern rim suggests the existence of a shell created in a mass outflow during the binary system evolution (Blair et al. 1991). The existence of a massive shell is further supported with the measurements of lower expansion parameters in that region compared to the other parts of the remnant. Chiotellis et al. (2012) suggested that the Kepler's SNR progenitor is a wide symbiotic binary system consisting of a CO WD and a 4–5 M_{\odot} asymptotic giant branch (AGB) donor star, where a part of the slow wind of a donor star has been accreted onto the WD while the rest of the wind formed the observed nitrogen-rich shell.

1.4 EVOLUTION OF SNRS

A SN injects material at velocities of $\sim 10^4 \text{ km s}^{-1}$, which expands supersonically into the ambient medium creating a shock around the SN. Once the shock wave is created, a SNR is formed. Before it is overrun by the shock, the upstream⁴ gas is unable to respond to the induced supersonic pressure disturbance. When it is overtaken by the shock, it is compressed, heated and accelerated. The transition layer where the upstream bulk energy dissipates into the heat downstream is called

⁴Upstream refers to the region in front of a shock (pre-shock), and downstream to the region inside the shock (post-shock).

the shock front. According to jump (Rankine-Hugoniot) conditions, based on mass, momentum and energy conservation, temperature, density and bulk velocity experience discontinuous jump while crossing the shock front. The Mach number $M = V_s/c_{s1}$, where V_s defines the shock velocity and c_{s1} the upstream sound speed, defines the magnitude of the jump⁵. Since the ISM is magnetized, we shall use the magnetosonic Mach number instead, which is defined as $M_s = V_s/\sqrt{c_{s1}^2 + V_{a1}^2}$, where V_{a1} is Alfvén velocity. For $M_s \gg 1$ and an ideal gas ($\gamma=5/3$), the upstream gas will be compressed by a factor $r = \rho_2/\rho_0 = 4$ (Drain & McKee 1993) in the post-shock region, and has a temperature of

$$T_2 = \frac{3\mu m V_s^2}{16k},$$

where ρ_2 and ρ_0 are post- and pre-shock gas densities respectively, and μm is an average particle mass. In the rest frame of the post-shock gas, the pre-shock gas has bulk velocity of $3V_s/4$.

The morphology of young⁶ SNRs is dominated by the amount of matter and energy ejected in the explosion, while interaction with ISM shapes older SNRs. According to the remnant shape and spectral index, we have shell remnants with the spectral index of $\alpha \approx 0.5$, plerions or centrally filled remnants with the spectral index of $\alpha \approx 0.2$, and composite remnants as combination of these two. Looking into radio spectrum, there is an obvious difference between shell remnants and plerions. The radio emission in the case of shell-like remnants comes from the region just behind the shock wave, while plerions show synchrotron radio emission from the central part of the remnant due to effect of a pulsar wind from the central source, i.e., neutron star.

Remnants are also grouped according to their optical spectra: B-remnants dominated by Balmer lines are associated to SNe Ia (van den Bergh 1988); O-remnants that show strong oxygen lines in the interaction of the blast wave and circumstellar material, and are linked to the massive O or Wolf-Rayet (W-R) stars; P/C-plerions related to massive B stars which optical spectrum is supported by a pulsar in their centers.

Regardless the type of SN, the remnant goes through four evolutionary phases:

1. **The free-expansion phase** (Chevalier 1982) where a shock wave expands freely with a nearly constant velocity of $\sim 10\,000 \text{ km s}^{-1}$, and its radius evolves linearly with time ($R \propto t$). The remnant's dynamics in this phase is defined by the explosion parameters, i.e., the energy and the amount of the material ejected. Duration of this phase is $\sim 1000 \text{ yr}$.
2. Once the shock wave overruns more ISM material than ejected in the explosion, the SNR enters the **adiabatic or Sedov phase** (Sedov 1959). Comparing to the initial energy released in explosion, radiative cooling is still negligible and does not influence shock dy-

⁵Shock wave is supersonic, meaning that $M > 1$.

⁶A SNR is called young if it is in a free expansion or Sedov-Taylor evolutionary phase (see below).

namics in this adiabatic shock. The remnant expands adiabatically, i.e., energy is conserved inside the remnant and we have a hot interior of $T_2 \sim 10^6$ K. The remnant's radius is defined as $R \sim (E_0/\rho_0)t^{2/5}$, where E_0 is the initial explosion energy and ρ_0 the ambient density. The shock velocity drops to ~ 2000 km s⁻¹. The boundary between the swept-up and unshocked ISM is called the forward shock. Deceleration, initiated in this phase, of the expanding ejecta creates a second shock (reverse shock) moving inwards with respect to the forward shock. The reverse shock heats and ionizes the dense, metal enriched material which then shines in X-rays. The region between shocked ISM and shocked ejecta is separated by a contact discontinuity. The remnant spends most of its evolution in this phase ($\sim 10^6$ yr).

3. When the temperature behind the shock drops below 10^6 K, strong radiative cooling takes place and the remnant enters the **radiative or snow plow phase**. Conservation of energy does not hold anymore, but instead we have momentum conservation. When the temperature gets close to 10^5 K, radiative cooling through He and intermediate to low ionization stages of C, N, O dominates. Being a bright strong source of UV and optical flux with prominent emission lines, radiative shocks can provide estimates of shock velocities, pre-shock densities and abundances. In this phase, the SNR radius changes with time as $R \propto t^{1/4}$.
4. **Dissipative phase** is the last phase in a SNR evolution. Once the shock velocity becomes lower than the sound speed in the ambient medium, the remnant loses its identity and assimilates with the surrounding ISM.

1.5 COSMIC RAYS

CRs are energetic charged particles traveling with the speed of light, consisting of about 99% of atomic nuclei and 1% of electrons. Protons are most abundant among nuclei ($\approx 89\%$), followed by He nuclei, i.e., α particles ($\approx 10\%$) and the rest ($\approx 1\%$) consist of the heavier nuclei. The origin of CRs is diverse. They can originate in the solar neighbourhood, from galactic and even extragalactic sources. The sources of CRs anticorrelate with the CR direction detected on the Earth due to their deflection by the Galactic, interstellar and interplanetary magnetic fields. Therefore, the potential sources of CRs are traced by the electromagnetic radiation, often by radio synchrotron and non-thermal X-ray emission from CR *electrons* in the magnetic field, and also γ -ray emission from CR *electrons* and CR *protons*.

CRs collide with atmospheric molecules at an altitude of about 10–50 km and produce a cascade of secondary particles (air shower) – pions, which decay to muons, neutrinos and γ -rays that fur-

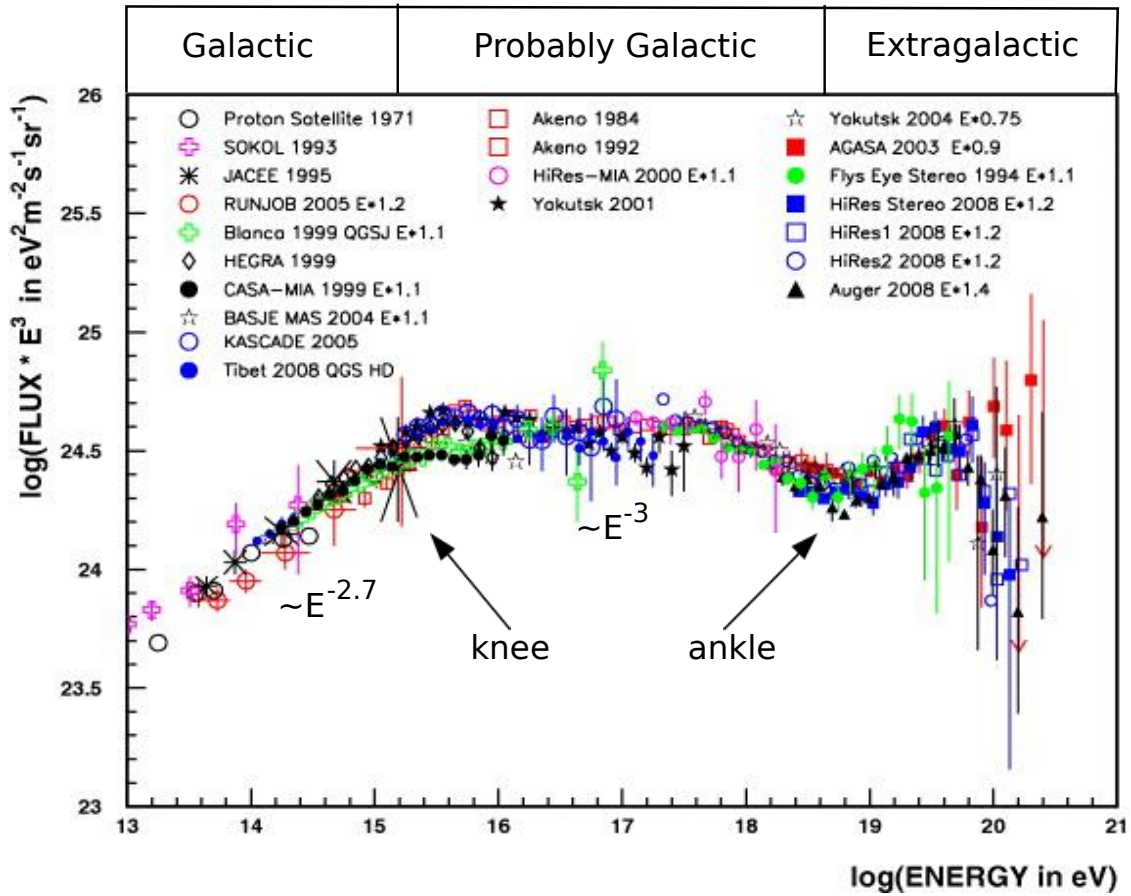


Figure 1.3: Shown is CRs flux, scaled by an energy dependent factor of E^3 , as a function of their energies in the range 10^{13} to 10^{20} eV. The points show measurements from different experiments as indicated in the plot. The slope of the spectrum for the energies up to 10^{15} eV (the 'knee') is well approximated by the slope index of -2.7, while the index of -3 best explains the spectrum in the energy range 10^{15} eV– 10^{19} eV (the 'ankle'). CRs with the energies up to 10^{18} eV are believed to originate within the Galaxy, and the ones with higher energies are supposed to originate from extragalactic sources. The plot is adapted from Nagano (2009).

they produce electrons and positrons in their collisions with the air atoms, and form an extended shower of particles. By studying the secondary particles in the air showers, the energy of CR particles can be determined within an uncertainty of about 30%. The CR energy spectrum shown in Figure 1.3 illustrates the flux of particles per unit time, area, solid angle and energy interval. The low-energy CRs with energies up to 10^{11} eV are most frequently detected, i.e., every second per square meter. The number of CRs with energies up to 10^{15} eV is moderate, once in a year per square meter. CRs with even higher energies occur once per year per square kilometer.

There are two breaks in the CR energy spectrum, one around 10^{15} eV called the 'knee' and the other at around 10^{19} eV called the 'ankle'. CRs with energies below 10^{18} eV are believed to originate in the Galaxy, while the gyroradius of the CRs with the energies above is larger than the thickness of the Galactic disk and, thus, they are believed to come from outside of the Galaxy. The energy spectrum below the 'knee' follows the power-law shape with the slope index of -2.7, while the slope index for the CR energy range between the 'knee' and the 'ankle' has a value of -3. Over decades, these observed indices have not changed. The CR energy spectrum is significantly modulated by the Sun. When CRs encounter a turbulent solar wind with an embedded heliospheric magnetic field, they can significantly change their energy. As a result, the spectral shape bends downward for energies lower than 30 GeV. The Sun itself is also a source of energetic charged particles with typical energies of 10–10 MeV which can also sporadically (about once per year) reach 1 GeV energies and rarely (once in ten years) even 10 GeV. The solar nuclei and electrons are accelerated by shock waves in the corona and by magnetic energy released in solar flares, most prominent during the active phase of the solar cycle.

There are some indications that the chemical composition of CRs becomes dominated by heavier elements as we go toward higher energies (Hörandel 2006). Apel et al. (2013) managed to separate light from heavy elements' spectral contribution in the energy range 10^{16} – 10^{18} eV analyzing the air shower. They found that up to 10^{17} eV light elements dominate the spectrum, while iron-like CRs become prominent at around 10^{18} eV and comparable to the contribution of light elements. They interpreted this feature as a transition from Galactic to extragalactic CRs. However, this result is not in agreement with earlier findings by Sokolsky & Thomson (2007) and Abraham et al. (2010) of the light elements dominant role at energies of 10^{18} eV. This inconsistency is not surprising since the interpretation of the spectrum for the energies above the 'knee' is quite complex, because the number of particles detected above this threshold is low.

The cores of Active Galactic Nuclei (AGN), Gamma Ray Bursts (GRBs) or powerful radio galaxies are good candidates for producing ultrahigh energy CRs, i.e., CRs with the energies above the 'ankle' (Miralda-Escudé & Waxman 1996; Berezhko 2008; Kohta et al. 2012). SNRs are thought to be the main contributors to the Galactic CR flux densities measured on the Earth (Baade & Zwicky 1934). As potential sources, they are expected to be able to convert 10–20% of their kinetic energy to CRs, match the CR energy spectrum described above, account for the observed chemical abundances in the Galaxy and explain multiwavelength observations of SNRs.

1.5.1 CR ACCELERATION IN SNRS

Enrico Fermi was the first to propose that a charged particle can gain or lose its energy in collision with a magnetic mirror, i.e., a magnetized cloud (Fermi 1949). The particle gains energy in the head-on collision with the cloud. In the tail-on collision it loses the energy. The relative energy gain in this process is proportional to the quadratic cloud-to-particle velocity ratio, i.e., $\varepsilon = \Delta E/E = (4/3)(V/c)^2$, where V is the cloud bulk velocity and we assume that the particle velocity is close to the light speed c . Due to this quadratic dependence, this process is best known as the **second-order Fermi** acceleration mechanism. In the ISM plasma, (Alfvén) waves play the role of magnetized clouds in the mentioned process. The Alfvén speed is given by

$$V_a^i = \sqrt{\frac{B_0}{4\pi\rho_0^i}},$$

where B_0 is the magnetic field strength which is about $\approx 3 \mu\text{G}$ in the interstellar gas, and ρ_0^i is the ion mass density where if we consider only protons and its number density of $\approx 10^5 \text{ m}^{-3}$, we get $V_a^i \approx 20 \text{ km s}^{-1}$. This velocity will introduce a small energy gain of the charged particle yielding an inefficient acceleration process, applicable to the Galactic disk for example.

Unlike these low cloud velocities, shock waves around SNRs have three order of magnitude higher velocities of $\sim 1000 \text{ km s}^{-1}$. Due to magnetic field presence, more precisely its fluctuations, a CR particle goes collisionlessly back and forth across the shock front and gains energy. This process is called **diffuse shock acceleration** (DSA) and is based on the **first-order Fermi** acceleration mechanism where the relative energy gain of the particle is linear function of the velocity ratio of the gas behind the shock front and the CR particle (Bell 1978). In the first-order Fermi mechanism, the collisions are always head-on and the particle always gains the energy. This is due to the fact that a particle going from upstream to downstream encounters the shocked gas moving at $V \approx 3/4V_s$ in the upstream rest frame. When the particle passes from downstream to upstream, it sees the upstream gas moving with $V \approx 3/4V_s$ in the downstream rest frame. The energy transferred to the particle is the same in each crossing, and the relative energy gain after averaging over scattering angles is $\varepsilon = \Delta E/E = (4/3)V/c$ in one completed cycle (upstream-downstream-upstream). DSA was discovered independently by Axford et al. (1977), Krymskii (1977), Bell (1978) and Blandford & Ostriker (1978). Most of those authors used the Fokker-Planck equation to describe the momentum distribution of high energy particles in strong shocks, while Bell (1978) followed the behaviour of individual particles.

The shock front thickness is generally much smaller than the gyroradius of high energy particles. For a particle energy of 10^{14} eV and a typical ISM magnetic flux density of $\sim 1 \mu\text{G}$, the proton gyroradius is about 1 pc. The shock thickness is determined by the scale of instabilities that dis-

sipate the shock energy, and it is usually several gyroradii ($\sim 10^8$ cm) of the downstream thermal particles (mostly protons). In order that downstream charged particles recross the shock front and end up upstream participating in the DSA process, they need momentum of $p \gtrsim p_{\text{inj}} \approx (3-4)p_{\text{th},p}$, where $p_{\text{th},p} = \sqrt{2m_p k T_2}$ is the momentum of thermal protons with the downstream temperature T_2 and k the Boltzmann constant (Kang et al. 2002). Assuming full thermal equilibration of electrons and protons downstream ($T_e \approx T_p$) and a Maxwellian particle distribution, the number of protons having the momenta above the injection momentum (i.e. the so-called suprathermal particles) is much greater than the number of electrons. This implies that electrons have to be pre-accelerated before being able to take part in the DSA process. It is important to mention that the injection of the suprathermal particles into the process of acceleration at astrophysical shocks is poorly known. Once injected into the DSA process, particles are scattered by streaming instabilities or turbulent motions on both sides of the shock front.

To infer the energy spectrum of high energy particles produced in DSA, we assume that the initial particle energy is E_0 and N_0 their number, that the average particle energy after one collision is $E = (1 + \varepsilon)E_0$, and the probability for a particle to remain in the region of acceleration after one collision is P . After b collisions we then have $N = N_0 P^b$ and $E = E_0(1 + \varepsilon)^b$. Solving these two equations for b and taking derivation per energy E , we get the power-law spectrum:

$$N(E)dE \propto E^x dE,$$

where $x = -1 + \ln P / \ln(1 + \varepsilon)$. We know that $\varepsilon = (4/3)(V/c)$ for first-order Fermi acceleration mechanism. The rate at which particles cross the shock front in either direction is given by the projection of an isotropic flux onto the plane shock front and is equal to $\rho_{\text{cr}}c/4$, where we assume particles are relativistic and their number density is given with ρ_{cr} . We assume that particles are rapidly isotropized on both sides of the shock front. The rate at which downstream particles are advected from the shock is $\rho_{\text{cr}}V_s/4$. The probability that a particle stays inside the region of acceleration is:

$$P = 1 - \frac{\rho_{\text{cr}}V_s/4}{\rho_{\text{cr}}c/4} = 1 - \frac{V_s}{c}.$$

This will give the power-law spectral index:

$$x = -1 + \frac{\ln P}{\ln(1 + \varepsilon)} = -1 + \frac{\ln(1 - V_s/c)}{\ln(1 + \frac{4}{3} \frac{3/4 V_s}{c})} = -2,$$

where we used $\lim_{x \rightarrow 0} \ln(1 \pm x) = \pm x$ approximation. Therefore, the differential energy spectrum of high energy particles in the presence of strong shocks and under the assumption of the particles isotropization on both sides of the shock is:

$$N(E)dE \propto E^{-2}dE.$$

Following the same approach, one will get for the energy spectrum of high energy particles in the weak shocks (compression factor $r < 4$):

$$N(E)dE \propto E^{-q+2}dE,$$

where $q = 3r/(r - 1)$.

DSA does not take into account back-reactions of accelerated particles on the shock structure, but rather treats them as test particles. Irregularities in the magnetic field might be either pre-existing fluctuations in the ISM or generated by Alfvén and hydromagnetic waves, which are excited by the streaming motions of suprathermal particles (Wentzel 1974; Cesarsky 1980). The momentum of the particles' beam is transferred to the waves which is further related to the growth rate of the instability given by the formula (Cesarsky 1980):

$$\Gamma = \omega_g \frac{N(\geq E)}{N_p} \left(-1 + \frac{|V|}{V_a}\right),$$

where ω_g is non-relativistic angular gyrofrequency of a proton, $N(\geq E)$ is the number density of the particles with the energy E that resonate with the Alfvén waves, N_p is the proton number density, V is the particle velocity and V_a is the Alfvén speed. As long as the streaming velocity of the high energy particles is higher than the Alfvén speed, we can expect the instability to grow. However, the calculation was done assuming a fully ionized plasma. If the ISM is partially ionized, the neutral particles remove the energy from the waves in ion-neutral collisions in a time short compared to the growth time of instabilities, leading to ion-neutral wave damping (see O'C Drury et al. (1996) for a review). Therefore, in partially ionized plasma, the instability is effective only when the waves are not damped before they grow to large amplitudes. Moreover, particles are effectively scattered only if the scale of the magnetic field fluctuations are comparable to the particles' gyroradii. In the case when the magnetic field fluctuation scale is much larger than the particle gyroradius, the particle's trajectory remains unaffected as well as in the case when the fluctuation scale is much smaller than the particle gyroradius, because its trajectory is determined by the mean magnetic field much larger than its fluctuating component. Finally, the shock obliquity defined by the angle between the shock normal and the ambient magnetic field is also important for the process of injection and acceleration. At quasi-perpendicular shocks, where the mentioned angle is larger than 45° , the self-excitation of waves is ineffective and the injection of suprathermal protons is significantly suppressed (Caprioli & Spitkovsky 2013).

As noted above, the streaming of the particles excites resonant Alfvén waves, non-resonant waves and turbulence, and reduces the acceleration time, but should also provide the way to accelerate particles up to the 'knee'. Particles are most efficiently accelerated in the free-expansion phase of a SNR evolution, so if we assume $B = 1\mu\text{G}$ in the ISM, $V_s = 10^4 \text{ km s}^{-1}$ and acceleration time of $t \approx 10^3 \text{ yr}$, the particles are accelerated up to 10^{14} eV in the DSA theory which is well below

the 'knee' energy limit. Moreover, we see that DSA gives the spectral index of -2 for strong shocks while the observations give steeper energy spectrum (Figure 1.3). The pressure which accelerated particles induce on the plasma is not negligible and has to be taken into account when studying shock dynamics and the acceleration process itself. It will decrease the compression ratio ($r < 4$), increase index q , and, thus, decrease the energy spectral index ($x < -2$). If the magnetic flux is frozen in the plasma on both sides of the shock front, one would expect an increase of the magnetic field strength of a factor 4 in the downstream region. The observations of narrow non-thermal X-ray filaments around young SNRs indicate the presence of magnetic fields two order of magnitude higher than predicted by DSA in strong shocks (Vink 2012). Moreover, numerical calculations of Lucek & Bell (2000), Bell & Lucek (2001) showed that instabilities lead to magnetic field amplification. The acceleration process is strongly nonlinear and requires numerical methods to be studied in detail. The review of the **non-linear theory of DSA (NLDSA)** is given by Malkov & Drury (2001) and its physical aspects on the CR energy spectrum has been discussed by Blasi (2013).

1.5.2 OBSERVATIONAL SIGNATURES OF CR ACCELERATION IN SNRS

Radio, X-ray and γ -ray observations provide evidence for CR acceleration in SNRs. Acceleration of CR *electrons*⁷ in SNR shocks is best probed via synchrotron radio (electron energy of order 1 GeV) and non-thermal (mostly synchrotron) X-ray emission (electron energy in the range 10–100 TeV). While radio synchrotron emission might originate from electrons accelerated at much earlier times, for X-ray synchrotron emission, which probes the highest energy electrons accelerated, the acceleration happened recently and is still on-going. Non-thermal emission provides an estimation of CR acceleration efficiency in SNRs, the maximum energy to which the particles are accelerated, the magnetic field strength and its amplification. However, although some of the shell-like SNRs show prominent non-thermal (synchrotron) X-ray filaments (Koyama et al. 1995, 1997), shell-like SNRs are mostly dominated by X-ray thermal emission with strong lines of heavy elements from the shock-heated gas (both ISM and ejecta).

To accelerate a particle to an energy E , one has to take into account two limitations: the remnant's age and the particle's loss (cooling) time. Unlike protons, electrons lose their energy fast in the process of synchrotron radiation and inverse Compton (IC) scattering. The process of acceleration stops once the acceleration and loss time scales become equal. Therefore, protons/ions can obtain higher energies than electrons. The electrons are accelerated to the maximum energy

⁷Due to their ≈ 2000 times lower masses, CR *electrons* lose their energies much faster than CR *protons*, making the contribution of the latter to the synchrotron radio and X-ray emission negligible.

given by Reynolds & Keohane (1999):

$$E_{\max}[\text{TeV}] \approx 10 \left(\frac{B}{100\mu\text{G}} \right)^{-1/2} \frac{V_s}{1000\text{kms}^{-1}}.$$

In the loss-limited regime, advection and diffusion are of the same order at the maximum energy of electrons. The combination of two sets the emission scale of the synchrotron filaments behind the shock front. The X-ray filament thickness can be inferred from the advection length scale for the electrons that are moving away from the shock front and do not gain the energy, but rather lose it in radiation: $L_{\text{adv}} = V_s \tau_{\text{loss}}/r$. On the other hand, the particles diffuse around the shock and the thickness can be defined as the diffusion length scale: $L_{\text{diff}} \approx 2Dr/V_s$, where D is diffusion coefficient behind the shock front. The diffusion coefficient can be written as $D = \lambda_{\text{mfp}}c/3$ (Drury 1983), where λ_{mfp} is the mean free path of a particle interaction given in terms of gyroradius. The relationship between L_{adv} and L_{diff} is then (Vink & Laming 2003; Berezhko et al. 2003):

$$L_{\text{diff}} \approx \frac{3}{2} \left(\frac{r-1}{4} \right) L_{\text{adv}}.$$

The loss-limited case for $r = 4$ gives $L_{\text{adv}} \approx L_{\text{diff}}$ (Helder et al. 2012). The thickness of the synchrotron X-ray filament is the convolution of the advection and diffusion length scales, and for $L_{\text{adv}} \approx L_{\text{diff}}$ we have:

$$\Delta L[\text{pc}] \approx \sqrt{2}L_{\text{adv}} = \sqrt{D(E_{\max})\tau_{\text{loss}}(E_{\max})} \approx 0.04 \left(\frac{B}{100\mu\text{G}} \right)^{-3/2},$$

where $D(E_{\max})$ is the CR diffusion coefficient and τ_{loss} is the time for which CRs lose their energy. The magnetic field downstream is much higher than the upstream field and it is, thus, expected that the non-thermal emission comes predominantly from the downstream region. Moreover, the detection of synchrotron X-ray emission suggests highly turbulent magnetic fields in order to achieve electron energies of $\gtrsim 10$ TeV. The typical measured width of those filaments is $\sim 5 \times 10^{16}$ cm and predicts the value of 100–300 μG for the post-shock magnetic field strength (Hwang et al. 2002; Vink & Laming 2003). This result provides observational evidence for the DSA theory and generation of the turbulent magnetic field larger than the ordered ISM field.

Radio and X-ray emission give the information on CR *electrons*, but 99% of CRs observed on the Earth are atomic nuclei (mostly protons). Accelerated CR *protons* and *nuclei* are potential sources of GeV and TeV γ -ray emission through pion π^0 -decay (hadronic model). CR *protons* collide with the background plasma and create π^0, π^+, π^- , where only π^0 creates γ -rays: $p + p \rightarrow \pi^0 \rightarrow 2\gamma$. The other two pions produce a positron and an electron which further create low level IC and synchrotron radiation. Each produced photon in π^0 -decay has an energy of 135 MeV which is the half rest energy of the π^0 in the collision rest frame. The source's CR

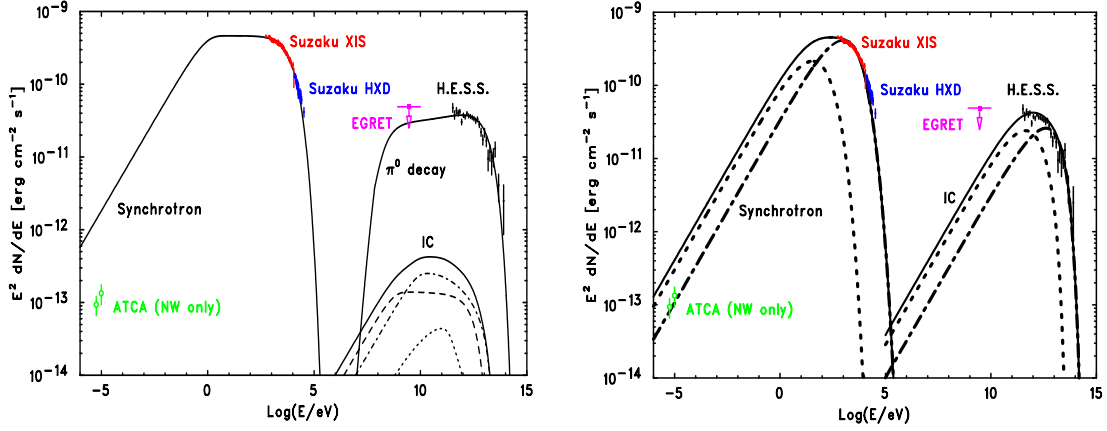


Figure 1.4: Multi-wavelength spectral energy distribution of the remnant RX J1713.7-3946: ATCA (radio data), Suzaku (X-ray data), EGRET source 3EG 1714-3857 (GeV γ -ray data) and H.E.S.S. (TeV γ -ray data). Left: Hadronic model fit with the parameters: $E_e = 3.1 \times 10^{46}$ erg - the total energy of electrons; $E_p = 2.7 \times 10^{50}(n/1\text{cm}^3)^{-1}$ erg - the total proton energy and n is the ambient matter density; $B = 200 \mu\text{G}$; power-law injection spectrum with an index of 2 is assumed for both electrons and protons. The dashed line, the dash-dotted line, and the dotted line are IC flux of CMB, infrared, and optical photons, respectively. Right: Leptonic model fit with the parameters: two electron populations with energies $E_e = 1.4 \times 10^{47}$ erg (dotted-dashed line) and $E_e = 3.4 \times 10^{47}$ erg (dotted line) for the magnetic field of $B = 14 \mu\text{G}$. As it is shown, both models hadronic and leptonic can nicely fit the same data. Credit: Tanaka et al. (2008).

spectrum and the ISM density define the number of π^0 , where higher CR *proton* energy yields more pions per p-p collision, and, therefore, γ -ray spectrum and emissivity.

Many young (Aharonian et al. 2001; Enomoto et al. 2002; Aharonian et al. 2005, 2009; Acciari et al. 2011) and middle-age SNRs (Albert et al. 2007; Aharonian et al. 2008; Abdo et al. 2010) are bright in γ -rays. However, the γ -ray detection does not have a unique interpretation regarding the nature of its potential particle sources. This is because the CR *electrons* can also produce γ -rays through IC and bremsstrahlung. Relativistic electrons scatter of cosmic microwave background (CMB) photons which usually dominate the photon field in the Galaxy, and, thus, contribute to γ -ray emission through IC (leptonic model) which is very efficient at TeV energies. The emissivity of IC scattering depends on the background photon field, the relativistic electron's and the ISM density. The same electrons that produce γ -ray emission, produce also radio synchrotron radiation. Non-thermal bremsstrahlung emission, formed in a relativistic electron deceleration in the charged particle field, also contributes to the γ -ray spectrum. This emission is highly sensitive to the background density.

Gamma ray production ratio in the case of IC and π^0 -decay is about $10^3(E_e/E_p)(n/1\text{cm}^{-3})^{-1}$, where E_e and E_p are total energies of 20 TeV electrons and protons, respectively (Aharonian et al. 2013). For a typical SNR shell gas densities ($n \leq 1\text{cm}^{-3}$) and magnetic fields of order of $1\mu\text{G}$, IC dominates over π^0 -decay even if the number of electrons is much smaller than the number of protons. In case of magnetic fields of order of $10\mu\text{G}$ or higher, electrons would lose their energy in synchrotron radiation rather than contribute to IC γ -ray component. SN explosion initial parameters and the ISM properties give the preconditions to the particle acceleration and radiation processes. It is then not surprising that the interpretation of the detected radiation requires the knowledge of magnetic field, photon field and densities.

Explaining γ -ray spectrum is, thus, quite complicated in practice, because the data can be fitted with any of these models by just tuning the parameters (see Figure 1.4). It is often the case that the spectrum can be either explained with IC for smaller magnetic fields ($\approx 6\mu\text{G}$) where π^0 -decay brings negligible contribution at this low magnetic fields, or with π^0 -decay for $B \geq 100\mu\text{G}$ and high density. On the other hand, the Klein-Nishina effect suppresses the contribution of the IC component for energies higher than 10 TeV (Aharonian et al. 2013). Also, the presence of the γ -rays and X-ray synchrotron emission at the same time and position in the remnant refers to CR *electron* presence. If the same region show no signs of thermal X-rays, this would yield low density medium in SNR and would further support the previous statement. As pointed out by Drury et al. (2009), thermal emission might be suppressed by very low plasma temperature as a result of efficient non-linear CR acceleration.

Old SNRs have stopped producing high-energy particles, but since they are usually (in the case of core-collapse SNe) in the vicinity of molecular clouds (Hewitt et al. 2009), they are suitable for studying CR propagation and the escape from their sources in two different events: when the shock propagates inside the cloud, and when escaped CRs interact with the cloud. Gamma ray emission in high densities in and around these SNRs is easier linked to pion-decay or non-thermal bremsstrahlung, because both scale with the density. Using the Fermi Large Area Telescope (Fermi LAT), Ackermann et al. (2013) have recently detected the characteristic pion-decay feature in the two old SNRs (IC443 and W44) interacting with the molecular clouds. The pion-decay and non-thermal bremsstrahlung processes were analyzed, where the latter failed to fit the data (see Figure 1.5). This is the first direct evidence for the CR *protons* being accelerated in SNRs.

So far, we have discussed radio, X-ray and γ -ray observations that can reveal the presence of CRs in SNRs with the particular emphasize on pion-decay that can indicate CR *proton* existence. In the next Chapter we will review how the optical observations, namely Balmer $H\alpha$ lines, can also trace CR *protons* in young SNRs. We will present the theoretical foundation of the optical shocks and will describe the observational techniques suitable for studying these shocks around SNRs and novae.

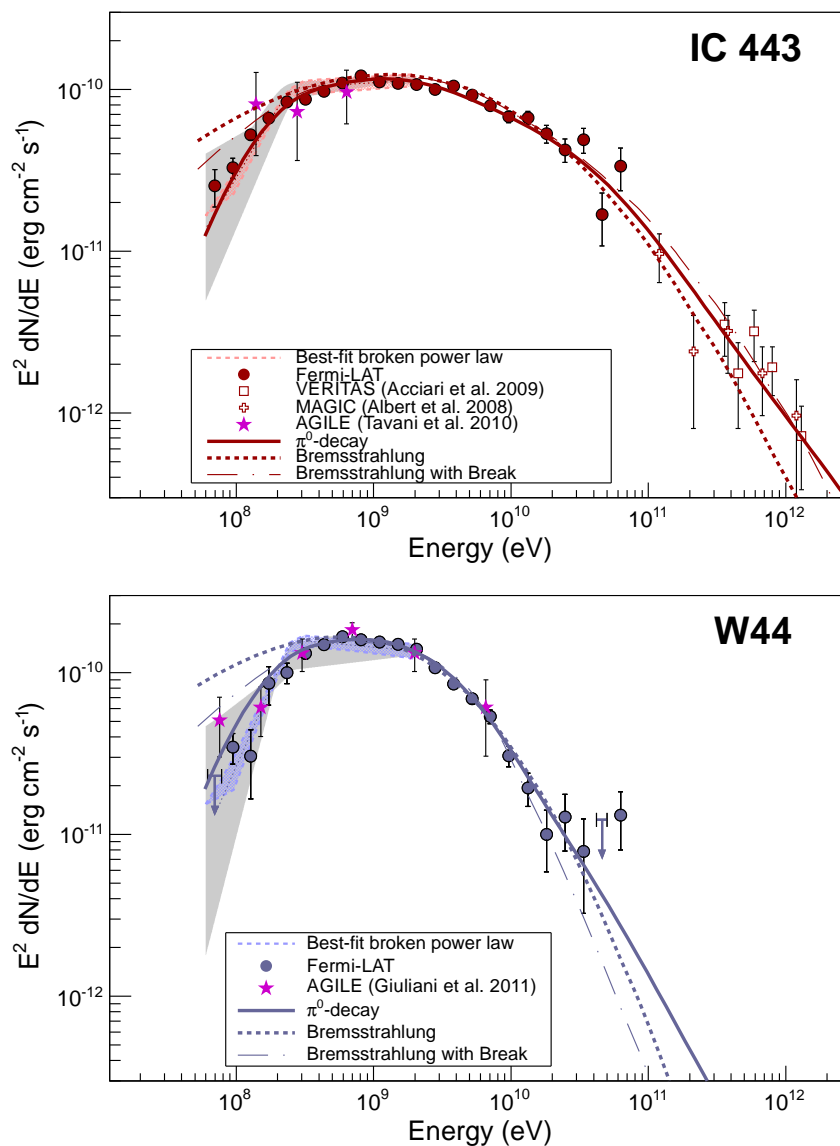


Figure 1.5: Gamma ray spectra of the remnants IC443 and W44. Solid and dashed lines show the best-fit (fitting only Fermi LAT data) pion-decay and bremsstrahlung spectra, respectively. The dash-dotted lines denote the best-fit bremsstrahlung spectra which include a low-energy break at $300 \text{ MeV} c^{-1}$ in the electron spectrum. The gray-shaded bands show systematic errors below 2 GeV caused by galactic diffuse emission modeling. The dashed orange and violet-shaded box is the best fit broadband smooth broken power law (60 MeV to 2 GeV). Credit: [Ackermann et al. \(2013\)](#).

OUTLINE OF THE THESIS

The main part of the thesis focuses on studying Balmer $H\alpha$ lines around SNRs and novae. Chapter 2 presents the theory behind Balmer-dominated shocks and introduces different observational techniques for studying optical shocks. Chapter 3 shows the use of integral-field spectroscopy for tracing the shocks in a small region at the northwestern rim of the SNR SN 1006, deducing the shock parameters (shock velocity and electron-to-proton equilibration level) and revealing the presence of suprathermal protons in the remnant. Chapter 4 contains the Fabry P erot data of Tycho's SNR, where we again deduce shock parameters, but now for a region that contains one-fourth of the remnant's shell. The use of integral-field spectroscopy in the case of the classical nova FH Ser is shown in Chapter 5, where we analyze the object structure and explosion mechanism through the $H\alpha$ -line profiles. Chapter 6 summarizes this thesis and discusses prospects for related future work.

ABSTRACT

Our research is focused on studying optical shocks, i.e., Balmer-dominated shocks (BDSs), around novae and supernovae. These optical shocks are characterized by strong hydrogen emission lines with a narrow ($\sim 10 \text{ km s}^{-1}$) and a broad ($\sim 1000 \text{ km s}^{-1}$) component. In this chapter we will review the physics behind BDSs, summarizing theory and observations, including models with and without shock precursors – regions ahead of the shock where the heating occurs as a result of particles or waves streaming from the post-shock region. We will then introduce some of the spectro-photometric techniques convenient for observing optical shocks around (super)novae. We will mainly focus on three observational techniques: long-slit spectroscopy, Fabry-Pérot interferometry, and integral-field spectroscopy. The first two are commonly used when studying shocks around the remnants of supernovae and novae (Smith et al. 1994; Gill & O’Brien 2000; Rakowski et al. 2003) while the latter is mainly used in studying galaxies (Heald et al. 2007). In this work, we use Fabry-Pérot interferometry and narrow-band tunable filter imagery to study BDSs around Tycho’s supernova remnant (SNR) (see Chapter 4), and integral-field spectroscopy to study shocks in the remnant of supernova SN 1006 and in the classical nova FH Ser (see Chapters 3 and 5). Detailed descriptions of our observations, data reduction and results will be provided in the respective chapters.

2.1 BALMER-DOMINATED SHOCKS

Balmer-dominated shocks (BDSs) are dominated by the Balmer lines of hydrogen atoms with absent or very weak forbidden lines. These shocks have relatively high velocities ($\gtrsim 200 \text{ km s}^{-1}$)

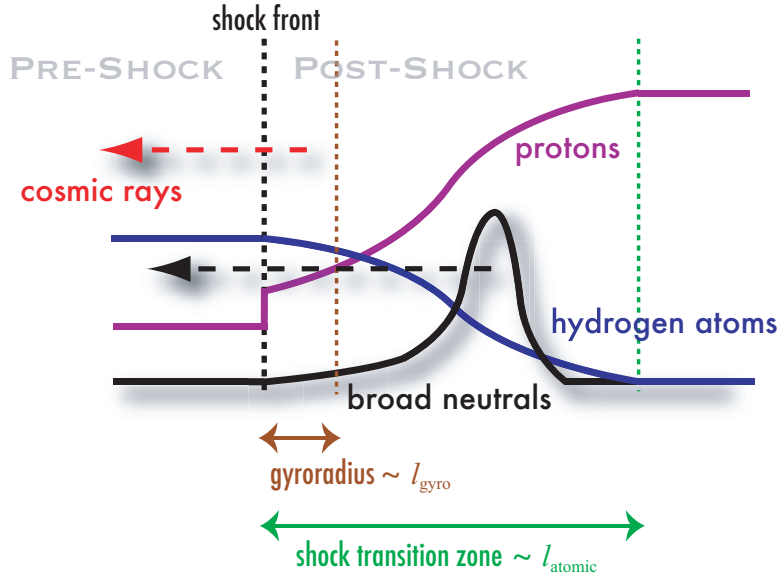


Figure 2.1: Transition zone in Balmer-dominated shock where excitation, charge exchange and ionization take place. The width of the shock transition zone is set by the total upstream density and mean free paths for atomic interactions (excitation, charge exchange and ionization). Also shown are pre-shock hydrogen atom, proton and broad neutral density distributions across the transition zone. While neutrals can cross the shock front unaffected by EM fields and plasma turbulence, charged particles follow Rankine-Hugoniot jump conditions (see proton density distribution at the shock front). Credit: Heng (2010).

and are thus **non-radiative** (see Section 1.4). The ambient medium surrounding BDSs must be partially neutral for these lines to be produced. This is the reason why they are traditionally observed around SNe Ia. By contrast, core-collapse SNe are sources of strong UV radiation which pre-ionizes the surrounding medium leaving almost no neutrals. A non-radiative shock propagating into a fully ionized medium would be invisible at optical wavelengths; radiation from the shock itself can pre-ionize the gas, but this does not apply to non-radiative shocks, where cooling and recombination times are larger than the age of the remnant.

Another characteristic of BDSs is that they are **collisionless**. Interstellar shocks around (super)novae propagate through low density media ($\sim 1 \text{ cm}^{-3}$). The mean free path (l_{mfp}) for particle interactions is given by

$$l_{\text{mfp}} \approx 2.27 \times 10^{-12} V_p^4 / n_p,$$

where V_p is the proton velocity and n_p the proton density (Drain & McKee 1993). Shocks around young SNRs have velocities of $\sim 1000 \text{ km s}^{-1}$ and $n_p \sim 1 \text{ cm}^{-3}$ implying $l_{\text{mfp}} \gtrsim 50 \text{ pc}$ which is much greater than typical SNR's radius ($\sim 1 \text{ pc}$), and, thus, also greater than the width of the shock front. Collisions are thus ineffective and cannot form the shock. Instead, the shock is created by the electromagnetic (EM) fields and plasma turbulence which scatter incoming charged particles over the width of an order of proton gyroradius $\sim 10^8 \text{ cm}$ (Friedman et al. 1971). This implies that the shock thickness is measured in ion gyroradii rather than collision mean free paths.

The important difference between collisional and collisionless shocks is that electrons and protons equilibrate almost instantaneously through collisions in the collisional case ($T_e \approx T_p$). In collisionless shocks, electrons and protons can be far from equilibrium ($T_e \ll T_p$) as the Coulomb equilibration rate is low (Ellison et al. 2010). However, EM coupling between electrons and protons can bring T_e closer to T_p (Cargill & Papadopoulos 1988). Unlike charged particles, neutrals entering the shock are unaffected by the EM fields and plasma turbulence. Due to low interstellar medium (ISM) density in collisionless shocks, they can travel $\sim 10^{14}$ – 10^{15} cm (the width of the transition zone, see Figure 2.1) downstream before being ionized.

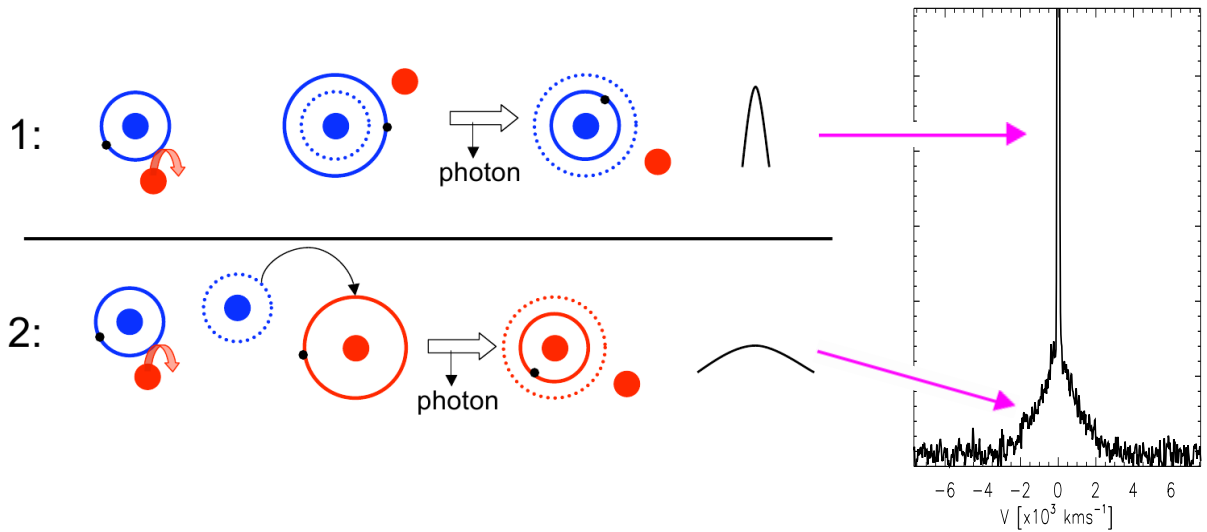


Figure 2.2: The mechanisms that produce the two-component $H\alpha$ line. The narrow component is a product of a radiative decay of a slow neutral excited in collisions with hot electrons or protons (process 1). The broad component is the result of a radiative decay of an excited, fast neutral formed in a charge exchange (process 2) between a slow neutral and a hot proton. Blue/red circles indicate cold/hot protons and small, black circles electrons. Credit: E.A. Helder, PhD thesis.

BDSs are mainly seen as very faint edge-on optical filaments around young SNRs. Among all hydrogen Balmer lines, $H\alpha$ line is the brightest. It is a **two component line** with a narrow ($\sim 10 \text{ km s}^{-1}$) and a broad ($\sim 1000 \text{ km s}^{-1}$) component¹. BDSs were first observed in the eastern limb of the historical galactic remnant Tycho (Minkowski 1958). It took nearly 20 years to explain the observed two-component lines. Chevalier & Raymond (1978) defined the mechanisms that form the two components (see Figure 2.2). When cold and slow hydrogen atoms in the pre-shock region are overrun by the shock, they can be either excited or ionized by electrons or protons downstream, or they can undergo charge exchange (CE) with hot and fast protons in the post-shock region². A narrow component is produced in a radiative decay of an excited slow neutral (hereafter narrow neutral). The width of the narrow component is set by the pre-shock temperature. A broad component is produced in a radiative decay of an excited fast neutral (here-

¹Some SNRs in the radiative phase also show Balmer lines, but not as two-component lines.

²Traveling further downstream all the atoms eventually become ionized.

after broad neutral) created in a CE process between a slow neutral and a hot proton. The width of the broad line is related to the temperature of the hot protons, which in turn depends on the shock velocity (Chevalier & Raymond 1978; Chevalier et al. 1980).

Broad component widths are used to estimate shock velocities. The combination of measured proper motions of Balmer filaments with the shock velocity provide distance estimates (Helder et al. 2013). Moreover, the width of the broad component and the intensity ratio between the two components depend on the electron-proton³ equilibration (Chevalier & Raymond 1978; Chevalier et al. 1980; van Adelsberg et al. 2008; Heng 2010). Further, when we combine optical observations (inferred T_p) with X-ray and radio observations (inferred T_e), we can estimate the electron-proton equilibration independently of the former method. BDSs are, thus, a powerful tool for studying physical conditions in the shocks.

In an idealized scenario, the pre-shock gas is not affected (e.g. temperature, ionization state) by the oncoming shock until the latter arrives. However, the post-shock gas can influence the physical conditions in the pre-shock region. This phenomenon is termed a precursor. The shocked gas can be a source of photons, particles and waves that can overtake the shock and heat the pre-shock gas. Mach number, ambient density and orientation of the magnetic field define the precursor type. Its existence can affect the lines' widths, intensities and even their shapes.

2.2 NARROW H α -LINE PROFILES AND PRECURSORS

Observations revealed narrow H α -line widths beyond the expected 10–20 km s⁻¹ gas dispersion (Smith et al. 1991; Sollerman et al. 2003). If the measured full widths at half maximum (FWHM) of 30–50 km s⁻¹ would be purely thermally broadened, a kinetic temperature of 20 000–50 000 K would be needed to explain the results. This temperature is higher than 10 000 K, the temperature expected for the undisturbed ISM where neutral hydrogen atoms exist. Higher temperatures will leave no neutral hydrogen in the pre-shock region, and no Balmer emission would be produced. In the following subsections, we will review different effects (post-shock and pre-shock) that might be responsible for the broadening of the narrow H α line (Smith et al. 1994; Heng 2010). However, we will see that the post-shock effects are not efficient in broadening the narrow H α line, which is why pre-shock effects with a precursor have to be invoked.

³It would be more precise to say electron-ion equilibration, but we refer to electron-proton rather because of very low abundances of heavier ions in the ISM.

2.2.1 POST-SHOCK EFFECTS

- **Lyman line trapping:** Balmer H α line is produced in hydrogen deexcitation from level 3s/3d to 2p and 3p to 2s. The latter can produce Lyman β (Ly β) line instead, in the transition from 3p to 1s. The narrow H α line can in principle be broadened if its wings are optically thick for (broad) Ly β photons. The shock speed, the electron-proton temperature ratio and the pre-shock ionization fraction define the conversion efficiency of Ly β to H α photons. Monte Carlo simulations of the Ly β radiative transfer (Smith et al. 1994) showed that absorption of (narrow) Ly β is more efficient in the centre of the narrow H α line, effectively narrowing the line further instead of broadening it.
- **Elastic collisional heating of slow neutrals by hot electrons/protons in the post-shock:** The lifetime of a neutral hydrogen before CE or ionization is given as

$$1/\tau = n_i V \sigma_{\text{CE}} + n_e q_i,$$

where $V \sim 3V_s/4$ is the particle velocity, σ_{CE} the CE cross section, q_i the ionization rate coefficient and n_i (n_e) are ion (electron) densities. No ionization by ions is included because they might produce broad neutrals. In elastic scattering, a neutral can change its velocity by $\Delta V = V\tau/(2t_s)$, where $t_s = 1/(n_i\sigma_{\text{EL}}V)$ and σ_{EL} is elastic scattering cross section (Spitzer 1968). As calculated by Smith et al. (1994), the shock speed of 300 (1000) km s $^{-1}$ implies neutral's velocity change of 9 (13) km s $^{-1}$. To summarize, the most efficient heating would be for either high shock velocities $\gtrsim 3000$ km s $^{-1}$ or complete electron-proton equilibration. The first implies that this broadening mechanism is limited to high shock speeds which stands in contradiction to broadened narrow lines observed in older SNRs (Tuohy et al. 1982). The second is not favored by present non-radiative shock models (Raymond et al. 1983; Cargill & Papadopoulos 1988; Laming et al. 1996).

- **Molecular dissociation:** Dissociation of pre-shock molecular hydrogen would produce hydrogen atoms heated to ≈ 30 km s $^{-1}$. This requires almost all pre-shock hydrogen to be molecular. However, for typical non-radiative shock velocities $V_s \gtrsim 1000$ km s $^{-1}$ CE ($\text{p}+\text{H}_2 \rightarrow \text{H}+\text{H}_2^+$) destroys molecular hydrogen and creates fast neutrals instead. Also, for those velocities electrons are heated enough to trigger another reaction $\text{e}^-+\text{H}_2 \rightarrow 2\text{e}^-+\text{H}_2^+$, likewise depleting H $_2$.

2.2.2 PRE-SHOCK EFFECTS

- **Electron thermal conduction precursor:** In case of a complete equilibration in the post-shock gas, electrons are heated to velocities greater than the shock velocity and can over-

take the shock in the form of a precursor⁴ (Zel'dovich & Raizer 1966). In a pure hydrogen gas, using $\beta = T_e/T_p$ as a measure of electron-proton equilibration and m_p (m_e) as proton (electron) mass, electron/proton temperatures and thermal velocities are given as follows:

$$T_e \approx \frac{3m_p V_s^2}{16k} \frac{\beta}{1+\beta},$$

$$T_p \approx \frac{3m_p V_s^2}{16k} \frac{1}{1+\beta},$$

$$V_{\text{th},e} \approx \frac{3V_s}{4} \sqrt{\frac{m_p}{m_e} \left(\frac{\beta}{1+\beta} \right)},$$

$$V_{\text{th},p} \approx \frac{3V_s}{4} \frac{1}{\sqrt{1+\beta}}.$$

When the pre-shock region is taken as the rest frame, the post-shock fluid bulk velocity is $\sim 3V_s/4$. For $\beta=1$, $V_{\text{th},e}$ is much higher than the post-shock bulk velocity, and electrons can escape upstream. The electron temperature in a thermal conduction precursor would be higher than the temperature of pre-shock ions. However, even for high Coulomb collision rates, the length scale for electron-proton interactions is an order of magnitude larger than the electron ionization scale. Thus, electrons will predominantly ionize pre-shock neutrals and are unlikely to be the explanation for the narrow H α line broadening.

- **Magnetohydrodynamic (MHD) precursor:** If the Alfvén velocity in the ionized component of the plasma is greater than the shock velocity, a MHD precursor can form. The Alfvén velocity is given (in CGS units) as

$$V_a^i = \sqrt{\frac{B_0}{4\pi\rho_0^i}},$$

where B_0 and ρ_0^i are the magnetic field strength and the total mass density of charged particles in the pre-shock, respectively. This precursor requires a low pre-shock ionization fraction ($f_{\text{ion}} \lesssim 0.2$), and high magnetic fields of $B \sim 100 \mu\text{G}$ (two orders of magnitude higher than expected in the ISM) for typical $V_s \approx 2000 \text{ km s}^{-1}$ and $n_0 \approx 1 \text{ cm}^{-3}$. This pre-shock magnetic field strength is unrealistic, and rules out this scenario.

- **Photoionization precursor (PIP):** In strong radiative shocks ($V_s \geq 110 \text{ km s}^{-1}$, $n \geq 10 \text{ cm}^{-3}$), substantial Lyman flux is produced when gas starts to cool and recombine downstream. The produced photons escape to the pre-shock region and form a PIP (Cox 1972; Ray-

⁴This might not be possible for collisionless shocks, because the EM field and plasma turbulence may confine electrons to the post-shock region (Borkowski et al. 1989).

mond 1979). A PIP in a strong radiative shock can fully ionize the pre-shock gas (Vancura et al. 1992; Morse et al. 1996). Non-radiative shocks lack recombination zones, but that does not prevent them from creating a PIP as well. Compared to heavier species, like C, N, O, He is abundant at nearly the same distance behind the shock front, where the broad and narrow H α lines are created. HeI λ 584 Å and HeII λ 304 Å emission is the main source of the photons produced downstream. The HeII λ 304 Å photons alone can ionize the pre-shock gas up to 20% (Hamilton & Fesen 1988), and can also heat the gas to a temperature much higher than 10^4 K. The PIP precursor is undoubtedly present in non-radiative shocks, which was observationally confirmed in Tycho's SNR by Lee et al. (2007). However, the PIP deposits energy in electrons rather than ions, and thus suffer from the same conceptual problem as the electron thermal conduction precursor. This means that, rather than being excited, neutral hydrogen would be collisionally ionized before reaching the shock front.

- **Broad-neutral precursor:** Broad neutrals, created in CE processes between hot protons and slow neutrals downstream, have a bulk velocity of $3V_s/4$. Therefore, the fraction of the fast neutrals on the tail of the velocity distribution can have thermal velocities higher than the shock velocity. Those that have net velocities toward the shock front can cross it and enter the pre-shock region. Once they reach the upstream region, they undergo CE with the cold, pre-shock protons creating a population of hot protons and slow neutrals (opposite to CE downstream). The hot protons share their energy with the pre-shock electrons, which then can heat slow neutrals and broaden narrow Balmer emission. The result is very sensitive to the pre-shock neutral fraction, shock velocity and electron-ion equilibration. The first models that include this precursor were introduced by Lim & Raga (1996). Only recently Blasi et al. (2012) and Morlino et al. (2012) have put forward detailed calculations on the shock modification in the presence of this precursor, and its effect on the observed Balmer lines (see Section 2.4.2). The main result of this state-of-the-art model is that this precursor does not affect significantly the width of the narrow component, but rather introduces a third, intermediate component to the H α line, with a width of ~ 150 km s $^{-1}$.
- **Cosmic-ray (CR) precursor:** Models of diffuse shock acceleration (DSA) require a CR precursor (Blandford & Eichler 1987)⁵. A CR precursor consists of Alfvén wave turbulence created by CRs streaming away from the shock. Alfvén waves dissipate their energy in the pre-shock gas through collisions and CE. This process heats and compresses the gas, broadening the narrow line. The narrow component width could reflect the precursor temperature, Alfvén turbulence, or both. The advanced shock model which includes CR physics (Morlino et al. 2013b) and its application to observations, will be discussed in the Section 2.4.2 and in the outlook chapter.

⁵See also Chapter 1, Section 1.5.1

2.3 BROAD $H\alpha$ -LINE PROFILES

In the previous section we have seen how the narrow $H\alpha$ -line width and profile can be used to trace the conditions in the shock. The same conditions can also affect the broad $H\alpha$ component through its width and profile. The two-component line reflects the velocity distributions of the pre-shock and post-shock gas. It is common to assume that these distributions are isotropic Maxwellian distributions, and the information on the lines is usually extracted by fitting two Gaussians, one for the narrow and the other for the broad component. However, there are certain processes which can introduce the departure from the Maxwellian distributions, and have potentially been observed in the broad $H\alpha$ line (Raymond et al. 2010). Apart from geometric effects, three physical possibilities have been put forward.

First, broad neutrals are considered to negligibly interact among themselves, which implies that every time a neutral participates in CE becomes a part of a new velocity distribution. It was estimated that every atom experiences around three CE before being ionized and swept-up into the post-shock proton population (Heng & McCray 2007). The assumption of Maxwellian distribution here stands when CE is a dominant interaction process in the transition zone, i.e., when the shock speed is $V_s \leq 2500 \text{ km s}^{-1}$. If the shock velocity is higher than 2500 km s^{-1} , CE is not any more the dominant process and broad neutral velocity distribution can significantly deviate from the Maxwellian.

Secondly, when a slow neutral becomes ionized, the created cold proton is taken by the magnetic field, starts gyrating around its lines and is re-energized. Those protons form a ring beam in the velocity space due to gyro motions around and their motion along the magnetic lines. This distribution of so-called pick-up ions is unstable and relaxes to the bi-spherical distribution symmetric about the magnetic field direction. Raymond et al. (2008) calculated pick-up ions effect on the broad $H\alpha$ -line profile. They showed that summed-up velocity distribution of thermal protons and pick-up ions result in a peak with a sharp cutoff and high velocity wings from the thermal distribution. In case we have laminar magnetic field and high neutral pre-shock fraction, pick-up ions can form a precursor and also affect the narrow line. However, it remains still unclear how the narrow component will be affected by such a precursor.

Thirdly, if SNRs accelerate CRs, the post-shock proton distribution will deviate from the Maxwellian distribution by having a core and power-law tails, a so-called κ distribution. In order to produce detectable power-law wings, a large number of hot protons should be converted to CRs.

All three processes can narrow the broad line width and underestimate the post-shock gas temperature. Also, in case they form the precursor, they can possibly broaden the narrow component. This would also result in lowering the broad-to-narrow intensity ratio. In the next section we will see how one can convert the observables, the line widths and their intensities into physical

parameters, namely shock velocity (V_s) and electron-proton equilibration (β) using the state-of-the-art shock models. We will also introduce some empirical relationships between β and V_s , and discuss the effect of a CR precursor and a broad-neutral precursor on the shape of the broad H α component.

2.4 SHOCK MODELS

The first shock models started developing right after Chevalier & Raymond (1978) proposed the mechanisms for producing the two-component H α lines. Chevalier et al. (1980) modeled optical emission from a strong adiabatic shocks, and got the first shock velocity and distance estimations for Tycho's SNR. The shock velocity was calculated from the broad component width W which is determined by the proton temperature downstream and the assumption of the Maxwellian post-shock proton distribution. The intensity ratio between broad and narrow components (I_b/I_n) also depends on the shock velocity, because CE cross section is a strong function of V_s . This implies another way of shock velocity determination. Also, both W and I_b/I_n depend on the electron-proton thermalization downstream β .

The subsequent shock models are based on the same principles as the model of Chevalier et al. (1980). The model of Ghavamian et al. (2001) includes the more complete treatment of the shock transition zone and Monte Carlo calculations of Lyman line trapping put forward by Chevalier et al. (1980). Ghavamian et al. (2007) established an empirical relationship between β and V_s using measurements in several SNRs and the model of Ghavamian et al. (2001), where they found linear relationship $\beta \propto V_s$ for $V_s \lesssim 400 \text{ km s}^{-1}$, and $\beta \propto V_s^{-2}$ for $V_s \gtrsim 400 \text{ km s}^{-1}$. They suggested the electrons can be heated with lower hybrid waves in a CR precursor and predict the relationship $\beta \propto V_s^{-2}$. Lower hybrid waves are longitudinal oscillations of ions and electrons in magnetized plasma, directed nearly perpendicular to the magnetic field, with the frequency of the geometric mean of the electron and ion gyrofrequencies. The formation of this wave helps energy exchange between ions moving perpendicular to the field lines and electrons moving along the field lines in the collisionless shock.

Determination of β is still an unsolved problems in the theory of collisionless shocks. The jump conditions do not determine the temperature of the individual particles, but the mean temperature behind the shock front. One way of estimating β is to determine T_e from X-ray observations and T_p from optical observations, i.e., the width of the broad H α component. However, the X-ray emission usually does not spatially coincide with the Balmer emission. Balmer emission arises from the region just behind the shock front, while X-ray emission might come from the region further downstream. This spatial inconsistency can introduce a significant error in the estimation of β . On the other hand, the width of the broad H α component and I_b/I_n depend on β and provide

a unique opportunity to estimate the degree of electron-ion thermal equilibration.

Based on atomic cross sections, Heng & McCray (2007) presented a formalism for computing the broad neutral velocity distributions, rate coefficients and probabilities for atomic interactions. In the shock models without precursor, neutrals and ions in the pre-shock region are assumed to be in local thermal equilibrium. Using a Dirac-delta function in velocity space to approximate the narrow $H\alpha$ line, the model of Heng & McCray (2007) predicts theoretical values for W and I_b/I_n as a function of V_s and β . Assuming that broad neutrals and post-shock ions in the transition zone have the same temperature, Heng et al. (2007) computed spatial emissivity profiles of the narrow and broad $H\alpha$. Furthermore, van Adelsberg et al. (2008) included Lyman line trapping and the effects of multiple charge exchange processes on the broad neutral population into calculations. They also relaxed the assumption on the thermal equilibrium between broad neutrals and post-shock ions in the transition zone.

There are several models that account for the effect of precursors on the shock dynamics. Models with a broad-neutral precursor have only recently started to develop. Ohira (2012) approximated broad neutrals' behavior as fluid and showed that the leaking particles decelerate the upstream flow and affect the shock compression ratio. However, this approach is adequate only for collisional shocks, because the length scales involved here are much smaller than the equilibration scale. Blasi et al. (2012) use fluid equations for describing ions and Vlasov equation to describe the interaction between neutrals and ions. This interaction was computed on both sides of the shock front. Following the approach of Blasi et al. (2012), Morlino et al. (2012) calculated the $H\alpha$ emission profiles produced in the broad-neutral precursor. They showed that the profiles deviate from Gaussian and that this precursor can introduce an intermediate width component of $\sim 150 \text{ km s}^{-1}$.

The shock models with the CR precursor were initiated by Boulares & Cox (1988) who calculated the heating and ionization in the CR precursor for lower shock velocities. Wagner et al. (2009) computed ionization, emission and heating in a CR precursor treating CRs and neutrals as fluids. Similarly, Raymond et al. (2011) computed the temperature, density and $H\alpha$ emission in the CR precursor. Morlino et al. (2013b) have extended the model of Morlino et al. (2012) by including a CR precursor. They found that the width of the narrow $H\alpha$ component depends on the level of turbulent heating and the maximum momentum. The latter leads to a larger CR precursor, where upstream neutrals have higher probability to experience CE and gain some energy. While the calculations show that the level of turbulent heating does not significantly affect the width of the broad component, larger turbulent heating increases the width of the narrow component.

2.4.1 VAN ADELSBERG ET AL.'S MODEL

We will introduce here the state-of-the-art shock model without precursors that we applied to our observations in Chapter 3. The model of van Adelsberg et al. (2008) is based on mathematical and physical formalism presented in the papers by Heng & McCray (2007) and Heng et al. (2007). Heng & McCray (2007) present calculations of velocity distribution functions for broad neutrals and broad-to-narrow intensity ratios as a function of the shock velocity and the density structure of the shock transition zone (Heng et al. 2007). The model has the following assumptions:

- The calculations are for plane-parallel, edge-on and non-radiative shocks;
- The broad line is optically thin to Ly β photons (Case A) to a very good approximation;
- The narrow line is typically between Case A and Case B (the line is optically thick to Ly β photons);
- The neutrals are considered to thermally equilibrate with the hot ions downstream after three CE processes;
- The contribution of He as a completely neutral upstream is taken into account;
- The calculations do not consider any precursor.

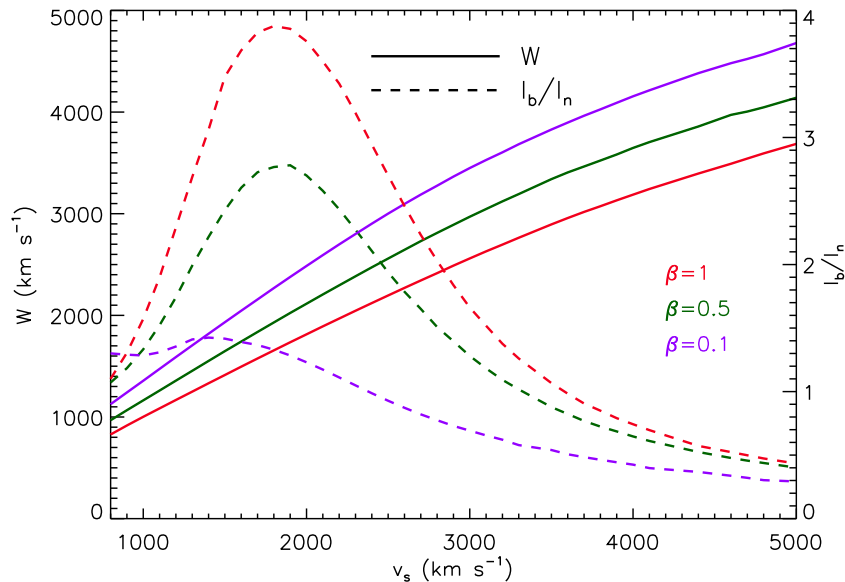


Figure 2.3: The width of the broad line W and the ratio of the broad to narrow line intensities I_b/I_n as a function of the shock velocity V_s and the electron-to-proton temperature ratio β based on calculations from the model of van Adelsberg et al. (2008) at upstream ionization fraction $f_{\text{ion}}=0.5$. Credit: Heng (2010).

By fitting two Gaussians to the observed $H\alpha$ line, one for the narrow and the other for the broad component, one extracts the widths of the components and the broad-to-narrow intensity ratio. Moreover, the shift between the velocity centroids corresponds to the shock inclination angle, i.e., the angle between the shock normal and the line-of-sight. In the absence of pick-up ions, edge-on shocks are expected to have zero offset between the narrow and broad $H\alpha$ line centers, while face-on shocks have an offset of $3/4$ of the shock velocity. Figure 2.3 shows the theoretical values for the broad line width and the intensity ratio as a function of V_s and β as predicted by the model of van Adelsberg et al. (2008); the results only weakly depend on the ionization fraction upstream f_{ion} .

2.4.2 MORLINO ET AL.'S MODELS

I. Shock model with broad-neutral (BN) precursor

The model of Morlino et al. (2012) is the state-of-the-art shock model which includes BN precursor. It is based on calculations introduced in the paper of Blasi et al. (2012) who showed that the fraction of returning neutrals can be up to 5%. The model of Morlino et al. (2012) is the first model that takes properly neutral distribution into account both downstream and upstream. The model assumptions are:

- The shock is non-radiative, plane-parallel and edge-on.
- Ions and electrons are described as a fluid (like in van Adelsberg et al. 2008), but neutrals interaction with ions is described with the Vlasov equation. Neutrals cannot be treated as a fluid, because on these timescales they can not reach thermalization. Newly produced ions (in CE and ionization) are in local thermal equilibrium with the bulk of ions.
- Neutral that experience few CE both upstream and downstream have a very anisotropic velocity distribution and are not Maxwellians. Their distribution is computed at every point in space and not volume integrated.
- He and heavier elements are neglected.
- Calculations include Lyman line trapping assuming that the narrow $H\alpha$ line is optically thick and the broad $H\alpha$ line is optically thin to $Ly\beta$ photons.
- A BN precursor is included into calculations through energy and momentum deposition on spatial scales defined by the cross sections for CE and ionization.

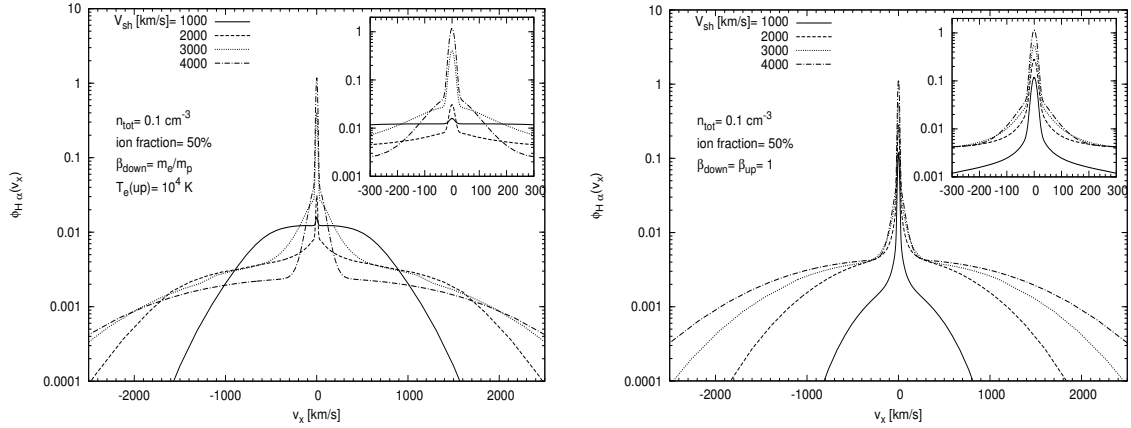


Figure 2.4: Volume integrated H α profiles for different shock velocities and fixed total ambient density and ionization fraction upstream. Shown are two cases, where there is no equilibration at all (left panel) and the case of full equilibrium downstream (right panel). Top-right panels in both cases show the zoomed-in region close to the line core. Credit: Morlino et al. (2012).

The main result of these calculations is that the BN precursor can heat the pre-shock gas to $\sim 10^6$ – 10^7 K and introduce an intermediate H α component. The width of the intermediate component reflects temperature in the precursor and has a non-Gaussian profile due to hydrogen atoms contributions from different locations in the precursor that have different temperatures. For shock velocities between 1000 and 5000 km s $^{-1}$, its width is in the range between 100 and 300 km s $^{-1}$. In the case of full equilibration both downstream and upstream ($\beta_{\text{down}} = \beta_{\text{up}} = 1$) a significant emission of the H α (narrow component) arises in the pre-shock region with a peak for $V_s \approx 2500$ km s $^{-1}$ and reaches $\approx 40\%$ of the total emission. Moreover, lowering β_{up} down to 0.05, there is still non-negligible emission upstream being around 10% of the total emission. All the components of H α line depend on V_s , f_{ion} and β (Figure 2.4). For $V_s \lesssim 1500$ km s $^{-1}$, the contribution of the intermediate component to the overall H α line is negligible. It is most prominent for $V_s \approx 2000$ km s $^{-1}$ and for lower f_{ion} . When β_{down} increases the intensity and the width of the broad H α component decreases because the electrons contribute to ionization of neutrals. This also affects the intermediate component since the number of broad neutrals travelling upstream is suppressed. Another very important result is that the width of the narrow H α component remains unaltered by this precursor. The reason lies in the fact that the precursor is thinner than the CE length for cold, pre-shock neutrals regardless the shock velocity, ambient density and ionization fraction upstream. Finally, the BN precursor affects the spectrum of the particles accelerated in the shock by lowering the compression ratio which implies steeper decline in the spectrum.

II. Shock model with broad-neutral (BN) and cosmic-ray (CR) precursor

Morlino et al. (2013b) extended the shock model with the BN precursor including the effects of the CR precursor on the shock structure and H α line. Malkov & Drury (2001) pointed out that large CR pressure can induce a CR precursor with a typical spatial scale of the order of the diffusion length of the highest energy particles. The model of Morlino et al. (2013b) includes four components and the interactions between them: thermal particles (protons and electrons), neutrals (hydrogen atoms), accelerated protons (hadronic CRs) and turbulent magnetic field. The non-linear diffuse shock acceleration theory in partially neutral medium was included following the approach of Amato & Blasi (2005) for the treatment of the CR distribution and Amato & Blasi (2006) for the description of the transport equation for waves. This model considers two types of heating in the CR precursor, adiabatic heating, i.e., pre-shock gas deceleration⁶ in the precursor, and turbulent heating where the magnetic turbulence is initiated by the CRs. It is shown that if there is no turbulent heating, the adiabatic compression moderately heats the pre-shock gas. Increasing the level of turbulent heating, downstream temperature remains almost unchanged and, thus, also the width of the broad H α component, but the narrow H α component is being broadened. The width of the narrow component depends on the level of turbulent heating and the precursor thickness. The width of the intermediate H α component induced in the BN precursor is also affected by the CR precursor, because the latter changes the distribution of neutrals upstream significantly. Therefore, the more efficient CR acceleration in the shock, i.e., the higher level of turbulent heating, the broader is the intermediate component. The CR acceleration efficiency is defined as $\varepsilon_{\text{CR}} = P_{\text{CR}}/(\rho_0^i V_s^2)$, where ρ_0^i is ion ambient density, and P_{CR} is CR pressure at the shock position. One of the results is also the linear decrease of the width of the broad line with ε_{CR} for ε_{CR} lower than 40%.

Apart from the precursors' effects on the shock dynamics, the important difference of Morlino et al.'s models from the model of van Adelsberg et al. (2008) is non-Gaussian velocity distribution of broad neutrals downstream. Van Adelsberg et al. assume that broad neutrals have the same distribution as the hot protons downstream after approximately three CE processes. This difference can significantly affect the estimated shock velocities (see Figure 2.5). Morlino et al.'s and van Adelsberg et al.'s results are consistent for $V_s \approx 2000 \text{ km s}^{-1}$. This is expected since for lower shock velocities, CE is the dominant process and neutrals would experience many CE before being ionized, thereby in this regime thermalization between ions and neutrals is a good approximation. Also, it is very hard to make strong conclusions on CR acceleration efficiency without prior constraints on electron-proton equilibration. However, if the measured broad line width is below the line where $\beta=1$, we can estimate the lower limit on CR acceleration efficiency (e.g. the triangles in Figure 2.5).

⁶in the rest frame of the post-shock gas

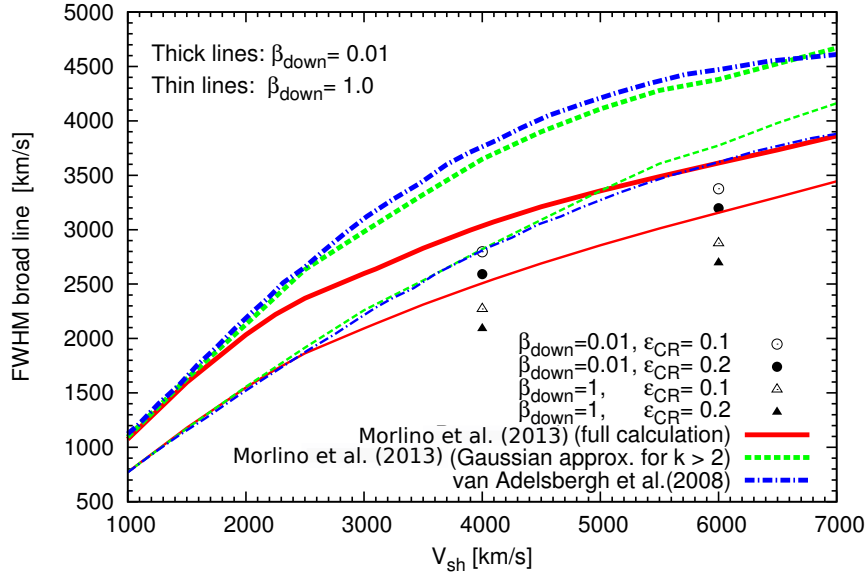


Figure 2.5: The predicted broad $H\alpha$ line widths as a function of V_s and β computed in Morlino et al. (2013b) (solid and dashed lines) and van Adelsberg et al. (2008) (dot-dashed lines). The dashed lines show the Morlino et al. (2013b) predicted broad line widths following the assumption of van Adelsberg et al. (2008) that broad neutrals and ions thermalize after three CE. Circles and triangles show the broad line width calculated in the presence of CRs with acceleration efficiency 0.1 and 0.2 and shock velocities of 4000 and 6000 km s^{-1} . Credit: Morlino et al. (2013a).

In conclusion, the van Adelsberg et al.’s model can be successfully used for describing two-component $H\alpha$ lines in low velocity shocks where one does not expect efficient CR acceleration to occur. Morlino et al.’s models with the BN and CR precursors have shown that the first precursor is responsible for the appearance of the intermediate $\approx 150 \text{ km s}^{-1}$ $H\alpha$ component, while the second causes broadening of the narrow $H\alpha$ component beyond 20 km s^{-1} . Applying the latter models to our data (see the outlook chapter), we will be able to distinguish among the contributions that arise from different precursors in the shock, which is an important step forward in understanding the structure of collisionless shocks.

2.5 SPECTRO-PHOTOMETRIC TECHNIQUES FOR STUDYING OPTICAL SHOCKS

Spectroscopy is one of the fundamental tools in astronomy used to determine the chemical compositions, physical properties, and radial velocities of astronomical sources. It has applications throughout the entire electromagnetic spectrum. Since the main goal of our research is studying shock microphysics and better understanding the origin of cosmic rays (CRs), we have used high-resolution spectro-photometric imaging to accurately trace and isolate optical shock fronts around (super)novae. High *spectral* resolution of $\sim 100 \text{ km s}^{-1}$ and $\sim 10 \text{ km s}^{-1}$ is needed in order to resolve the broad and narrow H α lines respectively, while high *spatial* resolution ($\sim 0.1''$) is required to accurately quantify the fundamental properties of the shocks by eliminating geometric effects, i.e., to separate the contributions of bulk motion versus thermal velocity to the measured line widths. Having both high spectral and high spatial resolution, but also a large field-of-view (FOV) to cover the majority of the extended remnants' shells ($\sim 1'$), is very hard to achieve using a single instrument. Often several different techniques and instruments are necessary to meet these requirements. In the following sections of this Chapter, we will review the most commonly used observational techniques in our field of interest, but also introduce a novel observational approach for studying Balmer-dominated shocks (BDSs).

2.5.1 LONG-SLIT SPECTROSCOPY

Long-slit spectrographs are traditionally used in astronomy, particularly for spatially resolving spectra of extended objects like galaxies, HII regions, planetary nebulae, etc. As the name implies, they disperse the image from a long slit, allowing only a narrow region of the FOV to pass through. The resulting spectral image is two dimensional (x, λ), where one axis is the one-dimensional (1D) spatial direction (x) and one is the wavelength axis (λ). A three-dimensional (3D) data cube is produced by stepping long-slit observations in the spatial direction y . The width of the slit defines the spectral resolution of the instrument: the narrower the slit, the higher spectral resolution. On the other hand, lower slit width means we will have less flux per pixel on the detector. Thus, if we want to gain photometric accuracy, we will lose the wavelength resolution. Moreover, to achieve high spectral resolution of a wide field, one needs very high number of telescope pointings to cover the whole field. Also, long-slits are straight and, thus, unfit for studying geometrically complex regions, like shock curvature in our case. Considering all this, this spectroscopic mode is best suited for low spectral and spatial resolution mapping, and partial coverage of an extended but geometrically simple object. The advantage of long-slit spectrographs is that the slit width and length can be adapted to the desired goals; they are usually easy to use and provide for easy sky subtraction.

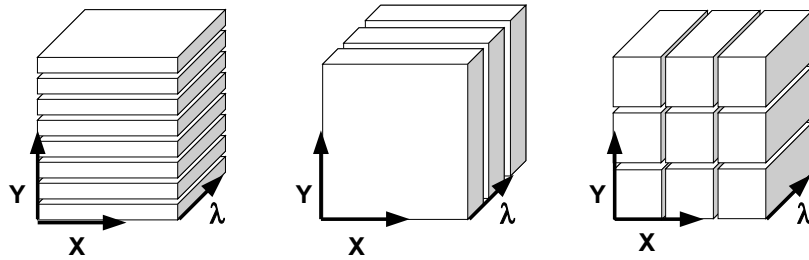


Figure 2.6: Constructing a spectroscopic data cube using long-slit (*left*), Fabry-Pérot & narrow-band tunable filter (*middle*), and integral-field spectroscopy (*right*). In the *left* cube, each slice is one long-slit spectrum; in the *middle* cube, each slice contains the full field imaged in one bandpass; in the *right* cube, each piece (spaxel) contains the full spectrum within a small field.

2.5.2 FABRY-PÉROT INTERFEROMETRY

A Fabry-Pérot interferometer (FPI) is a transparent plate with two semi-reflecting closely spaced surfaces. The reflectivity of the inner surfaces of the plates defines the spectral resolution, where higher reflectivity, i.e., reflective index of the surfaces, yields a better resolution. As narrow bandpass interference filter, FPI is also tunable, that is, the central frequency can be changed by varying the separation between the reflecting surfaces. An individual exposure is a slice (x, y, λ_0) , also called channel, that contains the full field imaged at and near one wavelength λ_0 . Performing a number of consecutive short exposures across the free spectral range⁷ (FSR) by altering the separation of the interferometer plates, one can produce a series of monochromatic images combined in a data cube. While FPIs have high resolving power (orders of ten thousands) and wide spatial coverage (FOV of several arcmin), they suffer from reduced total light throughput and are only effective across narrow bandpasses (small FSRs) on the order of few hundred km s^{-1} . Their disadvantage is also time-inefficiency in building the cube, similar to stepped long-slit spectroscopy. Moreover, this technique is sensitive to sky background that can change significantly during consecutive wavelength measurements, which makes accurate flat-fielding and flux calibration difficult to perform.

Low-resolution Fabry-Pérot can be used in place of narrow-band filters for flexible imaging purposes. The so-called imaging tunable filter can isolate a narrow spectral band from a broad, continuous spectral range, providing blocking-order filters in contiguous passbands. One example is the OSIRIS narrow-band tunable filter on the 10.4 m Gran Telescopio Canarias (GTC) in the low-resolution imaging mode of $\sim 100 \text{ km s}^{-1}$, which we have used to observe Tycho's SNR (see Section 4.6 in Chapter 4).

⁷Distance in frequency space between adjacent transmission maxima (interference orders).

2.5.3 INTEGRAL-FIELD SPECTROSCOPY

An integral-field spectrograph (IFS) is an instrument that combines spectroscopic and imaging capabilities, and is used to obtain spatially resolved spectra in astronomy. IF spectroscopy enables us to get the spectrum and its position on the sky simultaneously, i.e., a full data cube (x, y, λ) , in a single exposure. It is important to mention here that even though long-slit and Fabry-Pérot spectroscopy both create a data cube, these 3D imaging techniques are *non-simultaneous*. The term IF spectroscopy refers only to techniques which record spectra from each part of an object *simultaneously*. Comparison of the three different approaches to imaging spectroscopy and building of data cubes is illustrated in the Figure 2.6 and further explained in the Section 2.5.4 below. An IFS consists of the spectrograph and an integral-field unit (IFU) where the latter is used to divide the 2D spatial plane into a continuous array and is placed in front of the spectrograph. There are three different techniques of IF spectroscopy (Allington-Smith et al. 1998): lenslet arrays, fibre bundles and image slicers (Figure 2.7).

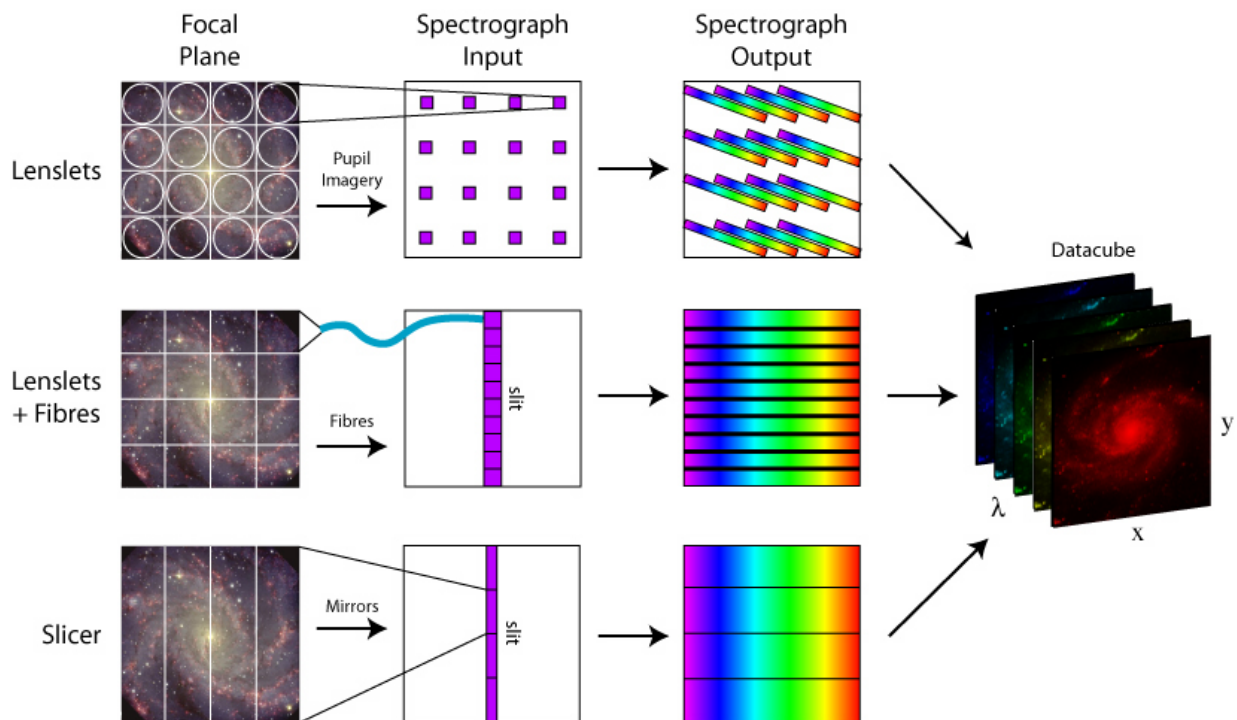


Figure 2.7: Illustration of the three different techniques of IFS: lenslet arrays, fibre bundles and image slicers. Credit: <http://ifs.wikidot.com/what-is-ifs>.

In the case of **lenslet arrays** method, we have microlens array (MLA) placed at the focal plane. Each lenslet produces a micropupil, a very small dot, to be then dispersed by a spectrograph. This

pupil imagery allows tilting of the MLA about the optical axis of the system so that we obtain a contiguously sampled input image. The number of spectra depends on the number of spatial elements in the IFU⁸. This method compromises spectral information, because of overlaps in the spectra that have to be corrected for. Moreover, it gives inefficient utilization of the detector surface (see spectrograph output in the Figure 2.7).

The **Fiber bundles** method consists of an array of optical fibers in the focal plane. Each fiber transmits the light to the spectrograph which is acting as a slit and rearranges the spectra to a line in its output. Without dithering, gaps between the fibers result in incomplete spatial coverage. This can be overcome by placing microlenses in front of the fibers, which will focus the light into the fiber and reduce the spatial losses.

The focal plane can be also divided into segments using a series of mirrors which project the segments to adjacent portions of a slit in the spectrograph. The **image slicer** technique retains spatial information within each slice, meaning that we have high information density in the data cube.

The FOV of IFSs is usually a few tens of arcsec squared with a spectral resolution of few thousands. This makes them particularly suited to IF spectroscopy of compact objects, distant galaxies, circumstellar disks and exoplanet systems. IFSs had been used before in infrared studies of SNRs, particularly SN 1987A (Kjaer et al. 2007), and classical novae (Lyke & Campbell 2009). Their application in optical studies of SNRs (Chapter 3) and classical novae (Chapter 5) have been introduced by our team.

2.5.4 COMPARISON OF DIFFERENT TECHNIQUES

The IF spectroscopy approach represents a compromise between wide field high-resolution Fabry-Pérot spectroscopy and narrow field low-resolution slit spectroscopy. Compared to FPI, IFS has much smaller field coverage, but a broader spectral coverage. On the other hand, spectral coverage of the IFSs is typically smaller than in stepped-slit spectrograph, but gives much more spatial information. Obtaining a data cube in a single exposure makes IFSs more efficient (about 10 times) than both long-slits and FPIs. Simultaneous acquisition of the whole data cube preserves spatial and spectral quality of the raw data, because changes in observing conditions (variations in seeing or atmospheric transmission) are negligible. This is not the case with stepped-slit techniques and FPIs. Also, IFSs provide higher signal-to-noise (S/N), thus making the studies of morphologically complex targets easier. A big advantage of long-slits and FPIs over IFSs is their higher spectral resolution.

⁸Within the IFU community it is often used a term *spaxel* – spatial pixel – to make a difference between a spatial element on the IFU and a pixel on the detector.

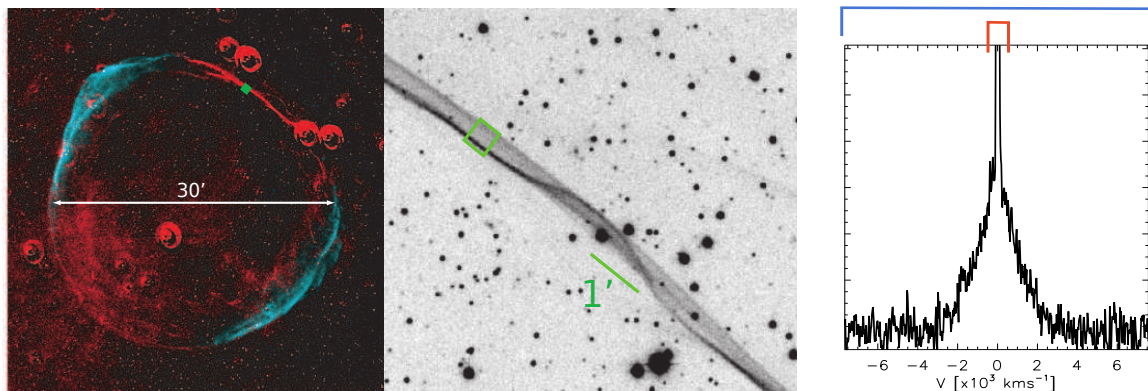


Figure 2.8: IFU observations of the northwestern (NW) rim of the supernova remnant SN 1006. The left panel shows a combined optical and X-ray image, adapted from Cassam-Chenaï et al. (2008). Shown are the Chandra synchrotron (2–4.5 keV; in cyan) and CTIO Curtis Schmidt narrow-band $H\alpha$ (in red) emission. The middle panel is a zoom-in of the NW rim in the optical image, clearly showing different shocks projected along the line-of-sight (Courtesy of Gamil Cassam-Chenaï and Jack Hughes). The remnant is about 30' across; the green box in both panels gives an approximate representation of the 27'' \times 27'' FOV of the VIMOS-IFU instrument that we used (see Chapter 3). The right panel shows one of approximately 2000 IFU spectra extracted from the green box. The blue bar indicates the large spectral coverage needed to detect the broad $H\alpha$ component, and red bar indicates the high spectral resolution (not achieved with this instrument) to resolve the narrow component.

Let us now summarize the characteristics of the shock fronts around (super)novae⁹ and the instrument requirements that we need to accomplish our scientific goals. BDSs are:

- very faint – we need very good instrument efficiency;
- often have a complex structure – we need high spatial resolution ($\sim 0.1''$);
- have a broad $H\alpha$ -line component ($\sim 1000 \text{ km s}^{-1}$) – we need a large spectral coverage;
- have a narrow $H\alpha$ -line component ($\sim 10 \text{ km s}^{-1}$) – we need high spectral resolution;
- are extended objects ($\sim 1'$) – we need a large FOV.

At the moment, there is no a single instrument that can satisfy all the requirements. Therefore, we used the combination of IFU and Fabry-Pérot techniques to study BDSs around (super)novae (see Figures 2.8, 2.9 and Chapters 3, 4 and 5).

⁹The main difference between BDSs around supernovae and novae is ≈ 4 –5 times lower shock velocities (broad-line widths) in case of novae.

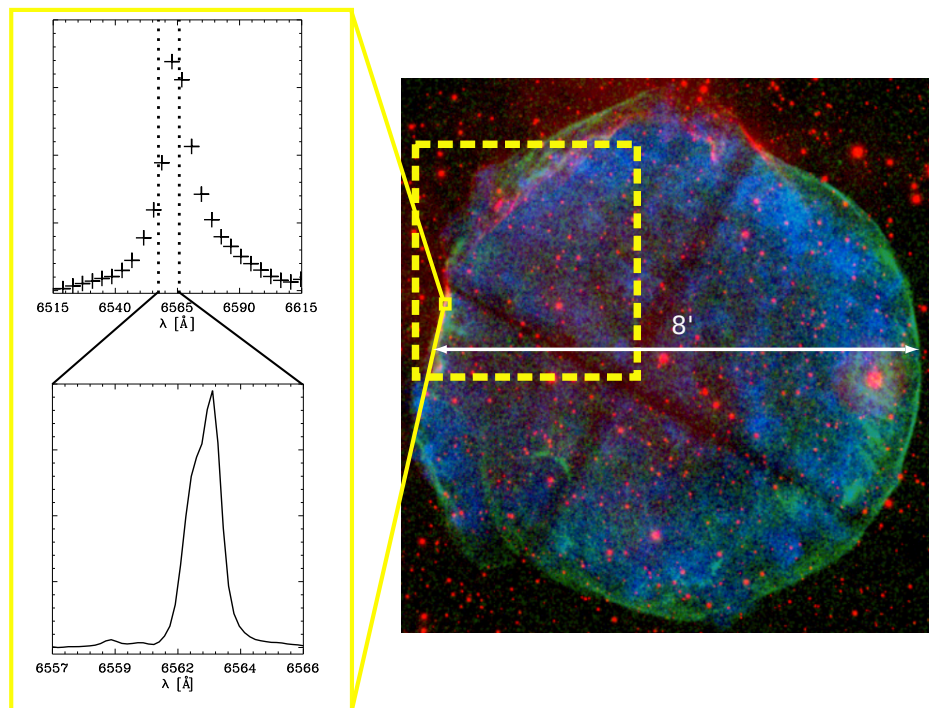


Figure 2.9: Fabry-Pérot observations of the Tycho SNR (diameter of $8'$, see Chapter 4). The right image is an $H\alpha$ narrow-band image of Tycho's SNR (red; courtesy P. F. Winkler), 3–8 keV hard X-rays (green), and 0.5–3 keV soft X-rays (blue). Both optical and X-ray images were acquired during the same epoch (2007). The yellow dashed box indicates a FOV of $4' \times 4'$ of the narrow-band tunable filter imager and Fabry-Pérot used to measure broad (top-left panel) and narrow $H\alpha$ component (bottom-left panel), respectively. The narrow $H\alpha$ line was not resolved with the former instrument (vertical dashed lines in the top-left panel). The shown spectra originate in the small yellow box within the dashed one.

2.6 SUMMARY

The purpose of this chapter was to introduce the reader to BDSs from both theoretical and observational point of view. In the first part, we have reviewed the current shock theories including state-of-the-art models, and have also discussed the effects on the observables. In the second part, we have summarized commonly used techniques for observing BDSs around (super)novae, but also introduced a novel observational approach that we used, which results are presented in the following chapters.

BALMER-DOMINATED SHOCKS AROUND SN 1006*

ABSTRACT

Supernova remnants are among the most spectacular examples of astrophysical pistons in our cosmic neighborhood. The gas expelled by the supernova explosion is launched with velocities $\sim 1000 \text{ km s}^{-1}$ into the ambient, tenuous interstellar medium, producing shocks that excite hydrogen lines. We have used an optical integral-field spectrograph to obtain high-resolution spatial-spectral maps that allow us to study in detail the shocks in the northwestern rim of supernova 1006. The two-component $H\alpha$ line is detected at 133 sky locations. Variations in the broad line widths and the broad-to-narrow line intensity ratios across tens of atomic mean free paths suggest the presence of suprathermal protons, the potential seed particles for generating high-energy cosmic rays.

3.1 INTRODUCTION

Supernova remnants, the expanding shells of material created in a stellar explosion, are astrophysical laboratories for studying non-thermal physics and high-velocity shocks, and have been scrutinized over a broad range of wavelengths. The signatures of non-thermal electrons are typically manifested in the X-ray, γ -ray and radio range of wavelengths (Reynolds 2008). Complementary to these observations, hydrogen emission from “Balmer-dominated shocks” (Chevalier & Raymond 1978; Bychkov & Lebedev 1979; Chevalier et al. 1980), around supernova remnants of thermonuclear origin, directly probe the proton populations (Heng 2010). Until now, all

*This chapter is adapted from the paper Nikolić S., et al., 2013, *Science*, 340, 45: *An Integral View of Fast Shocks around Supernova SN 1006*.

studies of Balmer-dominated shocks have typically used conventional spectrographs that yield rich spectral information but limited spatial information. Here we report on Balmer-dominated shocks around a supernova remnant using integral-field unit (IFU) spectroscopy, a technique that produces a three-dimensional “data cube”: two dimensions of space (across the sky) and a spectral dimension. We selected supernova (SN) 1006 as our target, because it has a long history of serving as a laboratory for studying non-thermal physics and high-velocity shocks (Acero 2010; Koyama et al. 1995; Berezhko et al. 2002; Winkler et al. 2003; Rothenflug et al. 2004; Cassam-Chenaï et al. 2008; Petruk 2009).

Long-slit spectroscopy, utilized in previous studies of Balmer-dominated shocks (Ghavamian et al. 2002), cumulatively measures the $H\alpha$ emission emanating from regions much larger than the characteristic length scale: the mean free path for interactions between hydrogen atoms and electrons or ions, $L_{\text{mfp}} \sim 1/n\sigma_{\text{ce}}$ (with n being the pre-shock number density and $\sigma_{\text{ce}} \sim 10^{-15} \text{ cm}^2$ denoting the typical cross section for charge exchange). With use of the inferred range of densities for the northwestern rim of SN 1006 of n from 0.15 to 0.40 cm^{-3} (Raymond et al. 2007; Long et al. 2003; Acero et al. 2007), we estimated that the $0.''67$ size of a pixel in our IFU observations corresponds to $\sim 5L_{\text{mfp}}$. The high spatial resolution allowed us to separate out the contributions of bulk motion versus thermal velocity to the measured line widths, an issue that has limited the interpretation of previous observations. It also enabled us to study the spatial variation of the line widths and ratios and hence changes in microphysics of a shock across several atomic mean free paths. To buttress the second point, we have intentionally chosen a field-of-view that zooms in on a region of simple geometry, implying that any substantial spatial variation detected cannot be due to variations in density caused by geometric or projection effects.

3.2 INTEGRAL-FIELD SPECTROSCOPIC OBSERVATIONS AND DATA REDUCTION

Our observations of the northwestern rim of SN 1006 were performed in queue mode on the nights of 2010 April 6, 11, 12, 13, and May 10, using the VIMOS (VIisible Multi-Object Spectrograph) in the IFU (integral-field unit) mode on the Very Large Telescope (VLT). The IFU was placed approximately $15'$ away from the remnant’s center, at coordinates $\alpha_{J2000} = 15^h02^m13^s.5$, $\delta_{J2000} = -41^\circ45'22''$. The overall exposure time of 6 hours accumulated in 10 exposures, all taken at air mass $\lesssim 1.60$ and seeing $\lesssim 1''.60$, enabled us to collect enough photons to reach the required signal-to-noise ratios (S/N). A dither pattern with small offsets between the individual exposures was applied in order to account for dead fibers. We have used a spatial scale of $0''.67$ per pixel in combination with the HR-Orange grism providing a field-of-view of $27'' \times 27''$ as well as a resolution of $R \approx 2650$ within the wavelength range of $5250 \text{ \AA} \lesssim \lambda \lesssim 7400 \text{ \AA}$.

The data has been reduced with our own dedicated data reduction pipeline which was developed in particular to deal with the rather complex VIMOS instrument in IFU mode. It is based on several individual scripts written in the software language python. VIMOS is made of four identical optical quadrants, each representing a completely independent spectrograph. Each quadrant is at first reduced separately, including the following standard procedures: bias subtraction, straylight correction, interactive fibre-identification and -tracing, spectra extraction and wavelength calibration using the arclamp frames. For the extraction of the fluxes the “optimal extraction algorithm” was applied (Sharp & Birchall 2010), which was designed to deal with dense packed IFUs to correct for the cross talk between adjacent fibres. The associated continuum lamp frames were used to construct corresponding fibre-flatfields which were used to normalise the wavelength-dependent throughput of each fibre. Additionally, VIMOS also suffers from substantial distortions on the raw frames due to instrumental flexure. Thus, in order to guarantee the best possible extraction results the fiber traces were smoothed and corrected for shifts between science and calibration frames. This included a 2nd order correction of the absolute positions of the traces as well as an adjustment of the wavelength solution by using the available strong night-sky emission lines within the observed wavelength-range. The raw frames were cleaned for cosmic rays using the newly developed software package PyCosmics (Husemann et al. 2012), which represents an optimized algorithm to detect their artifacts in IFU raw-data.

After the basic reduction steps the four individual science frames for each observing block were combined and rearranged into three dimensional datacubes, using the dedicated VIMOS lookup-tables. Flux calibration was achieved by reduction and extraction of photometric standard stars which were observed using the same setup as the science data. As the VIMOS-IFU does not have “sky-dedicated” fibers, it is normal practice to do separate offset “sky exposures”, but in this case the sky background could be reliably measured from the “empty” downward triangular part in the field-of-view (see top-right panel of Figure 3.1). The last step involved the correction of the barycentric Doppler shift, i.e., the offset in velocity space caused by the movement of the Earth around the Sun. The observations were accomplished within a time-window of approximately one month, causing a velocity shift of about 20 km s^{-1} which corresponds roughly to one pixel on the detector. In order to readjust this offset we measured the center of the narrow $H\alpha$ emission line and shifted it to the laboratory wavelength of 6562.8 \AA .

The $H\alpha$ line is found in the middle of the HR-Orange grism wavelength range of $5250\text{--}7400 \text{ \AA}$. This spectral range is broad enough to both easily fit the broad component of the $H\alpha$ line with width of the order of 50 \AA , and to still leave plenty of spectral range for an accurate determination of the continuum. Finally, we used the precise header information of the telescope-pointings to compute the spatial-offsets between each observation and combined all ten individual datacubes within one final cube, containing in total 2162 spectra. The instrumental resolution of about 110 km s^{-1} (FWHM) around the wavelength of $H\alpha$ is more than sufficient to measure the width

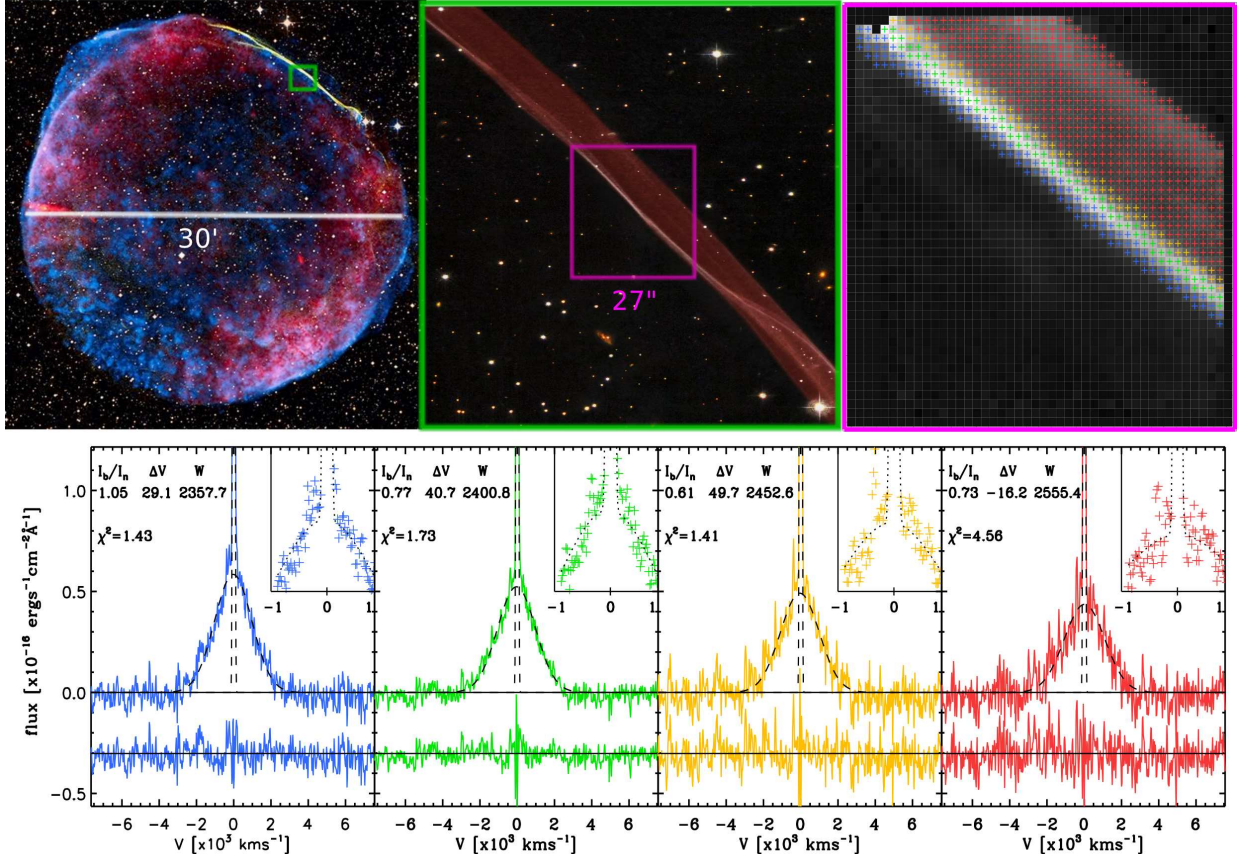


Figure 3.1: VIMOS-IFU spectroscopy of the shock front in the remnant of SN 1006. The *top-left* panel shows a composite image of the full remnant ($\approx 30'$ in diameter), combining data from the Very Large Array and Green Bank Telescope (red; NRAO/AUI/NSF/GBT/VLA/Dyer, Maddalena & Cornwell), Chandra X-ray Observatory (blue; NASA/CXC/Rutgers/G. Cassam-Chenaï, J. Hughes et al.), 0.9 m Curtis Schmidt optical telescope (yellow; NOAO/AURA/NSF/CTIO/Middlebury College/F. Winkler), and Digitized Sky Survey (orange and light blue stars). The green box indicates the region covered by the Hubble Space Telescope (HST) $H\alpha$ narrow-band image shown in the *top-middle*, with subsequently the magenta box indicating the region observed with the VIMOS-IFU. The *top-right* panel shows the reduced data cube collapsed in wavelength around the $H\alpha$ -line, recovering the shock front. The crosses with four different colors indicate the pixels for which the spectra have been combined to produce the spectra shown in the four panels at the *bottom*. In each of the bottom panels, the dashed black lines show the best-fit double-Gaussian, with parameters given in the legends: the intensity ratio of the broad to narrow component I_b/I_n , the velocity offset between the broad and narrow line centroids ΔV (in km s^{-1}), and width of the broad component W (in km s^{-1}). The reduced χ^2 values above unity along with the differences between the observed spectra and their best-fits (shown below the spectra with an offset of -0.3 for clarity), indicate that non-Gaussianity is present. Most of the reduced χ^2 values above unity come from the mismatching near the line core, as can be seen from the zoomed-in region ($-1000, 1000$) km s^{-1} in the top-right corner of bottom panels. On the horizontal axis is shown only the fitted region of the spectra, while the y axis shows the flux in units of $10^{-16} \text{ erg s}^{-1} \text{ cm}^{-2} \text{ \AA}^{-1}$ rescaled with the respect to the blue panel by factors 2 and 0.5 for the yellow and red panel, respectively.

of the broad line of $2000\text{--}3000\text{ km s}^{-1}$, as well as deviations from a Gaussian profile. The width of the narrow line, expected to be about 20 km s^{-1} , cannot be resolved, but the narrow line intensity can be accurately measured, especially given that the narrow line has a significantly higher S/N than the broad line.

3.3 DATA ANALYSIS

Figure 3.1 illustrates the general configuration of our observations performed with VIMOS in the IFU mode on the VLT. We have focused on the northwestern rim, because it produces the brightest emission from a Balmer-dominated shock. As a first analysis of our data, we divided the shock structure into four strips and bin up the data along each strip. The two-component $\text{H}\alpha$ line is convincingly detected. To first order, the broad line width (FWHM) W yields the shock velocity v_s , whereas the level of energy equilibration between electrons and protons in the post-shock gas introduces small corrections (Cargill & Papadopoulos 1988; Ghavamian et al. 2007). Because the broad line profile is a direct probe of the velocity distribution of the post-shock protons, and the narrow line profile traces pre-shock hydrogen atoms, the ratio of broad-to-narrow line intensities I_b/I_n contains information on how energy is shared between the pre- and post-shock regions. If no energy is shared, models which include the basic shock and atomic physics correctly translate the measured W and I_b/I_n values into the inferred v_s and β values (Ghavamian et al. 2002; van Adelsberg et al. 2008; Heng & McCray 2007; Heng et al. 2007), where β is the ratio of electron to proton temperatures in the post-shock gas. Unusually low I_b/I_n values ($\lesssim 0.7$) indicate that suprathermal particles from the post-shock region are traveling upstream into the pre-shock gas and depositing energy via atomic interactions (excitation, ionization and charge exchange), thus acting as precursors (Ghavamian et al. 2000; Sollerman et al. 2003; Lee et al. 2007). The loss of energy decreases the shock velocity and hence W . The increased flux of particles into the pre-shock region leads to enhanced excitation of the hydrogen atoms via collisions and increases I_n . The binned regions in Figure 3.1 already hint at this phenomenon, because $I_b/I_n \approx 0.6\text{--}0.7$ in two of the strips (yellow and red). The broad line exhibits subtle deviations from a Maxwellian profile in the line core, further supporting the presence of suprathermal particles in the shock.

We refined our approach by using the technique of Voronoi binning (Cappellari & Copin 2003). We combined neighbouring spectra into spatial Voronoi bins until S/N of about 40 was reached (see lower-right panel of Figure 3.2). We fitted double-Gaussians to the detected $\text{H}\alpha$ lines (for the fitting accuracy see Subsection 3.3.1) and derived W and I_b/I_n values, thus producing the maps in the top-left and top-middle panel of Figure 3.2. In addition to the lack of complex density variations, we demonstrated that the viewing geometry of the shock is simple: by measuring the

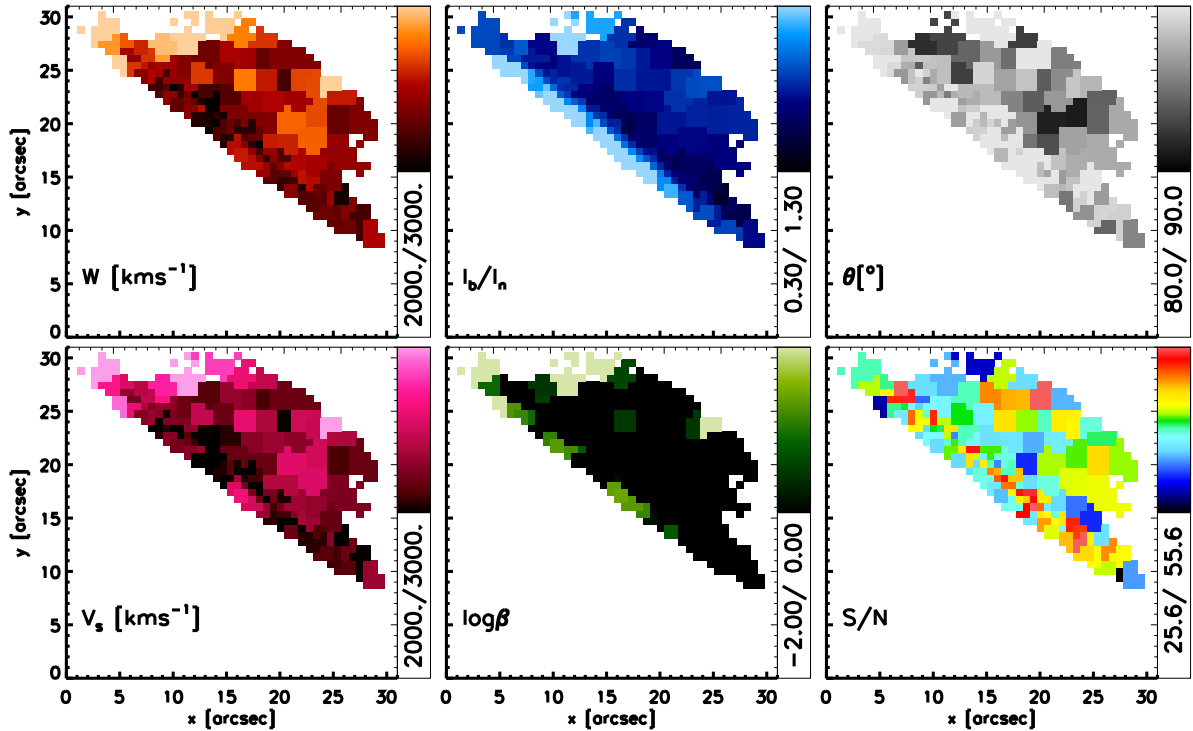


Figure 3.2: Two-dimensional spatial-spectral maps of various properties associated with the shock front in the remnant of SN1006. The *bottom-right* panel shows the spatial Voronoi binning to reach a minimum signal-to-noise $S/N \approx 40$. The maps in the *top row* from left to the right: the broad line width W (in km s^{-1}), the broad-to-narrow line intensity ratio I_b/I_n , and the shock inclination angle θ (in degrees). Shock velocities v_s and electron-to-proton temperature ratios β shown in the *bottom-left* and *bottom-middle* panels, respectively.

velocity shift ΔV between the centroids of the narrow and broad $\text{H}\alpha$ line components, we derived the viewing angle θ via the relation $\Delta V = 3v_s \cos \theta/4$. Our measurements indicate that $\theta \approx 80^\circ - 90^\circ$. Therefore, the shocks we observe are mostly edge-on as expected, but the rim seems slightly S-shaped along the line of sight as suggested by Raymond et al. (2007).

Surprisingly, we detected significant spatial variations in W and I_b/I_n across length scales $10'' \sim 70L_{\text{mfp}}$, despite the simple geometry of the shocks, suggesting that they arise from variations in the microphysics rather than density. Within the bright rim the variations in W are of order 10-20%, significantly larger than the individual measurement uncertainties (see Subsection 3.3.1 and Table 3.1 in Appendix). The density variations of 20-40% required to explain the detected variations in W are much larger than expected on these scales, and also incompatible with the unchanged smoothness of the shock over two decades of imaging observations (Winkler et al. 2003; Raymond et al. 2007). The low I_b/I_n values are found at all distances from the inner rim, reaching as low as 0.4 at some locations (Figure 3.3). We used the models without non-thermal

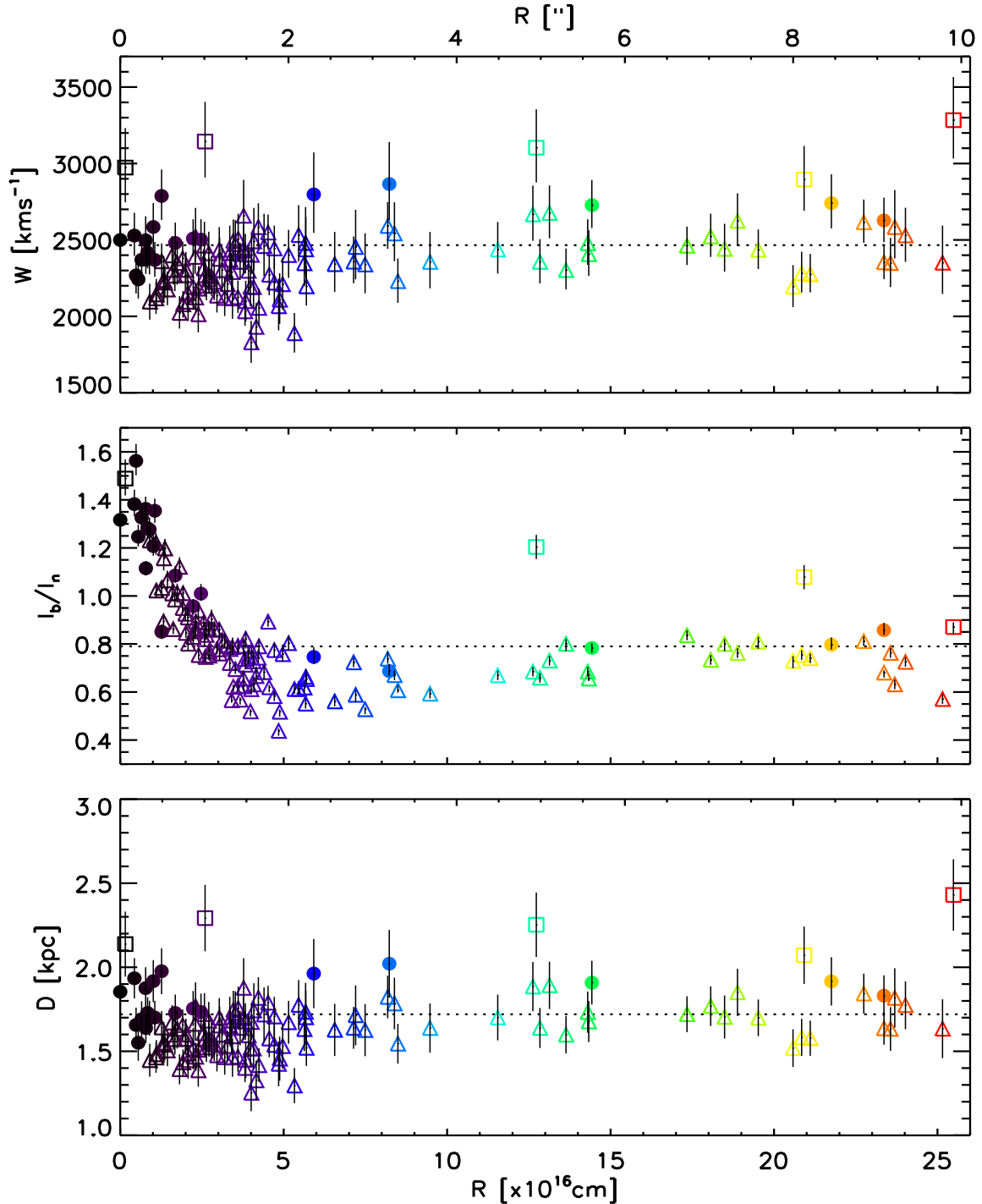


Figure 3.3: The three panels show all measured (with error bars) broad line widths W , broad-to-narrow intensity ratios I_b/I_n , and heliocentric distances D from combining the proper motion measurement with the shock velocities. Data are ordered in increasing distance from the inner rim (black/purple) to the outer rim (orange/red color), shown in arcsec at the top and in units of 10^{16} cm at the bottom horizontal axis. The inner rim coincides with the inner edge of the blue rim in the top-right panel in Figure 3.1. The dashed horizontal lines indicate the measured $W=2465.76 \text{ km s}^{-1}$ and $I_b/I_n=0.79$ values from collapsing all spectra of the pixels on the shock front, and from there the inferred $D=1.72 \text{ kpc}$. Data points marked with a filled circle are those for which a valid model solution is found. The triangles (squares) indicate that due to low (high) I_b/I_n values the models hit the lower (upper) boundary limit in β of 0.01 (1.0).

physics to infer the values of v_s and β (van Adelsberg et al. 2008). Most (about 85%) of the binned data are not accounted for by the model because of the low I_b/I_n values, thus motivating the need for models which include suprathermal particles and cosmic rays (Morlino et al. 2013b). Combining the derived shock velocities with the proper motion measurement from (Winkler et al. 2003), we obtained estimates of the heliocentric distance to SN 1006. Clearly, there has to be a unique distance, likely given by the upper points around ~ 2 kpc (see also Subsection 3.3.2). Most points, however, are underestimating the distance due to loss of energy from the broad line component resulting in too low inferred shock velocities.

3.3.1 ACCURACY OF THE H α -LINE FITTING

We fitted the H α line with two Gaussians, one for the narrow component and the other for the broad component, after convolving with a Gaussian instrumental profile. Hint on the non-Gaussianity around the line core of the broad component that we detected is a supporting, but not the main piece of evidence of suprathermal particles presence.

In order to investigate possible non-physical contributions to the H α -line profile, we compared the continuum emission profile across wavelength in the region downstream and upstream of the shock. As shown in Figure 3.4, we combined spectra in the downstream and upstream regions. The continuum has the same profile in these two regions, and does not affect the H α -line profile. In these regions we did, however, detect diffuse narrow-line H α emission, with surface brightness, 10-30 times lower compared to the emission in the four regions in Figure 3.1.

Next, to verify that the instrumental profile is Gaussian we fitted sky lines that went through the same data reduction steps (except for sky subtraction). In Figure 3.5, we show five sky lines around H α line fitted with a Gaussian. The fits together with the differences between the observed and fitted sky lines show that the instrumental profile is indistinguishable from Gaussian.

We have also checked if the residuals might be coming from the intrinsic variations among the individual spectra that went into the combined spectra. The offsets between velocity centroids are much smaller than the "extra-core" size, and thus rule out this possibility. Also, the individual bins have very similar narrow line widths that are always unresolved, but much smaller than the "extra-core" size.

Finally, the uncertainties in measuring the broad line width W and broad-to-narrow intensity ratio I_b/I_n were determined in various independent ways, taking into account the varying noise per pixel in wavelength as given by the derived error spectrum per pixel. Two of the methods were very robust and led to consistent error estimates even in case of spectra with signal-to-noise significantly lower than our target $S/N \approx 40$. In the first method, we created 1000 mock spectra

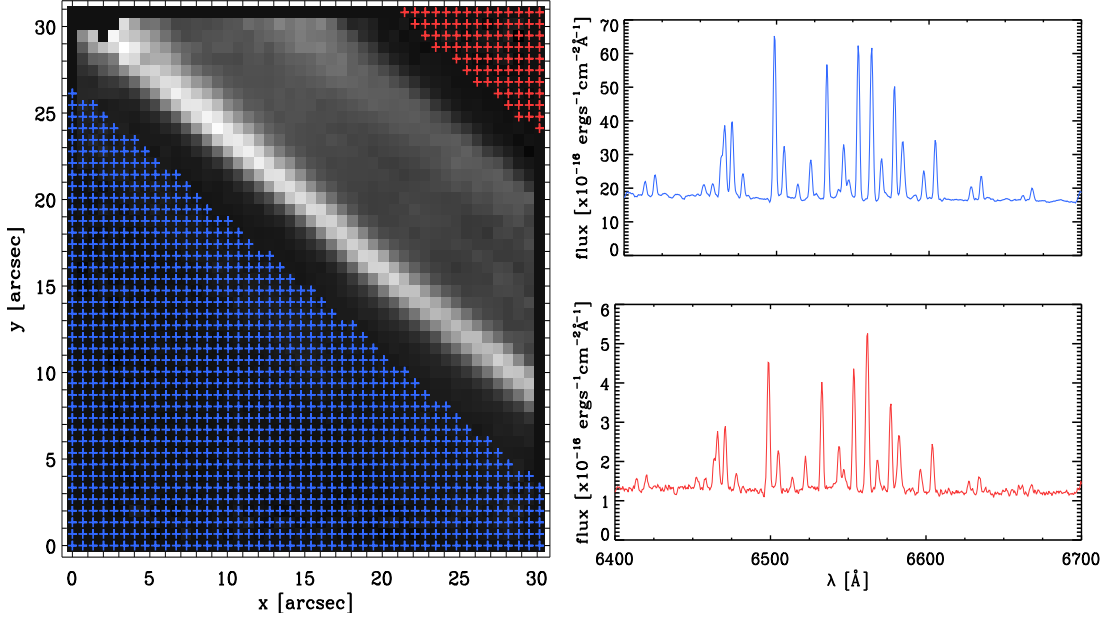


Figure 3.4: The *left* panel shows the reduced data cube collapsed in wavelength around the $H\alpha$ line with blue and red crosses indicating the pixels for which the combined non-sky-subtracted spectra are shown in the *right* panels. Comparing the continuum emission across wavelength, we confirm that the emission profile is the same in the upstream and downstream region of the shock.

per Voronoi bin through Monte Carlo sampling of the observed (combined) spectrum, and fitted each mock spectrum with a double Gaussian. The resulting distributions of values in W and I_b/I_n shows that both quantities are uncorrelated and their means are the same as from the fit to the observed spectrum. Their standard deviations, however, are slightly larger than those from the second method in which we varied¹ W and I_b/I_n on a grid around their best-fit values until χ^2 changed by an amount corresponding to the 68% confidence level given the degrees of freedom. This is expected, as the first method, apart from the added noise from the error spectrum, also includes noise already inherent in the observed spectrum, increasing the reduced χ^2 values of the mock spectra fits above unity. Re-scaling the reduced χ^2 values to unity leads to uncertainties that are fully consistent with those inferred from the second method. The double-Gaussian fits to the $H\alpha$ -line profile in all 133 sky positions are shown in Figure 3.6. The resulting best fit parameters and uncertainties are given in Table 3.1, along with shock properties inferred using van Adelsberg models.

¹Keeping the total intensity $I_n + I_b$, narrow line width and centroids of the narrow and broad component fixed to their best-fit values.

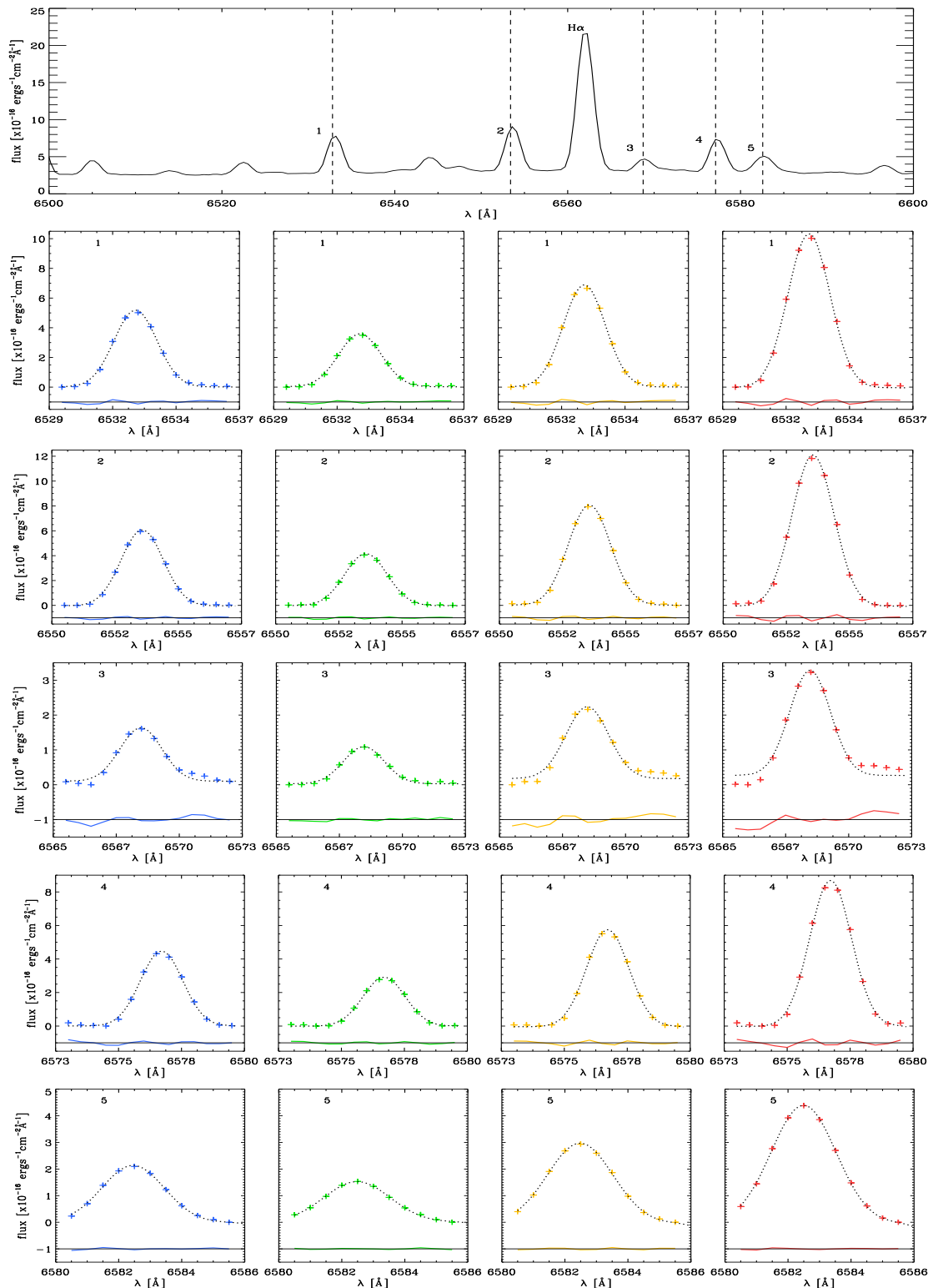


Figure 3.5: The *top* panel shows a non-sky-subtracted spectrum with five sky lines around H α , indicated by vertical dashed lines and numbered. Next, each *row* shows one sky line fitted with a Gaussian for the four different regions consistent with the ones in Figure 3.1. The fits along with the differences between observed and fitted sky lines (with an offset downward for clarity) show that the instrumental profile is Gaussian.

3.3.2 HELIOCENTRIC DISTANCE TO SN 1006

When converting from angular to physical length scales, $1'' \approx 2.58 \times 10^{16}$ cm, we adopted a heliocentric distance of 1.72 kpc, derived as follows. We first summed up all pixels on the shock front, and extracted the width of the broad component W and intensity ratio I_b/I_n by fitting the $H\alpha$ line with double-Gaussians. The resulting broad line width and broad-to-narrow intensity ratio are $W = 2466 \text{ km s}^{-1}$ and $I_b/I_n = 0.79$. Using the van Adelsberg et al. model, this yields a shock velocity of $v_s = 2288 \text{ km s}^{-1}$. Combining this shock velocity with the proper motion measurements of 280 mas yr^{-1} (Winkler et al. 2003) yields a heliocentric distance of 1.72 kpc.

Previously inferred distances to SN 1006 from the $H\alpha$ observations in the northwestern rim, 2.18 kpc (Winkler et al. 2003) and 1.6 kpc (van Adelsberg et al. 2008), were based on long-slit spectroscopic observations from (Ghavamian et al. 2002). The discrepancy in the inferred distances comes from different shock models applied. The latter one uses the same van Adelsberg et al. model, yielding a lower shock velocity for the same $W = 2290 \text{ km s}^{-1}$ and $I_b/I_n = 0.84$, primarily due to the broad neutral velocities contribution to the relative speeds in fast neutral-ion interactions.

Analysis of the optical spectrum of the Schweizer-Middleditch star (Burleigh et al. 2000) which lies almost at the same line-of-sight as the center of SN 1006, sets the upper limit on the distance of SN 1006 at 2.1 kpc. The observed ejecta expansion at 7026 km s^{-1} (Hamilton et al. 2007), and the requirement that this material lie within the remnant places a lower limit of 1.6 kpc. We actually expect the distance to be closer to ~ 2 kpc to explain the upper envelope of the points in Figure 3.3, but a model that properly takes into account the non-thermal physics is needed before we can robustly measure an intrinsic shock velocity and correspondingly obtain a secure estimate of the heliocentric distance.

3.4 DISCUSSION

The low values and variations of W and I_b/I_n , as well as the potential non-Gaussian contributions to the broad $H\alpha$ lines, demand an explanation. We examined three possibilities. The first is that “broad neutrals” are acting as a precursor (Lim & Raga 1996; Morlino et al. 2012). These are secondary populations of “hot” hydrogen atoms which are produced when post-shock protons capture an electron from a pre-shock hydrogen atom—the subsequent excitation of these broad neutrals produces the broad $H\alpha$ -line component detected in our observations (Chevalier & Raymond 1978; Bychkov & Lebedev 1979; Chevalier et al. 1980; Heng & McCray 2007). Broad neutrals will warm the pre-shock gas and produce a third $H\alpha$ -line component of intermediate width, which may account for the narrow-plus-broad-line double-Gaussian being unable

to fit the data within the measured uncertainties (i.e., not reaching a reduced χ^2 of unity). The strongest argument against broad neutrals is that they can only act as a precursor over an atomic mean free path, which is at odds with our observational result that the variations and low values of W and I_b/I_n extend over distances $\gg L_{\text{mfp}}$.

The second possibility is that pre-shock hydrogen atoms may cross the shock front, eventually become ionized and become protons gyrating along an ambient magnetic field line. It has been shown that these “pick-up protons” settle into a bi-spherical distribution which introduces a non-Gaussian contribution to the broad $H\alpha$ line core (Raymond et al. 2008). This explanation requires the magnetic field to be ordered on small length scales ($\ll L_{\text{mfp}}$), whereas turbulent magnetic fields will result in a broad $H\alpha$ line that is approximately Gaussian.

Both explanations are disfavored at low pre-shock neutral fractions, which is the situation in SN 1006 with a pre-shock neutral fraction of about 0.1 (Ghavamian et al. 2002). This is because both broad neutrals and pick-up ions require the pre-shock gas to contain a substantial population of hydrogen atoms (relative to electrons and protons) in order to initiate the process. In the limit of a fully ionized pre-shock gas, no broad neutrals or pick-up ions may be produced.

The explanation we favor is that the post-shock proton population includes a non-thermal sub-population of protons—suprathermal protons (that are not pick-up protons). Such an explanation requires no assumption on the magnetic field geometry or pre-shock neutral fraction. The lack of non-thermal X-ray and TeV γ -ray emission in the northwestern rim of the remnant indicates that if there is a CR precursor, the injection of electrons is little and the particle energies are low ($< 1\text{MeV}$), but CR acceleration can still happen.

3.5 SUMMARY

Our pilot project demonstrates the feasibility of using integral-field spectroscopy to observe and study the microphysics of high-velocity shocks around supernova remnants. The resulting high spatial resolution mapping of the Balmer-dominated shocks in the northwestern rim of SN 1006 suggests the presence of suprathermal protons of energies 10-100 keV which can seed high-energy cosmic rays.

Acknowledgements:

This work was supported by the IMPRS for Astronomy & Cosmic Physics at the University of Heidelberg. The paper is based on observations made with European Southern Observatory Telescopes at the La Silla Paranal Observatory under programme ID 085.D-0983.

3.6 APPENDIX

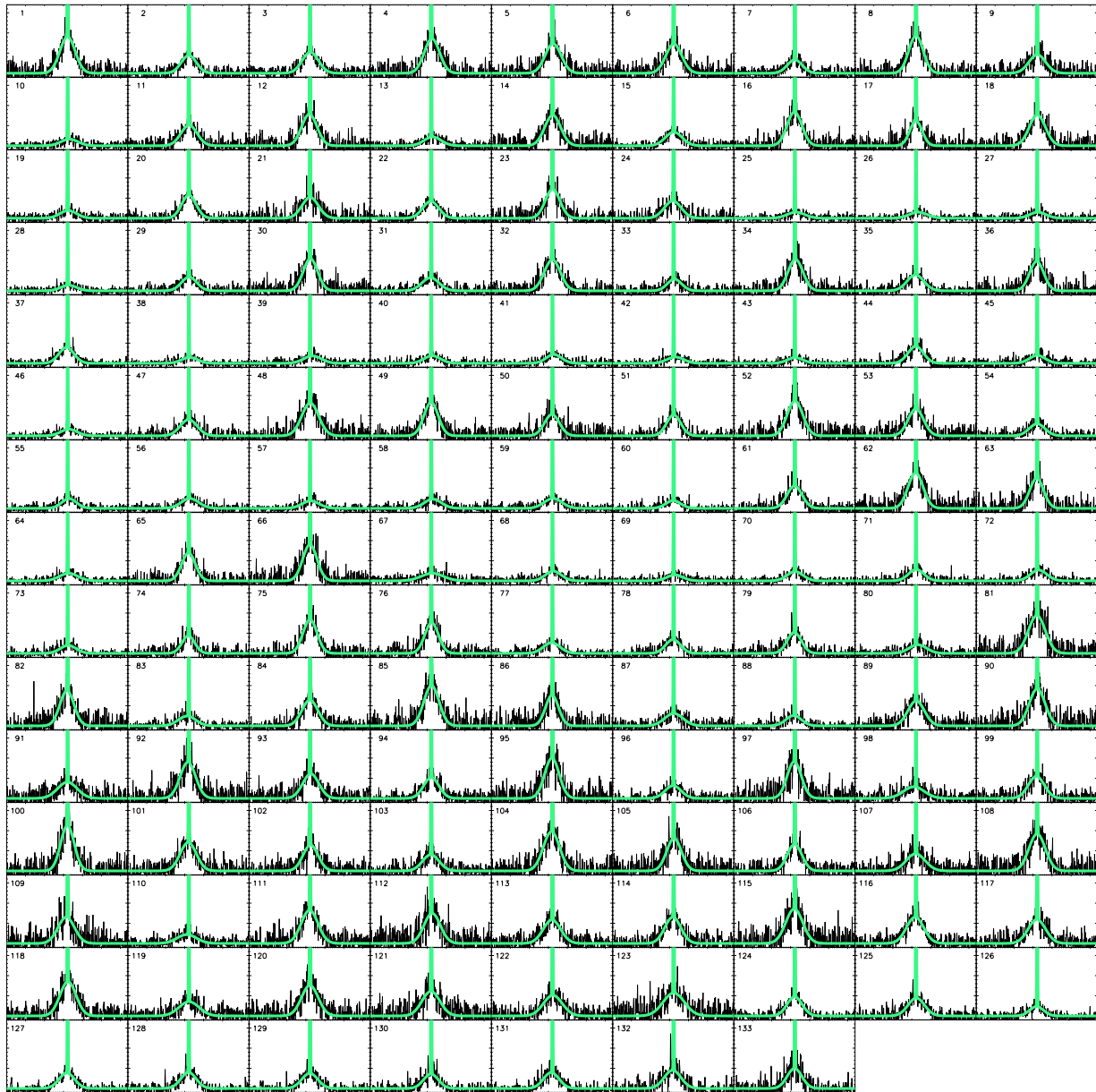


Figure 3.6: Montage of the $H\alpha$ line profiles in each of the 133 Voronoi bins. The horizontal axis represents wavelengths and vertical axis is in the relative units. Over-plotted are the double-Gaussian fits to the narrow and broad line components. No smoothing has been applied to the data.

Table 3.1: Properties of the shock front in the remnant of SN 1006 for 133 spatially binned locations. Columns 1–5: number of the (Voronoi) bin, x and y coordinates of the bin centroid, number of combined pixels, and signal-to-noise ratio. Columns 6–10: measured values of the broad component W and the broad-to-narrow line intensity ratio I_b/I_n (both with estimated uncertainties based on χ^2 68% confidence levels), shock inclination angle i (with typical uncertainty of 1.6° coming from a typical error of 47 km s^{-1} in ΔV), and the reduced χ^2 of the double-Gaussian fit to the observed $\text{H}\alpha$ -line. Columns 10–11: shock velocity v_s and electron-to-proton ratio β (in base-10 logarithm) of the best-fit shock model; a long dash indicates when the shock model hits the adopted boundary limits of $\log\beta = (-2, 0)$, likely because CR physics is missing.

Bin	x "	y "	Spx	S/N	W_{obs} km s^{-1}	$(I_b/I_n)_{\text{obs}}$	i_{obs} °	red. χ^2	v_s km s^{-1}	$\log\beta$
(1)	(2)	(3)	(4)	(5)	(6)	(7)	(8)	(9)	(10)	(11)
1	19.43	16.08	1	52.68	2268 ⁺¹¹⁰ ₋₉₄	0.93 ^{+0.03} _{-0.03}	89.3	0.91	2088	—
2	19.43	15.38	3	36.57	2242 ⁺¹³⁴ ₋₁₂₆	1.25 ^{+0.05} _{-0.04}	89.7	0.78	2058	-1.86
3	18.76	16.03	3	50.67	2417 ⁺¹¹⁰ ₋₁₀₂	1.28 ^{+0.03} _{-0.04}	89.1	0.91	2294	-0.95
4	20.10	15.41	1	44.70	2267 ⁺¹¹⁰ ₋₁₀₂	0.98 ^{+0.03} _{-0.03}	86.9	0.82	2087	—
5	20.10	16.08	1	48.21	2376 ⁺¹⁴¹ ₋₁₃₄	0.76 ^{+0.02} _{-0.03}	87.2	0.81	2194	—
6	19.43	16.75	1	50.81	2370 ⁺¹⁴¹ ₋₁₂₆	0.78 ^{+0.02} _{-0.03}	89.2	0.78	2189	—
7	20.24	16.79	3	44.35	2219 ⁺¹⁵⁷ ₋₁₄₁	0.58 ^{+0.02} _{-0.02}	89.5	0.81	2041	—
8	18.76	16.75	1	45.85	2124 ⁺⁹⁴ ₋₉₄	0.89 ^{+0.03} _{-0.03}	89.5	0.75	1948	—
9	20.77	16.08	1	36.70	2490 ⁺²²⁰ ₋₁₈₈	0.63 ^{+0.03} _{-0.03}	89.9	0.72	2313	—
10	20.93	18.06	8	38.61	2542 ⁺²⁰⁴ ₋₁₈₁	0.67 ^{+0.02} _{-0.02}	82.7	1.28	2368	—
11	18.85	17.42	2	51.71	2406 ⁺¹³⁴ ₋₁₂₆	0.71 ^{+0.02} _{-0.02}	89.3	0.92	2226	—
12	20.77	15.41	1	43.55	2266 ⁺¹¹⁸ ₋₁₁₀	0.77 ^{+0.02} _{-0.03}	86.7	0.81	2086	—
13	18.90	18.18	4	36.01	2531 ⁺¹⁹⁶ ₋₁₇₃	0.61 ^{+0.02} _{-0.02}	84.6	0.86	2357	—
14	18.09	16.75	1	44.23	2360 ⁺¹¹⁸ ₋₁₁₀	1.03 ^{+0.03} _{-0.04}	88.9	0.85	2179	—
15	17.76	16.39	4	38.21	2499 ⁺¹³⁴ ₋₁₁₈	1.32 ^{+0.05} _{-0.04}	89.7	0.89	2461	-0.81
16	18.09	17.42	1	51.08	2199 ⁺¹⁰² ₋₉₄	0.84 ^{+0.03} _{-0.02}	88.1	0.83	2021	—
17	18.09	18.09	1	38.59	1829 ⁺¹⁴¹ ₋₁₃₄	0.61 ^{+0.02} _{-0.02}	89.5	0.97	1663	—
18	17.42	17.42	1	43.81	2399 ⁺¹²⁶ ₋₁₁₈	1.01 ^{+0.04} _{-0.03}	89.5	0.79	2218	—
19	21.60	16.22	5	35.75	2479 ⁺²³⁶ ₋₂₀₄	0.55 ^{+0.02} _{-0.02}	87.4	0.93	2302	—
20	20.62	14.74	3	46.98	2143 ⁺¹⁰² ₋₉₄	1.02 ^{+0.02} _{-0.03}	89.8	0.79	1966	—
21	21.44	15.41	1	38.59	2432 ⁺¹⁶⁵ ₋₁₅₇	0.66 ^{+0.03} _{-0.02}	89.6	0.89	2252	—
22	21.36	14.01	4	42.77	2372 ⁺¹¹⁰ ₋₉₄	1.12 ^{+0.03} _{-0.03}	87.6	0.87	2175	-1.31

Bin	x	y	Spx	S/N	W_{obs}	$(I_b/I_n)_{\text{obs}}$	i_{obs}	red. χ^2	v_s	$\log \beta$
(1)	"	"	(4)	(5)	km s ⁻¹	(7)	°	(9)	km s ⁻¹	(11)
23	21.44	14.74	1	43.37	2181 ⁺¹⁴⁹ ₋₁₂₆	0.75 ^{+0.03} _{-0.02}	89.4	0.83	2003	—
24	22.11	14.82	2	44.82	2507 ⁺¹⁶⁵ ₋₁₄₉	0.63 ^{+0.02} _{-0.02}	86.3	0.82	2331	—
25	22.76	18.73	14	42.71	2667 ⁺¹⁸⁸ ₋₁₇₃	0.68 ^{+0.02} _{-0.02}	85.8	1.40	2502	—
26	21.09	20.26	12	41.81	2676 ⁺¹⁸¹ ₋₁₆₅	0.73 ^{+0.02} _{-0.02}	81.3	1.25	2512	—
27	23.05	15.86	8	33.32	2454 ⁺²⁴³ ₋₂₁₂	0.59 ^{+0.02} _{-0.03}	86.8	1.01	2275	—
28	18.79	20.23	8	31.57	2356 ⁺¹⁹⁶ ₋₁₇₃	0.59 ^{+0.02} _{-0.02}	85.3	1.10	2175	—
29	17.54	18.78	3	46.08	2272 ⁺¹³⁴ ₋₁₃₄	0.62 ^{+0.01} _{-0.02}	88.8	0.95	2091	—
30	17.42	18.09	1	48.11	2135 ⁺¹¹⁸ ₋₁₁₀	0.78 ^{+0.03} _{-0.02}	88.4	0.82	1959	—
31	16.72	17.39	4	35.13	2528 ⁺¹⁴⁹ ₋₁₃₄	1.38 ^{+0.06} _{-0.05}	87.2	0.86	2567	-0.71
32	16.75	18.09	1	47.90	2379 ⁺¹¹⁰ ₋₁₀₂	0.95 ^{+0.03} _{-0.02}	89.4	0.80	2198	—
33	16.86	19.45	3	39.35	2108 ⁺¹⁷³ ₋₁₅₇	0.52 ^{+0.01} _{-0.02}	86.1	1.06	1933	—
34	16.75	18.76	1	51.06	2211 ⁺¹¹⁰ ₋₁₀₂	0.79 ^{+0.02} _{-0.02}	87.2	0.84	2032	—
35	22.80	14.22	3	49.91	2493 ⁺¹⁴¹ ₋₁₃₄	0.62 ^{+0.01} _{-0.02}	87.6	0.87	2316	—
36	22.11	14.07	1	37.59	2095 ⁺¹⁴¹ ₋₁₂₆	0.80 ^{+0.03} _{-0.03}	87.2	0.79	1920	—
37	22.61	13.32	5	46.21	2228 ⁺¹⁰² ₋₉₄	0.89 ^{+0.02} _{-0.02}	84.5	0.98	2050	—
38	25.73	17.29	22	42.98	2406 ⁺¹⁵⁷ ₋₁₄₁	0.66 ^{+0.02} _{-0.01}	86.5	1.49	2226	—
39	23.52	21.21	11	41.18	2624 ⁺¹⁸¹ ₋₁₆₅	0.76 ^{+0.02} _{-0.02}	80.4	1.28	2456	—
40	21.88	22.28	9	36.97	2441 ⁺¹⁶⁵ ₋₁₄₉	0.80 ^{+0.02} _{-0.03}	85.7	1.20	2262	—
41	25.39	20.75	12	45.41	2281 ⁺¹⁴¹ ₋₁₂₆	0.75 ^{+0.02} _{-0.02}	83.6	1.24	2101	—
42	19.31	22.20	9	34.71	2478 ⁺¹⁵⁷ ₋₁₄₁	0.68 ^{+0.02} _{-0.02}	83.0	1.30	2300	—
43	24.61	14.80	9	31.54	2339 ⁺²⁰⁴ ₋₁₈₈	0.53 ^{+0.01} _{-0.02}	88.4	1.00	2158	—
44	23.49	13.67	3	49.25	2289 ⁺¹²⁶ ₋₁₁₈	0.57 ^{+0.02} _{-0.01}	88.5	0.93	2109	—
45	16.63	20.46	5	38.63	2341 ⁺²¹² ₋₁₈₁	0.56 ^{+0.02} _{-0.02}	89.7	1.06	2160	—
46	17.48	22.25	8	36.44	2437 ⁺¹⁸¹ ₋₁₅₇	0.67 ^{+0.02} _{-0.02}	84.5	1.13	2258	—
47	16.03	18.09	3	36.60	2498 ⁺¹⁵⁷ ₋₁₄₁	1.36 ^{+0.05} _{-0.05}	89.3	0.86	2490	-0.76
48	16.08	18.76	1	48.57	2509 ⁺¹²⁶ ₋₁₁₈	0.96 ^{+0.03} _{-0.03}	89.5	0.80	2328	-1.90
49	16.08	19.43	1	46.59	2124 ⁺¹¹⁰ ₋₁₀₂	0.79 ^{+0.02} _{-0.03}	89.1	0.67	1949	—
50	16.08	20.10	1	33.76	2210 ⁺¹⁷³ ₋₁₆₅	0.76 ^{+0.04} _{-0.03}	87.5	0.83	2031	—
51	15.36	18.75	3	38.40	2117 ⁺¹¹⁰ ₋₁₀₂	1.22 ^{+0.04} _{-0.05}	90.0	0.93	1941	—
52	15.41	19.43	1	47.63	2313 ⁺¹²⁶ ₋₁₁₈	0.89 ^{+0.03} _{-0.02}	89.5	0.87	2133	—
53	15.41	20.10	1	39.34	2297 ⁺¹⁶⁵ ₋₁₄₉	0.75 ^{+0.03} _{-0.03}	89.0	0.63	2117	—

Bin	x	y	Spx	S/N	W_{obs} km s ⁻¹	$(I_b/I_n)_{\text{obs}}$	i_{obs} °	red. χ^2	v_s km s ⁻¹	log β
(1)	(2)	(3)	(4)	(5)	(6)	(7)	(8)	(9)	(10)	(11)
54	15.19	21.11	4	41.04	2347 ⁺¹⁷³ ₋₁₄₉	0.62 ^{+0.02} _{-0.02}	89.2	0.92	2166	—
55	20.45	24.40	6	39.26	2194 ⁺¹⁴¹ ₋₁₃₄	0.73 ^{+0.02} _{-0.03}	83.2	1.06	2016	—
56	21.87	24.37	7	44.35	2615 ⁺¹⁴⁹ ₋₁₃₄	0.81 ^{+0.02} _{-0.02}	85.6	1.16	2446	—
57	18.87	24.37	9	41.68	2522 ⁺¹⁴⁹ ₋₁₃₄	0.73 ^{+0.02} _{-0.02}	87.5	1.37	2348	—
58	25.24	22.42	8	39.97	2529 ⁺¹⁸¹ ₋₁₇₃	0.73 ^{+0.02} _{-0.02}	83.5	1.00	2355	—
59	23.15	23.69	7	43.80	2627 ⁺¹⁴⁹ ₋₁₄₁	0.86 ^{+0.03} _{-0.02}	87.7	0.97	2430	-1.57
60	15.20	22.50	8	36.31	2230 ⁺¹⁴⁹ ₋₁₄₁	0.61 ^{+0.02} _{-0.01}	88.0	1.25	2051	—
61	14.65	19.43	3	38.76	2220 ⁺¹¹⁰ ₋₁₀₂	1.20 ^{+0.04} _{-0.04}	88.6	0.91	2042	—
62	14.74	20.10	1	44.37	2225 ⁺¹¹⁸ ₋₁₁₈	0.86 ^{+0.03} _{-0.03}	88.0	0.75	2046	—
63	14.74	20.77	1	36.95	2055 ⁺¹²⁶ ₋₁₁₈	0.79 ^{+0.03} _{-0.03}	87.0	0.78	1881	—
64	16.76	24.21	9	44.92	2727 ⁺¹⁶⁵ ₋₁₄₉	0.78 ^{+0.02} _{-0.02}	86.1	1.20	2533	-1.57
65	14.07	20.10	2	35.87	2022 ⁺¹¹⁰ ₋₁₀₂	1.12 ^{+0.04} _{-0.05}	88.2	0.80	1849	—
66	14.07	20.77	1	42.29	2120 ⁺¹³⁴ ₋₁₁₈	0.81 ^{+0.03} _{-0.03}	89.0	0.84	1944	—
67	24.64	23.59	7	38.71	3284 ⁺²⁸³ ₋₂₅₁	0.87 ^{+0.02} _{-0.03}	86.8	0.92	3225	—
68	27.50	20.46	16	41.68	2348 ⁺¹⁶⁵ ₋₁₅₇	0.76 ^{+0.02} _{-0.02}	86.1	1.13	2168	—
69	21.78	25.62	9	34.81	2350 ⁺²⁴³ ₋₂₀₄	0.57 ^{+0.02} _{-0.02}	84.2	1.12	2169	—
70	20.09	26.04	11	53.82	2354 ⁺¹¹⁸ ₋₁₁₀	0.68 ^{+0.01} _{-0.02}	88.9	1.36	2173	—
71	18.43	26.20	6	46.42	2275 ⁺¹³⁴ ₋₁₁₈	0.74 ^{+0.02} _{-0.02}	89.1	1.26	2094	—
72	17.12	26.42	6	46.57	2435 ⁺¹³⁴ ₋₁₂₆	0.81 ^{+0.02} _{-0.03}	83.7	1.09	2256	—
73	14.81	24.92	9	37.19	2356 ⁺¹⁴⁹ ₋₁₄₁	0.66 ^{+0.02} _{-0.02}	87.7	1.27	2175	—
74	13.66	22.13	3	37.38	1889 ⁺¹³⁴ ₋₁₂₆	0.61 ^{+0.02} _{-0.02}	86.9	0.96	1720	—
75	13.40	20.66	2	45.33	2078 ⁺⁸⁶ ₋₈₆	1.01 ^{+0.03} _{-0.03}	89.7	0.88	1903	—
76	13.59	21.44	2	51.06	2032 ⁺¹⁰² ₋₉₄	0.74 ^{+0.03} _{-0.02}	88.2	0.84	1859	—
77	15.49	26.61	9	47.53	2462 ⁺¹²⁶ ₋₁₂₆	0.84 ^{+0.02} _{-0.02}	86.8	1.09	2284	—
78	12.91	22.88	5	39.35	2196 ⁺¹³⁴ ₋₁₂₆	0.65 ^{+0.02} _{-0.02}	87.2	1.06	2018	—
79	12.67	20.72	4	35.90	2096 ⁺¹¹⁸ ₋₁₁₈	1.23 ^{+0.05} _{-0.04}	86.8	1.07	1921	—
80	18.31	27.56	8	35.97	2583 ⁺²⁴³ ₋₂₀₄	0.63 ^{+0.02} _{-0.02}	82.7	1.14	2412	—
81	12.73	21.44	1	44.55	2502 ⁺¹³⁴ ₋₁₂₆	1.01 ^{+0.04} _{-0.03}	88.3	0.86	2301	-1.31
82	12.73	22.11	1	39.36	2099 ⁺¹³⁴ ₋₁₃₄	0.82 ^{+0.03} _{-0.04}	86.3	0.78	1924	—
83	12.38	24.51	8	40.66	2591 ⁺¹⁵⁷ ₋₁₄₉	0.74 ^{+0.03} _{-0.02}	82.6	1.13	2420	—
84	11.83	21.44	3	41.26	2369 ⁺¹¹⁸ ₋₁₁₀	1.35 ^{+0.05} _{-0.05}	89.1	0.82	2258	-0.91

Bin	x	y	Spx	S/N	W_{obs}	$(I_b/I_n)_{\text{obs}}$	i_{obs}	red. χ^2	v_s	$\log \beta$
(1)	"	"	(4)	(5)	km s ⁻¹	(7)	°	(9)	km s ⁻¹	(11)
85	12.06	22.11	1	41.05	2259 ⁺¹³⁴ ₋₁₂₆	0.90 ^{+0.04} _{-0.04}	89.1	0.74	2080	—
86	12.06	22.78	1	33.65	1931 ⁺¹⁵⁷ ₋₁₄₁	0.67 ^{+0.04} _{-0.03}	87.6	0.82	1761	—
87	16.59	27.92	10	42.13	2741 ⁺¹⁸⁸ ₋₁₆₅	0.80 ^{+0.03} _{-0.02}	89.4	0.95	2543	-1.45
88	13.41	26.38	11	39.36	2302 ⁺¹⁴¹ ₋₁₂₆	0.80 ^{+0.02} _{-0.03}	84.4	1.24	2122	—
89	11.54	23.45	2	44.96	2444 ⁺¹⁴⁹ ₋₁₃₄	0.77 ^{+0.03} _{-0.03}	89.6	0.77	2265	—
90	11.39	22.11	1	38.93	2348 ⁺¹⁴¹ ₋₁₄₁	1.01 ^{+0.04} _{-0.04}	89.7	0.88	2167	—
91	14.48	29.13	12	29.53	2895 ⁺²²⁰ ₋₂₀₄	1.08 ^{+0.05} _{-0.05}	89.0	1.11	2749	—
92	11.39	22.78	1	42.26	2302 ⁺¹⁴⁹ ₋₁₄₁	0.81 ^{+0.03} _{-0.03}	85.4	0.93	2122	—
93	10.94	24.12	2	42.12	2400 ⁺¹⁶⁵ ₋₁₄₉	0.80 ^{+0.03} _{-0.03}	86.9	0.80	2220	—
94	10.62	22.08	4	35.85	2268 ⁺¹²⁶ ₋₁₁₈	1.56 ^{+0.07} _{-0.06}	90.0	0.92	2199	-0.80
95	10.72	22.78	1	37.78	2151 ⁺¹³⁴ ₋₁₁₈	0.91 ^{+0.04} _{-0.04}	87.2	0.76	1975	—
96	10.99	25.06	6	37.39	2357 ⁺¹⁶⁵ ₋₁₄₁	0.72 ^{+0.02} _{-0.02}	87.6	1.15	2176	—
97	10.72	23.45	1	40.19	2117 ⁺¹⁴⁹ ₋₁₃₄	0.79 ^{+0.04} _{-0.03}	86.8	0.81	1941	—
98	11.35	27.51	15	34.79	3103 ⁺²⁵¹ ₋₂₂₈	1.20 ^{+0.05} _{-0.05}	82.9	1.19	2990	—
99	9.97	22.78	3	37.83	2392 ⁺¹²⁶ ₋₁₁₈	1.28 ^{+0.05} _{-0.05}	86.1	0.91	2253	-0.98
100	10.05	23.45	1	40.63	2013 ⁺¹¹⁸ ₋₁₁₈	0.94 ^{+0.03} _{-0.04}	88.6	0.80	1840	—
101	10.05	24.25	2	49.73	2402 ⁺¹³⁴ ₋₁₂₆	0.77 ^{+0.02} _{-0.03}	87.2	0.95	2222	—
102	9.38	23.45	2	35.76	2237 ⁺¹⁵⁷ ₋₁₄₉	1.16 ^{+0.05} _{-0.05}	87.9	0.94	2058	—
103	9.50	25.48	3	37.77	2438 ⁺²¹² ₋₁₈₈	0.66 ^{+0.03} _{-0.02}	87.8	0.90	2259	—
104	9.38	24.12	1	43.11	2412 ⁺¹⁴¹ ₋₁₂₆	0.86 ^{+0.03} _{-0.03}	85.6	0.70	2232	—
105	9.38	24.79	1	38.80	2191 ⁺¹⁶⁵ ₋₁₄₁	0.73 ^{+0.04} _{-0.03}	88.2	0.85	2013	—
106	8.70	24.02	3	43.51	2175 ⁺¹¹⁸ ₋₁₀₂	1.06 ^{+0.04} _{-0.04}	88.4	0.97	1998	—
107	8.81	26.13	2	33.06	2797 ⁺²⁷⁵ ₋₂₅₁	0.75 ^{+0.04} _{-0.03}	88.3	0.72	2605	-1.51
108	8.71	24.79	1	42.75	2435 ⁺¹⁴⁹ ₋₁₃₄	0.86 ^{+0.03} _{-0.04}	89.4	0.82	2256	—
109	8.71	25.46	1	35.53	2459 ⁺²¹² ₋₁₉₆	0.68 ^{+0.03} _{-0.03}	83.7	0.80	2281	—
110	9.12	27.02	9	36.01	2866 ⁺²⁷⁵ ₋₂₃₆	0.69 ^{+0.03} _{-0.02}	82.4	1.03	2683	-1.59
111	8.04	24.64	2	48.25	2480 ⁺¹³⁴ ₋₁₂₆	1.09 ^{+0.04} _{-0.03}	87.9	0.87	2294	-1.17
112	8.04	25.46	1	37.72	2413 ⁺¹⁸¹ ₋₁₇₃	0.72 ^{+0.03} _{-0.03}	86.1	0.89	2233	—
113	7.65	26.19	3	51.42	2583 ⁺¹⁵⁷ ₋₁₄₁	0.74 ^{+0.02} _{-0.02}	87.9	0.79	2412	—
114	7.26	24.74	3	36.79	2370 ⁺¹³⁴ ₋₁₁₈	1.33 ^{+0.05} _{-0.05}	86.4	0.83	2245	-0.94
115	7.37	25.46	1	40.42	2521 ⁺¹⁸⁸ ₋₁₆₅	0.87 ^{+0.04} _{-0.03}	87.5	0.77	2346	—

Bin	x "	y "	Spx	S/N	W_{obs} km s^{-1}	$(I_b/I_n)_{\text{obs}}$	i_{obs} °	red. χ^2	v_s km s^{-1}	$\log \beta$
(1)	(2)	(3)	(4)	(5)	(6)	(7)	(8)	(9)	(10)	(11)
116	6.86	26.94	4	55.60	2548 ⁺¹¹⁸ ₋₁₁₀	0.89 ^{+0.02} _{-0.02}	86.1	0.86	2375	—
117	6.55	25.46	3	39.74	2585 ⁺¹⁵⁷ ₋₁₄₁	1.21 ^{+0.05} _{-0.04}	88.5	0.84	2545	-0.83
118	6.49	26.13	2	49.78	2388 ⁺¹²⁶ ₋₁₁₀	0.85 ^{+0.03} _{-0.03}	88.7	0.75	2208	—
119	5.25	26.03	5	28.79	2973 ⁺²⁵⁹ ₋₂₂₈	1.49 ^{+0.08} _{-0.07}	89.6	0.86	2837	—
120	5.79	26.80	2	43.83	2462 ⁺¹⁵⁷ ₋₁₄₉	0.82 ^{+0.03} _{-0.03}	89.1	0.83	2284	—
121	5.64	27.51	3	39.74	2658 ⁺²³⁶ ₋₂₁₂	0.79 ^{+0.03} _{-0.04}	88.6	0.83	2492	—
122	4.32	27.29	6	41.85	2788 ⁺¹⁷³ ₋₁₅₇	0.85 ^{+0.03} _{-0.03}	88.7	0.77	2623	-1.18
123	3.69	28.42	13	39.42	3144 ⁺²⁵⁹ ₋₂₃₆	0.86 ^{+0.03} _{-0.04}	89.7	0.94	3043	—
124	23.96	12.97	4	53.26	2242 ⁺¹⁰² ₋₉₄	0.75 ^{+0.01} _{-0.02}	88.9	1.05	2062	—
125	24.79	12.85	2	44.25	2441 ⁺¹⁴¹ ₋₁₃₄	0.62 ^{+0.02} _{-0.02}	88.9	0.91	2262	—
126	25.54	12.80	5	36.31	2066 ⁺¹⁸¹ ₋₁₅₇	0.44 ^{+0.01} _{-0.02}	86.5	1.04	1891	—
127	24.55	11.98	5	45.49	2303 ⁺¹¹⁰ ₋₉₄	0.86 ^{+0.02} _{-0.02}	86.2	1.12	2123	—
128	25.46	11.76	4	43.53	2268 ⁺¹¹⁸ ₋₁₁₀	0.75 ^{+0.02} _{-0.02}	88.3	1.25	2088	—
129	26.17	11.74	4	47.47	2356 ⁺¹²⁶ ₋₁₁₈	0.57 ^{+0.01} _{-0.02}	88.8	0.89	2175	—
130	27.12	11.17	6	43.58	2191 ⁺¹³⁴ ₋₁₂₆	0.52 ^{+0.01} _{-0.02}	88.4	1.32	2013	—
131	26.58	10.62	5	42.18	2303 ⁺¹¹⁸ ₋₁₀₂	0.85 ^{+0.02} _{-0.02}	84.6	1.23	2123	—
132	28.25	10.08	10	34.23	2472 ⁺¹⁵⁷ ₋₁₅₇	0.69 ^{+0.02} _{-0.02}	85.4	1.31	2294	—
133	27.47	10.05	2	25.62	2191 ⁺¹⁵⁷ ₋₁₄₉	0.83 ^{+0.04} _{-0.03}	88.3	1.01	2013	—

BALMER-DOMINATED SHOCKS AROUND TYCHO'S SNR*

ABSTRACT

We present Fabry-Pérot interferometric observations of the narrow $H\alpha$ component in the shock front of the historical supernova remnant Tycho (SN 1572). Covering one-fourth of the remnant's shell, we quantify the narrow $H\alpha$ -line widths, velocity centroids and fluxes along the northeastern rim of the remnant. We find a strong indication of broadening of the narrow $H\alpha$ line beyond its intrinsic width of $\sim 20 \text{ km s}^{-1}$ and a presence of an intermediate component with width of order $\sim 150 \text{ km s}^{-1}$. This points toward an additional heating mechanism in the form of a cosmic-ray precursor in the former, and a broad-neutral precursor in the latter case.

4.1 INTRODUCTION

Cosmic rays (CRs) with the energies up to the 'knee' ($\sim 1 \text{ PeV}$) are widely believed to be produced in supernova remnants (SNRs). There have been numerous efforts to find observational evidence for CR production in SNRs. With the development of instruments capable of observing particles with GeV and TeV energies, the hunt for astronomical sources of CRs became a top priority. Recent Fermi-LAT results (Ackermann et al. 2013) show, for the first time, direct strong evidence of hadronic CRs to be present in SNR shocks.

Along with the observations in high-energy bands, optical observations can also shed light on CR acceleration in SNRs (Helder et al. 2009, 2010; Nikolić et al. 2013). The spectra of Balmer-dominated shocks, typically observed around SNRs that originate from Type Ia supernova ex-

*This chapter is adapted from the paper Nikolić S., et al. (2014, in preparation).

plosions, show the presence of strong two-component hydrogen lines. When a shock wave encounters partly ionized interstellar medium (ISM), the cold pre-shock hydrogen atoms overrun by the shock can either be excited by hot post-shock gas resulting in the narrow $H\alpha$ -component emission, or enter a charge exchange process with the hot post-shock plasma producing excited hot neutrals which then give rise to the broad $H\alpha$ component. The two-component $H\alpha$ -line parameters provide valuable information on the CR precursor existence in the shocks. A narrow line broadened beyond $10\text{--}20\text{ km s}^{-1}$ gives direct evidence of the non-thermal particle presence in the shock precursor (Morlino et al. 2013b). The CRs will heat the cold neutrals in the interstellar medium, resulting in broadening of the narrow $H\alpha$ -line, but also reduction of the broad $H\alpha$ -line width due to energy being removed from the protons in the post-shock region. Given both effects on the $H\alpha$ line, the broad-to-narrow line intensity ratio is expected to be lower in the presence of CRs. Additionally, the profile of the broad $H\alpha$ line is expected to deviate from a Gaussian distribution (see Raymond et al. 2010).

We have observed Tycho's SNR, which has already been well studied across all wavelength ranges (Reynolds & Ellison 1992; Stroman & Pohl 2009; Bamba et al. 2005; Katsuda et al. 2010; Lee et al. 2004; Tian & Leahy 2011; Acciari et al. 2011; Giordano et al. 2012). In 1572, the star exploded as Type Ia supernova, leaving a remnant at an estimated heliocentric distance of $2.3\pm 0.5\text{ kpc}$ (Chevalier et al. 1980). At that distance, the remnant's diameter of $8'$ corresponds to $\approx 5\text{ pc}$. However, the observations reveal that the remnant is not symmetric, due to the density gradient of the medium that modifies the evolution of the shock. The lower shock velocity inferred in the northeastern (NE) part suggests the shock interaction with a dense ambient medium, namely a molecular cloud (Reynolds & Keohane 1999; Lee et al. 2004).

Previous optical studies of Tycho's SNR have shown indications for CRs (e.g. Ghavamian et al. 2000; Raymond et al. 2010; Lee et al. 2010). However, these studies focused on the $H\alpha$ -bright, but very complex 'knot g', where multiple or distorted shock fronts can contribute to the measured line broadening. Using the Fabry-Pérot instrument $\text{GH}\alpha\text{FaS}$ (Galaxy $H\alpha$ Fabry-Perot Spectrometer) on the William Herchel Telescope (WHT), we observed a great portion of the shock front in the NE region of the remnant. The high spatial and spectral resolution together with the large field-of-view (FOV) of the instrument, allow us to measure the narrow $H\alpha$ -line width across individual parts of the shocks simultaneously, and thereby study the indicators of CR presence in a large variety of shock front conditions. In particular, the spatial resolution allows us to distinguish between line broadening originating in geometric distortions and differential kinematics and intrinsic line broadening on very small scales.

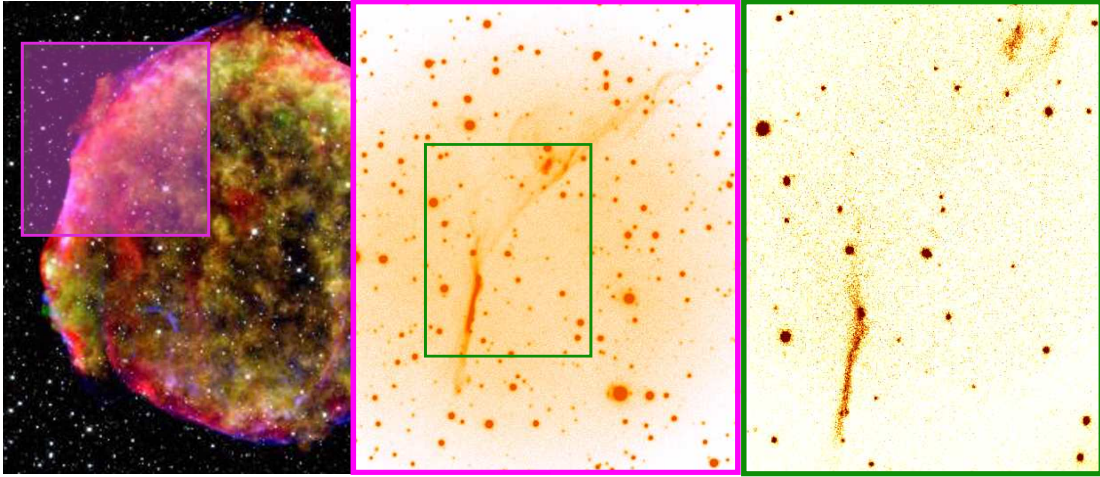


Figure 4.1: The left panel shows a composite image of the remnant ($\sim 8'$ in diameter) of Tycho Brahe's 1572 supernova, combining data from the Chandra X-ray Observatory (yellow, green, blue; NASA/CXC/SAO), Spitzer Space Telescope (red; NASA/JPL-Caltech), and the Calar Alto Observatory (white stars; Krause et al.). The transparent magenta box indicates the pointing of the ACAM (Auxiliary-port Camera) on the Cassegrain focus of the WHT with a FOV of $4' \times 4'$. The center panel shows a zoom-in on the ACAM FOV. We have covered the same region as with ACAM using the GH α FaS Fabry-Pérot interferometer with a FOV of $3'.4 \times 3'.4$. The green box marks the region which is zoomed-in in the right panel to show our reduced and integrated GH α FaS H α image.

4.2 OBSERVATIONS & DATA REDUCTION

In order to resolve the narrow H α lines along the rim of Tycho's SNR we have used the instrument GH α FaS mounted on the Nasmyth focus of the 4.2 m WHT (Hernandez et al. 2008), which operates at the Observatorio del Roque de Los Muchachos in La Palma, Canary Islands. GH α FaS is a Fabry-Pérot interferometer-spectrometer with a FOV of $3'.4 \times 3'.4$. We used a high resolution mode of the CCD, acquiring data on 1024×1024 pixels² with $R \sim 18\,000$ resolving power and a pixel scale of nearly $0''.2$. The free spectral range of the etalon was 8.2 \AA or 392 km s^{-1} centered at the H α line and split into 48 channels leading to a sampling velocity resolution of 8.2 km s^{-1} . The instrument response function is well approximated by a Gaussian with full width at half maximum (FWHM) of 19 km s^{-1} (Blasco-Herrera et al. 2010).

The observations were conducted on 15-18 November 2012, with a total exposure time of 3.5 h and the seeing FWHM $\approx 1''$. The data were reduced (see Figure 4.1) following the standard procedure for GH α FaS data described in Hernandez et al. (2008). First, we carried out wavelength and phase calibration for each observational block, followed by derotation of the channels. In the process, channels were integrated to obtain a final data cube, also called hypercube, of 48 calibrated constant-wavelength channels. The hypercube was then sky-subtracted as follows: for

each pixel, we estimated the continuum level by averaging the mean flux of the 10 bluest and 8 reddest channels, which are not affected by line emission. On pixels not covered by astronomical sources (stars and the SNR filament), the continuum map represents the sky background continuum emission. It exhibits a smooth pattern that can be well fit with a Chebyshev polynomial of order 5 (7) in x (y) direction. This allows us to interpolate over objects masked with the `SEXTRACTOR` software. To check whether the sky spectrum is constant across all channels, we extracted ≈ 15 boxes of $\approx 25^2$ pixels each across the pre-shock region, and dividing them by the local continuum level. We find that the so-normalized pre-shock spectra are all very similar and show no identifiable trend with position (see Figure 4.2). We hence adopt their average as normalized background emission across the entire field, and multiply it with the two-dimensional object-corrected continuum map to obtain a background-cube. Finally we subtract the sky-cube from the hypercube and use the result for the remainder of our analysis. Additionally, we estimated the noise cube by calculating the standard deviation within the 3×3 -pixel region (chosen because of the seeing of $1''$) around each pixel in each channel.

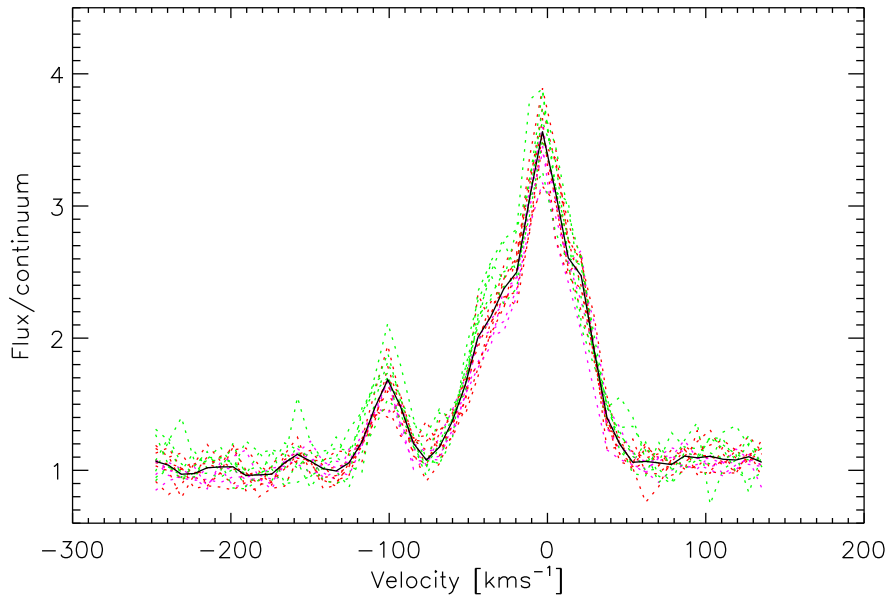


Figure 4.2: Spectral profiles from the ≈ 15 boxes from the pre-shock region used to construct the sky cube. Despite being taken from different locations all spectra are very similar, with merely the flux scale of the continuum varying (divided out here). The color indicates the distance of the boxes from the shock filament, where magenta is closest, and green farthest. The black solid curve is the averaged spectral profile over the ≈ 15 boxes.

4.3 TYCHO'S 'KNOT G'

4.3.1 PREVIOUS NARROW COMPONENT $H\alpha$ OBSERVATIONS OF 'KNOT G'

In 1992, Ghavamian et al. (Ghavamian et al. 2000) performed narrow-band $H\alpha$ imaging of 'knot g' using the Echelle spectrograph ($1''.8 \times 4'$) on the Kitt Peak National Observatory (KPNO), where they measured the width of the narrow $H\alpha$ component of $44 \pm 4 \text{ km s}^{-1}$ plus an extra component of 150 km s^{-1} arising from the small non-Gaussian contribution to the narrow component. They report on diffuse $H\alpha$ emission $1'.5$ ahead of 'knot g', but also $\text{NII}\lambda 6583$, $\text{SII}\lambda 6716$, and $\text{SII}\lambda 6731$.

In 2004, Lee et al. (Lee et al. 2007) measured the spatial variation of the line profile between the pre- and post-shock gas in the NE limb of Tycho using the Echelle spectrograph of the High Dispersion Spectrograph (HDS) on the Subaru Telescope (a $2'' \times 60''$ long-slit). The spatial scale of the instrument after binning was $0''.27$, and the velocity resolution 17 km s^{-1} . Their observations show a broadening and centroid Doppler shift $\approx 5 \text{ km s}^{-1}$ of the narrow-component post-shock $H\alpha$ line ('knot g') relative to the $H\alpha$ emission from the pre-shock gas. The narrow $H\alpha$ component and very faint NII lines in the pre-shock region reveal the existence of a photoionization precursor (PIP). The narrow component width of the 'knot g' is larger than that of the PIP $H\alpha$ line suggesting the presence of a thin precursor ($\sim 10^{16} \text{ cm}$) where gas is heated and accelerated ahead of the shock. They fitted the 'knot g' $H\alpha$ -line spectrum with three Gaussians having velocity widths of $45.3 \pm 9.0 \text{ km s}^{-1}$ for the narrow, $108 \pm 4 \text{ km s}^{-1}$ for the intermediate, $931 \pm 55 \text{ km s}^{-1}$ for broad component, and central velocities of -30.3 ± 0.2 , -25.8 ± 0.8 and $29 \pm 18 \text{ km s}^{-1}$, respectively. The width of the broad component being much lower than the expected $\sim 2000 \text{ km s}^{-1}$ is probably due to the insensitivity HDS spectroscopic configuration to the very broad line. Wagner et al. (2009) modeled the Lee et al. (2007) observations computing a series of time-dependent numerical simulations of CR modified shocks. Assuming a distance of 2.1 kpc to Tycho's SNR, they found the CR diffusion coefficient of $\kappa = 2 \times 10^{24} \text{ cm}^2 \text{ s}^{-1}$ and the injection parameter $\epsilon = 4.2 \times 10^{-3}$ to be in good agreement with the observations, suggesting that CR acceleration in the shock is not very efficient.

In 2008, Lee et al. (Lee et al. 2010) observed the NE limb of Tycho using Wide Field Planetary Camera 2 (WFPC2) on the Hubble Space Telescope (HST). The very high spatial resolution of HST revealed complex shock substructures as a consequence of different shock tangencies projected along the line-of-sight. They extracted $H\alpha$ -brightness profiles across the shock normals from four different regions along the bright filament including 'knot g'. They detected diffuse emission $1''$ ahead of the filament, and also $0''.3$ behind, which they explained with the CR shock precursor having $T \sim 80\,000\text{--}100\,000 \text{ K}$. They estimated precursor contribution of up to 30%-40% of the narrow component for a slit width of $1''$. The overall conclusion was that the acceleration

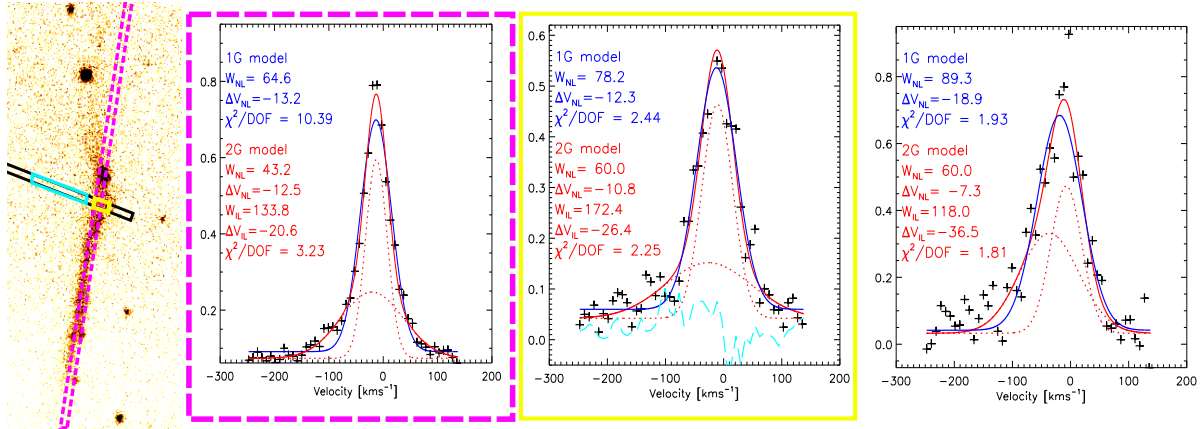


Figure 4.3: From left to right: long-slit positions of Ghavamian et al. (2000) (magenta) and Lee et al. (2007) (black) 'knot g' observations. Extracted spectra from the slits (black crosses) are shown inside the boxes with corresponding color border. For the Lee et al. slit we show the spectra extracted from the 'knot g' (yellow box) and the pre-shock region (cyan box) which spectrum was plotted inside the yellow panel as cyan dashed line. The rightmost panel shows the highest S/N spectrum of a 7×7 -pixel box inside 'knot g' to illustrate that we can now resolve the shock on smaller scales than ever before. All three panels' spectra have been fitted with two models each: one Gaussian (1G) model and two Gaussian (2G) model. The best-fit *1G model* and its parameters are shown with the blue solid line and blue legend, while the best-fit *2G model* and its parameters are shown with the red dotted lines (continuum and 2 Gaussian components), red solid line (total fit) and red legend. In the legend we show the velocity centroids ΔV , intrinsic FWHM of the components W , and the reduced χ^2 values.

of CRs is inefficient in 'knot g', suggesting that a small distance between the forward shock and contact discontinuity (Warren et al. 2005) could be due to a recent encounter of the shock with the dense ambient gas (see also Reynoso et al. 1999). More recently, Spitzer mid-infrared images of Tycho (Williams et al. 2013) revealed an overall gradient in Tycho's ambient density, with densities 3–10 times higher in the NE than in the southwest (SW) limb.

4.3.2 GHaFAS H α OBSERVATIONS OF 'KNOT G'

Here we first want to compare our GHaFaS observations of 'knot g' with the ones of Ghavamian et al. (2000) and Lee et al. (2007). As shown in the very left panel in Figure 4.3, we mimicked their long-slits centered on the 'knot g' using the coordinates and dimensions of the slits from their setups and applying a proper motion of approximately $0''.2/\text{yr}$ (Kamper & van den Bergh 1978). We have fitted the spectrum with two models, a *one-Gaussian (1G) model* and a *two-Gaussian (2G) model*. If there is only H α emission arising from the shock perturbations of the ambient hydrogen atoms, the emission should be a one-Gaussian line with the width of 10–20 km s^{-1} , and thus well represented by the *1G model*. However, presence of any kind of a

precursor or a complex shock geometry will either: a) broaden the line beyond $10\text{--}20\text{ km s}^{-1}$ (CR precursor; Morlino et al. 2013b), b) introduce a new component slightly shifted with respect to the primary $\text{H}\alpha$ component (PIP precursor) as reported by Lee et al. (2007), or c) introduce deviations from the Gaussian profile, which can be interpreted as an intermediate component with FWHM of about 150 km s^{-1} , originating from a broad-neutral precursor (Morlino et al. 2012).

Looking at the spectra (black crosses) in Figure 4.3, the *1G model* is insufficient to explain the observed line profiles, and we have therefore analyzed the data with the *2G model* as well. The second panel shows the extracted spectrum from Ghavamian's magenta slit of our GHaFaS observations. The spectrum is the average of all pixels along $36''$ length in the slit direction around 'knot g'. For Ghavamian's slit spectrum we obtain a velocity centroid position of $\Delta V = -13.2\text{ km s}^{-1}$ and an intrinsic width of $W = 64.6\text{ km s}^{-1}$ (FWHM)¹ for the *1G model*. The best-fit velocity centroid positions for the narrow and intermediate component are $\Delta V_{\text{NL}} = -12.5\text{ km s}^{-1}$ and $\Delta V_{\text{IL}} = -20.6\text{ km s}^{-1}$ with intrinsic widths of $W_{\text{NL}} = 43.2\text{ km s}^{-1}$ and $W_{\text{IL}} = 133.8\text{ km s}^{-1}$, respectively, for the *2G model*. Our *2G model* best-fit parameters are in agreement with Ghavamian's best-fit parameters $W_{\text{NL}} \approx 44\text{ km s}^{-1}$ and $W_{\text{IL}} \approx 150\text{ km s}^{-1}$.

The third panel shows the extracted spectrum from Lee's black slit around 'knot g' (yellow box) fitted by the *1G model* with $\Delta V_{\text{NL}} = -12.3\text{ km s}^{-1}$, $W_{\text{NL}} = 78.2\text{ km s}^{-1}$, and the *2G model* with $\Delta V_{\text{NL}} = -10.8\text{ km s}^{-1}$, $W_{\text{NL}} = 60.0\text{ km s}^{-1}$ and $\Delta V_{\text{IL}} = -26.4\text{ km s}^{-1}$, $W_{\text{IL}} = 172.4\text{ km s}^{-1}$. When compared to Lee's best-fit parameters, we notice that our *2G model* best-fit narrow and intermediate-component widths are broader by about 15 km s^{-1} and 60 km s^{-1} , respectively. Also, while the velocity centroids of the intermediate component are consistent, we get the narrow-component velocity centroid redshifted by $\approx 15\text{ km s}^{-1}$ with respect to the intermediate-component centroid unlike its previously reported 5 km s^{-1} blueshift (Lee et al. 2007). The cyan dashed line in the same panel shows the extracted spectrum from the cyan box in the pre-shock region (ahead of the 'knot g') by summing-up 80 pixels ($16''$) in the slit direction. Lee et al. (2007) reported on the PIP $\text{H}\alpha + \text{NII}$ emission in that region. We detect very faint line emission there as well, around the $\text{NII}\lambda 6548\text{\AA}$ line at -100 km s^{-1} and $\text{H}\alpha$ around -30 km s^{-1} . However, the total cyan flux is less than 10 % of the total flux on the shock filament (even in the smaller boxes) and we conclude that it cannot significantly affect our results. Thus, our current models do not include this component.

Unlike previous observations, we have enough spatial resolution and signal-to-noise (S/N) to extract the spectra from smaller regions than just collapse spectra from all the pixels in 'knot g'. Therefore, in the very right panel in Figure 4.3 we show the highest S/N spectrum of a 7×7 -pixel box inside the 'knot g'. We can make even smaller boxes, but we have chosen 7×7 box as a best compromise between spatial resolution and S/N. However, we do not consider boxes smaller than

¹All the widths presented in this Chapter are the intrinsic ones ,i.e., deconvolved from the instrument spectral resolution of 19 km s^{-1} .

3×3-pixel box, because of the seeing of 1'' at the time of the observations. Our best-fit parameters in said 7×7 box are: $\Delta V_{\text{NL}} = -18.9 \text{ km s}^{-1}$, $W_{\text{NL}} = 89.3 \text{ km s}^{-1}$ (*1G model*) and $\Delta V_{\text{NL}} = -7.3 \text{ km s}^{-1}$, $W_{\text{NL}} = 60.0 \text{ km s}^{-1}$, $\Delta V_{\text{IL}} = -36.5 \text{ km s}^{-1}$, $W_{\text{IL}} = 118.0 \text{ km s}^{-1}$ (*2G model*). The narrow-line width of the *2G model* is thus substantially lower; vice versa, the width is likely overestimated when the secondary (wider) line is not included. However, we find that not even *2G model* can provide a good fit to some of the 7×7 boxes. We introduce a third *3G model* which includes a third Gaussian in addition to the previous two Gaussians, in order to model flat-topped or split narrow lines, and local distortions in the narrow-line flanks where they occur.

4.4 TYCHO'S NORTHEASTERN FILAMENT

In order to map H α -line profiles and extract their line widths along the whole NE shock filament, we have refined our spatial binning into 7×7-pixel boxes covering an area of 1''.4×1''.4. Collapsing a large number of pixels may introduce projection effects which propagate into the final measurements. On the other hand, smaller binning gives us the opportunity to reduce, somewhere also possibly completely eliminate, the geometric effects that affect the fine H α -line structure. In the isolated three parts of the filament (see Figure 4.4) we have performed 7×7 box binning in each of the black, red and cyan region separately. Bin locations were chosen to maximize S/N, but are required to cover every position along the filament while avoiding box overlap. Some of the extracted spectra (black solid lines plus black crosses) are shown in Figure 4.4. We constructed three simple models which we used to analyze the spectra. The motivation of the use of the three models is encouraged by the complex line structure observed, and we will here give some further details on each of the models.

The model commonly used to explain the narrow H α profiles is a *1G model* where the line emission is interpreted with only one Gaussian. This model is a good approximation when we do not have or do not expect any precursor to be present. We have set a lower limit for the intrinsic width of the H α line to 10 km s^{-1} , which is half of the width expected for the ISM temperature of 10^4 K . Also, with this limit we wanted to secure that the model does not fit small-scale line structures in case of a noisy spectrum. We do not set an upper limit on the width, nor do we set limits on the line flux and velocity centroid. The model includes a constant to account for the continuum emission arising from the broad H α -line emission which is inaccessible here since it is much broader ($\sim 2000 \text{ km s}^{-1}$) than our spectral coverage ($\sim 400 \text{ km s}^{-1}$). This constant can vary along the filament.

The first (left) panel spectra in Figure 4.4 are fitted with the *1G model* (green solid line). In most of the cases (see also Table 4.1 in the Appendix), a *1G model* either yields much broader H α lines beyond the expected 20 km s^{-1} , or cannot explain the lines' structure (shape).

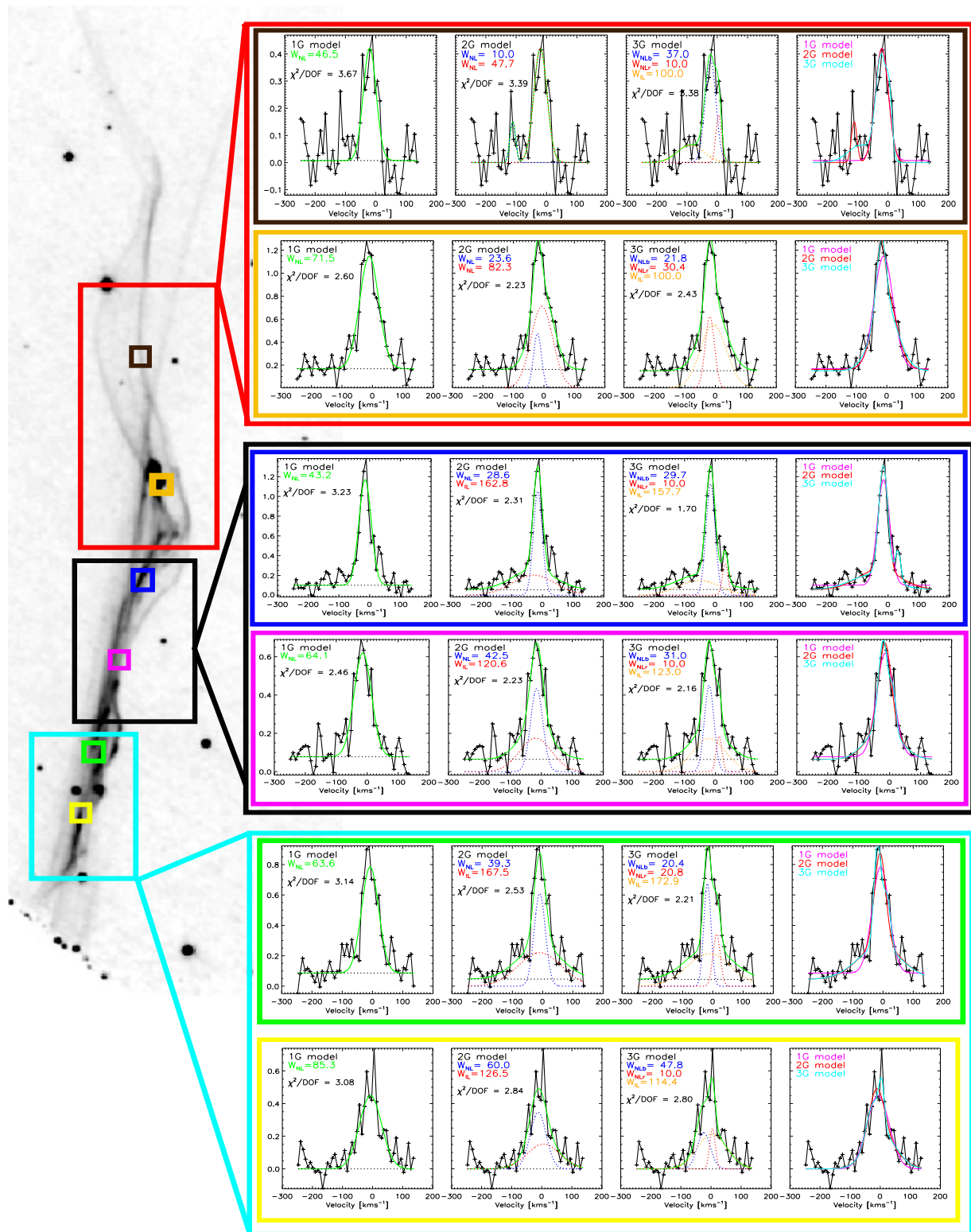


Figure 4.4: Three different regions marked with red, black and cyan squares overplotted on the HST image of Tycho's NE limb (Credit: Lee et al. 2010), including small 7×7 colored boxes inside each of them positioned where the presented spectra (black solid lines + black crosses) have been extracted from. We show six spectra in total and the best-fit parameters for the *1G model* (first panel), *2G model* (second panel), *3G model* (third panel). The comparison of the three models is shown in the fourth panel.

To account for deviations from a single Gaussian, we applied a *2G model* with the two Gaussian profiles. This time we have limited one of the component's intrinsic widths to the range 10–60 km s⁻¹, while we left the other free with the lower limit of 10 km s⁻¹. The upper boundary of 60 km s⁻¹ corresponds to the maximal line width measured in various observations of different SNRs (Hester et al. 1994; Smith et al. 1994). The intrinsic width of 150 km s⁻¹ was used as an initial guess for the width of the second component. Whenever the model gives the width of the second component larger (smaller) than 100 km s⁻¹ (an arbitrary cut²), we interpret it as an intermediate (narrow) component. The lines with widths in the range 60–100 km s⁻¹ might be both, either narrow or part of the intermediate component, and to distinguish between the two, the full posterior distribution of all line parameters must be studied, which is beyond the scope of the present thesis. Fluxes and centroid positions in this model are unrestricted for both components. As before, we fitted a constant for the continuum emission. We see that the fit sometimes yields either a narrow plus intermediate component as a best result, while sometimes the best fit contains two narrow components. Some of the double-narrow component fits show that one of them is broader than 60 km s⁻¹, e.g. the spectrum of the orange box inside the red region in Figure 4.4. On the other hand, the narrow+intermediate component fits cannot account for some of the bright peaks (e.g. blue box in the black region and green box in the cyan region), or for a double-peak profiles (e.g. yellow box in the cyan region). The second panels in all of the boxes show the *2G model* fit, where the black dotted line is the continuum fit, blue and red dotted lines are the Gaussian components fits, and the green line shows the total fit.

The *3G model* is a set of three Gaussians of which two are the narrow components with the widths limited to the range 10–60 km s⁻¹, and one is the intermediate component with the lower line width limit of 100 km s⁻¹. Where applicable, we used the best-fit parameters from the *2G model* for the intermediate component as initial parameters. Fluxes and centroids are again not restricted. The best-fit models are shown in the third panels, where blue, red and orange dotted lines show the three individual components, while, as before, black dotted line is the continuum fit and the green solid line is the total fit. The fourth panel shows the comparison of the three models. The full list of the best-fit parameters, i.e. line widths, flux ratios, velocity centroids, and the comparison between the models for all the 7×7 boxes on the filament (not only a few plotted spectra) are given in Tables 4.1, 4.2 and 4.3 in the Appendix. The uncertainties presented there are formal 1σ uncertainties of the χ²-minimum, which we found by running the IDL-based fitting procedure *mpfit*. The order of values in the tables are from the bottom part of the HST image (south) for the successive boxes toward the upper part (north). The filament becomes very faint in the northern part (red region), where, as can be seen in the black box spectrum, S/N is very low and the fit is uncertain, especially because the *2G* and *3G models* find a second/third model component in the part far from the Hα emission in the region where we would expect the NII line

²Shock velocities between 1000 and 5000 km s⁻¹ give rise to a width of the intermediate component in the range between 100 and 300 km s⁻¹ (Morlino et al. 2012).

to occur. The only solution here would be to enlarge the box size and increase the S/N. Since we focus here on the bright parts of the filament and interpretation of their spectra, we keep the 7×7 box size for all regions, but in the future will include larger boxes in regions of weaker emission. We are also cautious regarding the interpretation of fit results where a parameter hits any of our lower or upper limits. With respect to finding the global χ^2 -minimum (i.e. the maximum of the likelihood), we note that a better way to ensure locating it will be a Markov chain Monte Carlo (MCMC) approach, which would also provide more realistic parameter uncertainties.

4.5 DISCUSSION

Previous observations able to resolve narrow $H\alpha$ components in various SNRs showed $H\alpha$ -line broadenings of $30\text{--}50\text{ km s}^{-1}$ (Hester et al. 1994; Smith et al. 1994; Sollerman et al. 2003) implying pre-shock temperatures of $20\,000\text{--}60\,000\text{ K}$. We, too, unambiguously detect narrow $H\alpha$ lines with the widths much greater than 20 km s^{-1} . There are two possible interpretations of this result. One is that the CR acceleration is efficient in the NE rim of the Tycho's remnant and as a result affects the line in terms of broadening as predicted by Morlino et al. (2013b). The other is that the complex shock geometry, nicely evident in the HST image, cannot be completely ruled out as the culprit, gives a broadened narrow line as a result of spatial averaging or line blending. Moreover, in some of the boxes we find an indication of the double-peak profiles, especially when considering smaller (3×3 and 5×5) pixel boxes that can well be due to multiple shock fronts projections along the line-of-sight.

Paramount residuals in the line wings of the double narrow line model or broadened single line model justify inclusion of an intermediate component in the model. The intermediate component cannot be the result of the geometry alone, even if blending of two intermediate components could cause additional further broadening. Instead, the intermediate line clearly points towards an additional heating mechanism in the form of broad neutrals and/or CRs. The neutral fraction of the pre-shock gas ~ 0.9 was inferred by Ghavamian et al. (2001) and makes Tycho's NE rim one of the best candidates for detection of a broad-neutral precursor. Contribution of the PIP precursor in the line wings is rather small and should not significantly affect the previous conclusion, especially given that the residuals are often seen on both red and blue side of the line, contrary to the PIP occurrence only in the blue wings.

In concluding this discussion, we would like to mention that the analysis presented here is rather qualitative. In order to find the best model to explain the observed profiles, we would require proper Bayesian evidence comparison. To estimate the error bars we will have to perform Monte Carlo error or bootstrap resampling. Once we find the most likely model, we can start analyzing spectra from the smaller boxes in order to get as close as possible to the shock geometry limit. We

also plan to explore other statistical tools, like principal component analysis (PCA), a powerful tool for analyzing variability in spectra. In this way we can reduce the number of values needed to describe a spectrum to a small number of principal components, i.e. to a set of eigenvectors, which can account for the majority of the variability of the source. However, one has to be careful when applying this technique: as we have seen in preliminary tests, PCA can interpret the intermediate component, i.e., the small variations in the $H\alpha$ -line wings as noise and completely remove that part of the spectrum.

4.6 FUTURE WORK

Parallel to the study of the $\text{GH}\alpha\text{FaS}$ narrow $H\alpha$ -line profiles, we have conducted an investigation on the same part of the remnant using OSIRIS (Optical System for Imaging and low-intermediate Resolution Spectroscopy) to observe the broad $H\alpha$ -line profiles. OSIRIS is a narrow-band tunable filter imager mounted on the 10.4 m GTC (Gran Telescopio Canarias). This instrument has similar FOV ($3'.9 \times 3'.9$) and pixel scale ($0''.25$) as $\text{GH}\alpha\text{FaS}$. Independently of $\text{GH}\alpha\text{FaS}$ observations, the OSIRIS data can be used to quantify presence of precursors by studying the broad-line widths, broad-to-narrow line intensity ratios and the shape of the broad $H\alpha$ line (see Chapter 2, Section 2.3). Combination of resolved both broad and narrow $H\alpha$ -line profiles gives a better handle on the overall conditions in the shock. OSIRIS data have been recently reduced and the preliminary results are shown in Figure 4.5.

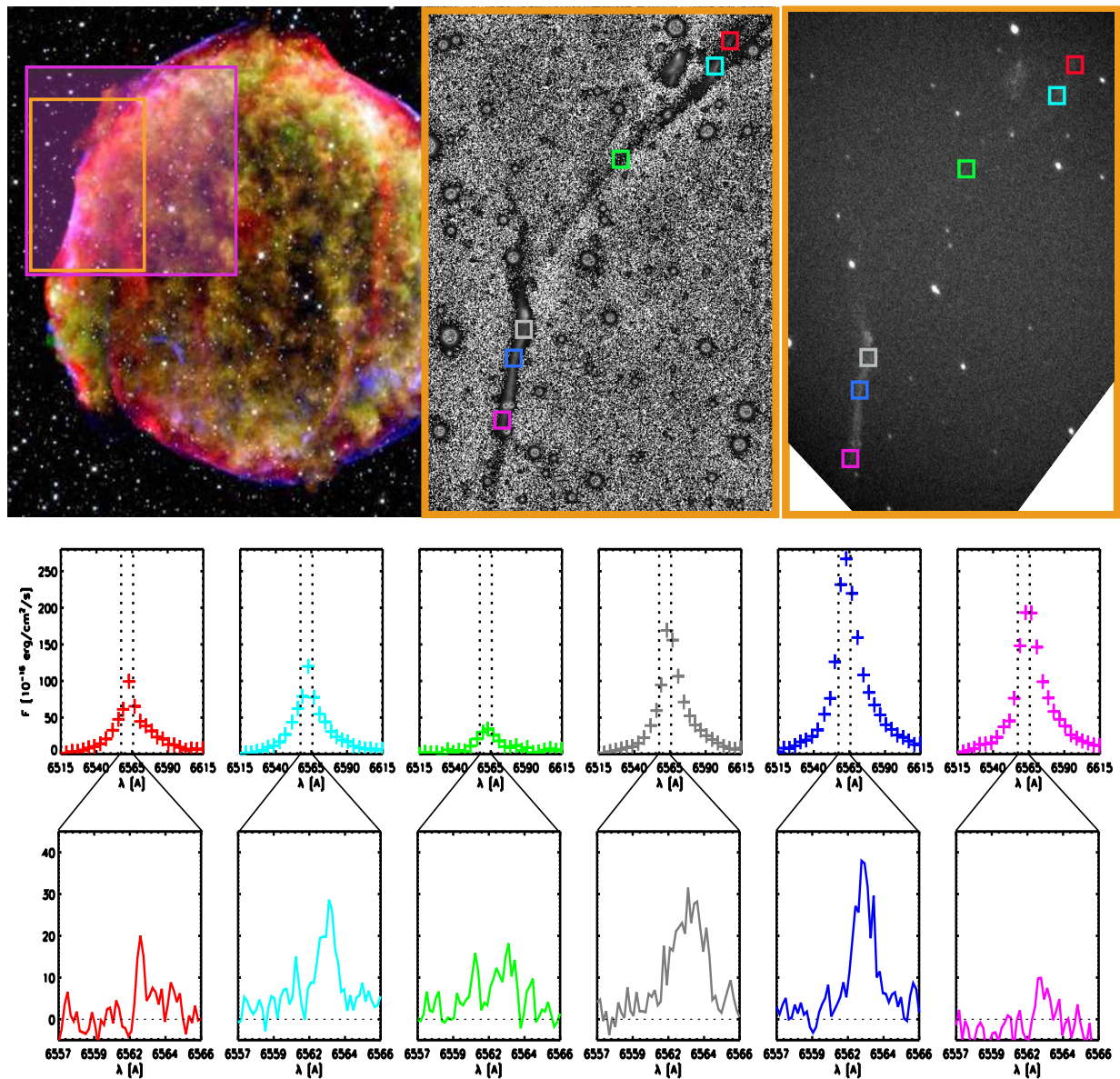


Figure 4.5: The *top-left* panel shows the composite image of the remnant ($\sim 8'$ in diameter) of Tycho Brahe's 1572 supernova, combining data from the Chandra X-ray Observatory (yellow, green, blue), Spitzer Space Telescope (red), and the Calar Alto Observatory (white stars). The transparent magenta box indicates the pointing with the OSIRIS and GH α FaS instruments. The image from the orange box magnified in the *top-middle* and the *top-right* panel shows our reduced OSIRIS and GH α FaS data, respectively. Small boxes (5 \times 5 pixels) with the different colours indicate six different positions along the nicely recovered shock front from which the H α line was extracted and shown in the panels below in the corresponding color. The *middle row* shows H α spectra extracted from the OSIRIS observations, where dashed vertical lines indicate the wavelength range covered with GH α FaS observations shown in the panels in the *bottom row*.

4.7 SUMMARY

We presented the on-going research on the Balmer-dominated shocks in the northeastern rim of Tycho's SNR. For the first time the observations covered not only the very bright and complex 'knot g', but the whole northeastern remnant's shock filament. With this larger spatial coverage of few $\sim 1'$, but at the same time small spatial scale $0''.2$ and high spectral resolution of 19 km s^{-1} , we are able to trace the narrow line behaviour all along the filament. Even though the results were presented in a more qualitative manner, we can draw very important conclusions: the observed narrow $H\alpha$ line cannot be explained by a single Gaussian line, and even if in some cases it might be possible, the line widths are broadened beyond the normal $10\text{--}20 \text{ km s}^{-1}$ gas dispersion. Next, we often find residuals in the terms of wings which can be fitted by adding an intermediate component of about $\sim 150 \text{ km s}^{-1}$. These two findings together point towards an additional heating mechanism in the form of broad-neutral and/or CR precursor. Finally, we find indications of double-peak narrow components in some of the spectra which is most probably the result of a complex shock geometry. While two blended narrow components might account for a broadening of a single narrow line, the intermediate component cannot be the result of geometry alone. With the further analysis and model developments, we aim to quantify the line behaviour in this part of Tycho's remnant.

4.8 APPENDIX

Table 4.1: Comparison of the widths and fluxes (fraction of total model flux) of the primary narrow components, fitted with the *1G model* (m1), *2G model* (m2) and the *3G model* (m3). Primary (NLa) is the narrow line with the stronger peak flux than the secondary line (where applicable). The uncertainties are the outputs of the IDL-based fitting procedure *mpfit* (which become zero in case of hitting a boundary constraint).

Box	$W_{\text{NLa,m1}}$ [km s ⁻¹]	$W_{\text{NLa,m2}}$ [km s ⁻¹]	$W_{\text{NLa,m3}}$ [km s ⁻¹]	$F_{\text{NLa,m2}}$	$F_{\text{NLa,m3}}$
1	49.4+/- 4.0	10.0+/- 0.0	46.2+/- 4.8	0.0	0.9
2	65.0+/- 4.0	69.6+/- 5.7	10.0+/- 0.0	0.9	0.3
3	85.3+/- 4.3	60.0+/- 0.0	10.0+/- 0.0	0.5	0.1
4	62.3+/- 4.1	43.9+/- 5.8	26.2+/- 4.9	0.4	0.3
5	68.7+/- 3.4	58.2+/- 5.2	58.2+/- 5.2	0.6	0.6
6	87.7+/- 5.5	30.2+/- 6.0	10.0+/- 0.0	0.3	0.1
7	61.8+/- 3.5	10.0+/- 0.0	10.0+/- 0.0	0.3	0.3
8	63.6+/- 3.5	39.3+/- 5.3	20.4+/- 6.1	0.4	0.3
9	62.2+/- 3.7	35.4+/- 6.6	25.2+/-10.2	0.4	0.3
10	58.2+/- 3.9	59.1+/- 5.0	43.9+/- 7.6	0.9	0.7
11	64.1+/- 4.4	42.5+/- 9.7	31.0+/- 9.3	0.5	0.4
12	78.8+/- 5.4	80.9+/- 6.4	100.0+/- 0.0	1.0	0.8
13	72.6+/- 4.5	21.6+/- 5.8	30.5+/- 6.3	0.3	0.5
14	58.6+/- 3.2	48.8+/-20.9	25.6+/- 9.6	0.1	0.4
15	54.2+/- 3.1	72.5+/-11.2	58.0+/-11.5	0.7	0.7
16	49.0+/- 2.9	10.0+/- 0.0	30.9+/- 3.8	0.3	0.6
17	43.2+/- 2.2	28.6+/- 2.5	29.7+/- 2.4	0.5	0.6
18	60.8+/- 3.1	48.3+/- 5.5	53.3+/- 9.1	0.6	0.6
19	64.4+/- 4.2	34.3+/-11.7	54.1+/- 8.3	0.4	0.3
20	78.4+/- 4.5	70.5+/-13.1	100.0+/- 0.0	1.0	0.7
21	100.6+/- 5.7	10.0+/- 0.0	107.4+/- 8.6	0.0	0.9
22	65.5+/- 2.7	77.8+/- 6.8	45.8+/-10.1	0.8	0.4

Box	$W_{\text{NLa},m1}$ [km s ⁻¹]	$W_{\text{NLa},m2}$ [km s ⁻¹]	$W_{\text{NLa},m3}$ [km s ⁻¹]	$F_{\text{NLa},m2}$	$F_{\text{NLa},m3}$
23	71.5+/- 3.1	82.3+/- 6.2	30.4+/- 5.5	0.8	0.3
24	52.9+/- 2.7	33.9+/- 3.7	32.4+/- 4.1	0.5	0.5
25	94.8+/- 6.9	54.9+/- 8.8	34.5+/- 7.7	0.5	0.3
26	51.1+/- 4.4	10.0+/- 0.0	10.0+/- 0.0	0.4	0.5
27	17.8+/- 2.6	17.7+/-10.1	19.3+/- 2.8	0.1	0.5
28	113.0+/-14.4	10.0+/- 0.0	10.0+/- 0.0	0.1	0.2
29	38.6+/- 4.7	31.7+/-11.9	24.6+/-16.6	0.7	0.5
30	35.4+/- 5.7	35.4+/- 5.7	26.4+/- 5.6	1.0	0.8
31	35.4+/- 5.8	10.0+/- 0.0	30.2+/- 6.4	0.4	0.5
32	64.3+/- 6.0	10.0+/- 0.0	11.2+/- 4.4	0.3	0.4
33	56.0+/- 8.3	10.0+/- 0.0	18.8+/- 0.0	0.4	0.0
34	84.0+/- 9.3	10.0+/- 0.0	17.4+/- 5.7	0.3	0.3
35	29.7+/- 5.4	16.7+/- 4.8	10.0+/- 0.0	0.4	0.4
36	33.5+/- 5.8	13.1+/- 5.9	12.9+/- 5.1	0.5	0.4
37	46.5+/- 5.3	10.0+/- 0.0	37.0+/-11.6	0.1	0.6
38	51.8+/- 5.7	10.0+/- 0.0	17.6+/- 0.0	0.5	0.0
39	36.5+/- 7.0	36.1+/- 7.1	18.1+/-13.2	0.8	0.4
40	20.2+/- 3.8	17.4+/-16.8	10.0+/- 0.0	0.3	0.2

Table 4.2: Comparison of the widths and fluxes (fraction of total model flux) of the intermediate components (IL), fitted with the *2G model* (m2) and the *3G model* (m3). The uncertainties are the outputs of the IDL-based fitting procedure *mpfit* (which become zero in case of hitting a boundary constraint). Empty boxes indicate that the model does not find the intermediate component.

Box	$W_{\text{IL},m2}$ [km s ⁻¹]	$W_{\text{IL},m3}$ [km s ⁻¹]	$F_{\text{IL},m2}$	$F_{\text{IL},m3}$
1	-	149.0+/-180.7	-	0.1
2	-	100.0+/- 0.0	-	0.4
3	126.5+/- 21.4	114.4+/- 13.4	0.5	0.6
4	230.1+/- 58.3	207.6+/- 42.2	0.6	0.6
5	239.7+/-112.7	239.7+/-112.7	0.4	0.4
6	149.0+/- 20.6	149.7+/- 19.7	0.7	0.7
7	99.9+/- 8.4	100.0+/- 0.0	0.7	0.7
8	167.5+/- 28.4	172.9+/- 28.9	0.6	0.6
9	122.5+/- 22.2	126.8+/- 21.0	0.6	0.6
10	-	121.4+/- 90.8	-	0.2
11	120.6+/- 36.7	123.0+/- 31.8	0.5	0.5
12	-	100.0+/- 0.0	-	0.8
13	106.9+/- 13.7	100.0+/- 0.0	0.7	0.3
14	-	100.0+/- 0.0	-	0.4
15	-	123.8+/-146.4	-	0.2
16	-	100.0+/- 0.0	-	0.3
17	162.8+/- 29.4	157.7+/- 37.0	0.5	0.3
18	137.8+/- 37.2	143.0+/- 50.5	0.4	0.3
19	-	396.0+/-101.2	-	0.6
20	-	100.0+/- 0.0	-	0.7
21	104.7+/- 7.0	107.4+/- 8.6	1.0	0.9
22	-	100.0+/- 0.0	-	0.5
23	-	100.0+/- 0.0	-	0.7
24	158.1+/- 27.3	169.6+/- 35.3	0.5	0.5
25	156.4+/- 33.8	143.0+/- 24.8	0.5	0.6

Box	$W_{IL,m2}$ [km s ⁻¹]	$W_{IL,m3}$ [km s ⁻¹]	$F_{IL,m2}$	$F_{IL,m3}$
26	-	100.0+/- 0.0	-	0.3
27	-	205.8+/-113.1	-	0.3
28	119.1+/- 17.3	146.7+/- 24.4	0.9	0.6
29	-	100.0+/- 0.0	-	0.2
30	136.1+/- 0.0	136.1+/- 0.0	-	0.0
31	-	317.3+/-756.4	-	0.5
32	-	100.0+/- 0.0	-	0.5
33	-	100.0+/- 0.0	-	0.7
34	115.7+/- 20.3	141.1+/- 43.4	0.7	0.6
35	246.2+/- 83.9	304.1+/-165.4	0.6	0.5
36	-	100.0+/- 0.0	-	0.5
37	-	100.0+/- 0.0	-	0.3
38	-	100.0+/- 0.0	-	0.6
39	-	100.0+/- 0.0	-	0.3
40	-	100.0+/- 0.0	-	0.7

Table 4.3: Comparison of the widths and flux fractions of the secondary narrow-line components, fitted with the *2G model* (m2) and the *3G model* (m3). Primary is the narrow line with the stronger peak flux than the secondary line (NLb). The flux fraction here is the ratio between secondary and primary narrow lines. The uncertainties are the outputs of the IDL-based fitting procedure *mpfit* (which become zero in case of hitting a boundary constraint). ΔV_{NLb} is the velocity centroid offset relative to the primary narrow line. Empty boxes indicate that the model does not find the secondary narrow component.

Box	$W_{\text{NLb,m2}}$ [km s ⁻¹]	$W_{\text{NLb,m3}}$ [km s ⁻¹]	$\Delta V_{\text{NLb,m2}}$ [km s ⁻¹]	$\Delta V_{\text{NLb,m3}}$ [km s ⁻¹]	$F_{\text{NLb,m2}}$	$F_{\text{NLb,m3}}$
1	-	10.0+/- 0.0	-	-51.0	-	0.1
2	10.0+/- 0.0	33.5+/-11.6	-12.8	34.4	0.2	1.1
3	-	47.8+/-23.0	-	-28.7	-	2.1
4	-	10.0+/- 0.0	-	-36.5	-	0.3
5	-	-	-	-	-	-
6	-	21.5+/-17.4	-	-20.2	-	1.3
7	99.9+/- 8.4	-	-8.2	-	2.9	-
8	-	20.8+/-11.3	-	30.3	-	0.5
9	-	10.0+/- 0.0	-	24.0	-	0.5
10	10.0+/- 0.0	15.4+/- 6.5	-14.4	43.1	0.1	0.2
11	-	10.0+/- 0.0	-	32.1	-	0.2
12	-	10.0+/- 0.0	-	-30.9	-	0.8
13	-	49.2+/-22.1	-	49.6	-	0.4
14	51.8+/- 4.1	23.4+/-12.2	-70.2	29.5	6.8	0.8
15	22.9+/- 9.1	10.0+/- 0.0	0.7	-8.9	0.4	0.2
16	66.5+/- 6.1	10.0+/- 0.0	-0.6	-44.6	2.9	0.1
17	-	10.0+/- 0.0	-	47.5	-	0.2
18	-	10.0+/- 0.0	-	9.2	-	0.1
19	35.4+/- 7.0	10.0+/- 0.0	41.9	34.1	1.9	0.2
20	-	19.6+/- 9.1	-	35.5	-	1.3
21	-	10.0+/- 0.0	-	-34.2	-	0.4
22	24.4+/- 8.9	10.0+/- 0.0	8.6	16.2	0.2	0.3

Box	$W_{\text{NLb},m2}$ [km s ⁻¹]	$W_{\text{NLb},m3}$ [km s ⁻¹]	$\Delta V_{\text{NLb},m2}$ [km s ⁻¹]	$\Delta V_{\text{NLb},m3}$ [km s ⁻¹]	$F_{\text{NLb},m2}$	$F_{\text{NLb},m3}$
23	23.6+/- 7.7	-	-14.5	-	0.2	-
24	-	10.0+/- 0.0	-	-37.8	-	0.1
25	-	10.0+/- 0.0	-	39.3	-	0.3
26	78.2+/-11.8	10.0+/- 0.0	3.8	-31.2	1.7	0.4
27	18.3+/- 2.6	26.4+/-10.0	-57.6	55.6	5.8	0.3
28	-	18.7+/-10.3	-	-38.9	-	0.9
29	10.0+/- 0.0	10.0+/- 0.0	21.3	21.2	0.4	0.5
30	-	10.0+/- 0.0	-	-39.1	-	0.2
31	35.2+/-17.0	10.0+/- 0.0	-22.2	-44.5	1.8	0.1
32	85.8+/-12.3	10.0+/- 0.0	-0.5	-40.6	2.6	0.3
33	60.1+/-18.1	-	-31.1	-	1.7	-
34	-	10.0+/- 0.0	-	59.0	-	0.2
35	-	14.9+/-15.0	-	-26.4	-	0.4
36	66.5+/-33.0	10.0+/- 0.0	-43.7	54.8	0.9	0.3
37	47.7+/- 5.0	10.0+/- 0.0	91.3	26.7	6.6	0.2
38	49.7+/-15.4	-	-31.6	-	1.1	-
39	39.2+/-25.4	10.0+/- 0.0	-74.8	24.9	0.2	0.6
40	87.4+/-31.0	10.0+/- 0.0	-3.4	15.9	2.6	0.7

BALMER-DOMINATED SHOCKS AROUND CLASSICAL NOVA FH SER

ABSTRACT

This chapter presents the study of a classical nova FH Ser using the VIMOS-IFU instrument on the VLT. We present spectroscopic observations of one of the deepest optical measurements of a nova, particularly of the nova FH Ser. We focus here on a central object emission which was successfully separated from the nova shell emission discussed briefly in this chapter as well. The main goal of this on-going research is to construct detailed spatial kinematic model of the nova remnant, and model density and velocity profiles of the central object emission, which contain the information of the nova outburst mechanism and its progenitors. We will first introduce some basic observational aspects of nova light curves and spectra, and present our preliminary results afterwards.

5.1 INTRODUCTION

As have been discussed in the Chapter 1, the fundamental energy source of a nova outburst, i.e., of luminosity increase and mass ejection, is thermonuclear runaway of an accreted envelope onto a white dwarf (WD) in a close binary system (CBS). There are three possible processes to eject the envelope: **shock ejection** initiated in a rapid release of energy in the envelope; **pressure ejection** formed in a gradual release of energy in the envelope (Sparks 1969); and **radiation pressure ejection** through stellar wind (Bath & Shaviv 1976); or any combination of those three. Classical novae eject material of about $10^{-5}M_{\odot}$ – $10^{-4}M_{\odot}$ in mass and with velocities of $\sim 10^3$ km s⁻¹, releasing a kinetic energy of 10^{43} to 10^{45} erg. The observed rate of classical novae in our Galaxy

is 35 ± 11 per year¹ (Darnley et al. 2006). This implies that classical novae bring into the ISM about $7 \times 10^{-3} M_{\odot} \text{yr}^{-1}$ (lower limit) of C, N, O and their isotopes, and thus contribute to chemical evolution of the Galaxy. It is widely believed that all novae are recurrent, but the successive time between two eruptions (order of $\geq 10^3$ yr) is much larger than our observational baseline.

5.1.1 LIGHT CURVES AND SPEED CLASSES

Unlike SNe Ia, novae do not form a homogeneous class. Moreover, each nova has its own distinct features, i.e., its fingerprints. Thus, for example, even though the form of optical light curves (see Figure 5.1) of all novae are similar, decline rate after the optical maximum defines the different

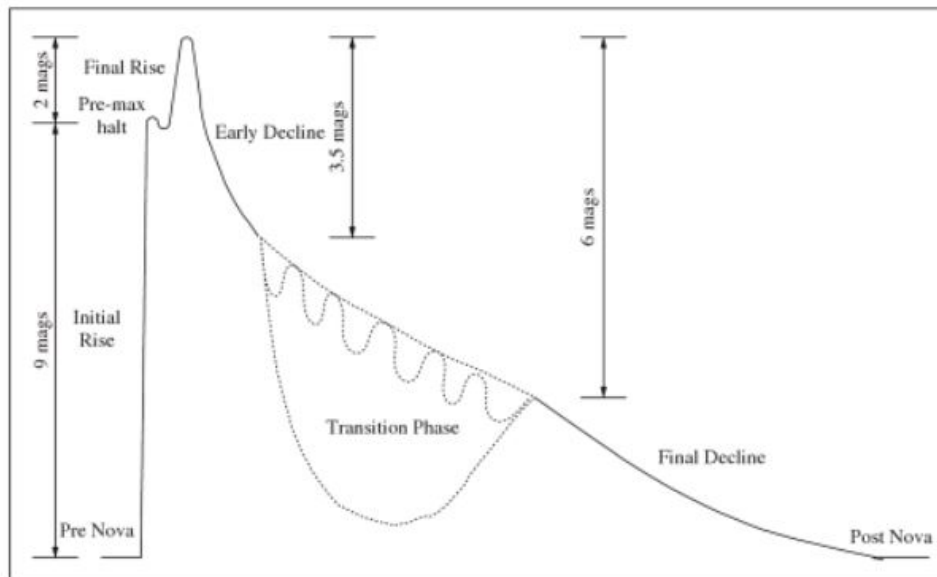


Figure 5.1: Nova optical light curve (credit: Bode & Evans 2008). Deep minimum in the transition phase is characteristic for novae that show presence of dust in the ejecta.

speed classes of novae. Payne-Gaposchkin (1957) introduced five different speed classes according to optical light curve decay time by 2 magnitudes (t_2) or 3 magnitudes (t_3): **very fast** with t_2 (t_3) of <10 (<20) days, **fast** 11–25 (21–49) days, **moderately fast** 26–80 (50–140) days, **slow** 81–150 (141–264) days, and **very slow** 151–250 (265–440) days. Downes et al. (2001) showed that there is a simple empirical relationship between t_2 and t_3 ; $t_3 = 2.10t_2$ for very fast and fast novae, and $t_3 = 1.75t_2$ for moderately fast, slow and very slow novae. Physics behind different speed classes lies in the initial energy generation rate, i.e., depends on the envelope ejection scenario mentioned above. First two scenarios (shock ejection and pressure ejection) are more connected to faster novae while radiation pressure ejection is more connected to slower classes of novae.

¹Subjective to selection effects.

Furthermore, there is a correlation between maximal magnitude and rate of decline (MMRD relationship). The fact that brighter novae fade faster, was first noticed for novae in M31 by Hubble (1929).

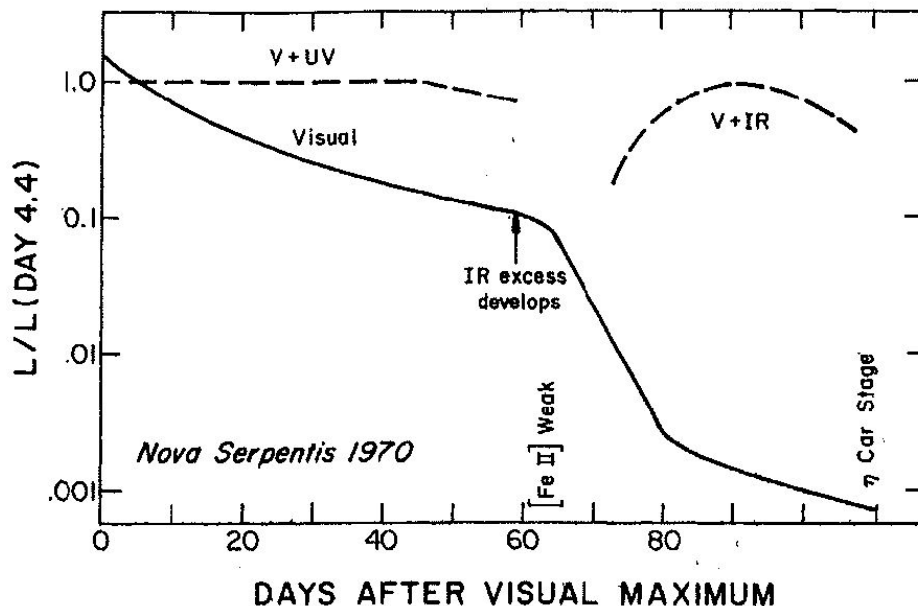


Figure 5.2: FH Ser light curve based on optical and UV observations (Gallagher & Code 1974), and Geisel et al. (1970) IR measurements.

McLaughlin (1945) confirmed the same correlation for Galactic novae. A modern MMRD relationship (without slow nova classes) is defined by Della Valle & Livio (1995) and has a non-linear trend. Downes & Duerbeck (2000) showed that MMRD relationship which includes also slow novae into consideration has more linear trend, and is defined as

$$M = b_n \log t_n + a_n$$

where M is V, B or pg^2 absolute magnitude, and n is either 2 or 3. They estimated uncertainty of ≈ 0.5 mag in M_V most probably arising from the spread in WD luminosities before eruption. Even though optical curves are very different among different speed classes, bolometric luminosities seem to be quite similar for moderate and slow novae (Gallagher & Starrfield 1976). It has been observed that a decrease in optical luminosity by a factor 10 is first followed by an increase in UV luminosity during first 60 days, implying existence of high-temperature remnant. Novae that show presence of dust in the ejecta have IR luminosities that dominate even in the next 40 days. This gives the bolometric luminosity nearly constant during the first 60 (100) days after the optical maximum (see Figure 5.2). This was first noticed in the case of the classical nova FH Ser (Gallagher & Code 1974; Hyland & Neugebauer 1970; Geisel et al. 1970).

²photographic

5.1.2 NOVA OUTBURST SPECTRUM

A nova spectrum goes through 5 phases, which correspond to the different stages in the evolution of a nova. The **pre-maximum phase**, the phase before rise to the optical maximum, is dominated by broad, blue-shifted absorption lines, where slower novae show smaller shifts and lower luminosity. The measured line widths give the expansion velocities, which go from -1300 km s^{-1} (very fast) to -100 km s^{-1} (very slow novae). This phase is dominated by the spectrum of an expanding, optically thick photosphere. At **visual maximum** absorption lines become stronger and more blue-shifted showing mostly C, N and O lines. [McLaughin \(1960\)](#) found a relationship between the velocity of the ejecta and the nova speed class:

$$\log V_{ej} = 3.70 - 0.5 \log t_3 = 3.57 - 0.5 \log t_2,$$

where t_2 (t_3) are given in days and V_{ej} in km s^{-1} . Right after the maximum, the absorption lines start developing P-Cygni profiles and the spectrum is being dominated by HI, CaII, NaI and FeII. Few days after OI, NII and OIII emission lines form. Accompanying UV spectrum show strong emission lines of He, C, N, O, Mg, Al and Si. After 1 to 20 days (speed class dependance) after the maximum, P-Cygni broad absorption lines start to dominate the spectrum again, but now almost twice broader and more blue-shifted than at the maximum spectrum. This **diffuse enhanced phase** lasts few weeks in case of very fast novae and few months in case of very slow ones. The velocity is described by [McLaughin \(1960\)](#) as

$$\log V_{ej} = 3.81 - 0.41 \log t_3 = 3.71 - 0.4 \log t_2.$$

Once the magnitude drops by 1–2 mag, HeI, CII, NII, OII and later NIII and NV optical absorption lines appear and form so-called **Orion spectrum**. This phase indicates that the originally expanding photosphere breaks up or collapses, and we start detecting radiation from the hot central region. Orion spectrum evolves to nebular spectrum after a drop of 2–4 mag from the visual maximum. **Nebular spectrum** is dominated by emission OI, NII, OIII and NeIII lines, showing also highly ionized heavier elements in the spectrum for very high $T \approx 10^6 \text{ K}$. After few years-decades when the ejecta can be resolved, we have **post-nova spectrum** exhibiting strong Balmer continuum and permitted recombination lines of H, He, C, N and O.

Modern classification separates novae into three groups according to their postoutburst spectra: He/N novae (showing HeI/HeII or NII/NIII lines), FeII novae (showing FeII lines) and hybrid novae which show characteristics of both (see [Williams \(2012\)](#) for a review). The characteristics of He/N novae are very broad lines, as a results of high expansion velocities, having rectangular profiles, higher ionization, small number of absorption features and relatively rapid decrease of a visible luminosity, and are, thus, connected to very fast and fast novae. These features point

towards their origin in episodic ejection from the WD. FeII novae have narrower, more rounded profiles which often show P-Cygni profiles dominated by low level ionization of heavy element, and show slower luminosity decline, and are, thus, related to slower novae. Contrary to He/N novae, spectroscopic features of FeII novae indicate that they most probably originate from the companion star in the CBS rather than from the WD itself. As a result of predominate physical conditions, the spectrum of hybrid novae evolves from FeII to He/N class, or vice versa. It is characteristic for moderately fast novae with the higher ejection velocities than in FeII class. Most of the observed novae (85 %) are of FeII class, 15 % are of He/N, while only 5 % belong to hybrid novae.

5.2 VIMOS-IFU OBSERVATIONS OF FH SER

FH Ser (Nova Serpentis 1970), discovered by Honda (1970), is located about 0.95 kpc away and has an expansion velocity of about 490 km s^{-1} . It is one of rare novae with a multiwavelength coverage. It is classified as a slow nova of the FeII class (Williams 1992). Looking through the optical wavelength window, FH Ser has a resolved $H\alpha$ elliptical shell surrounded by a well-defined NII equatorial ring (see Figure 5.3). According to Hubble Space Telescope (HST) images and WHT long-slit spectroscopic observations, the expanding nebula has been modeled as a prolate ellipsoid, with its major axis forming an angle of 60° with the line-of-sight (Gill & O'Brien 2000). The measured shell axes are $7''.0 \pm 0''.3$ (major axis) and $5''.8 \pm 0''.1$ (minor axis), where the true axial ratio after de-projection of the ellipsoid is 1.26 ± 0.08 . The observations also revealed the presence of a NII-enhanced equatorial ring with its brightness 40 times greater than in the $H\alpha$ -dominated shell. The nature of this NII-enhanced ring is still unknown. Gill & O'Brien (2000) suggested that the larger irradiation at the higher latitudes of the accretion disc might result in very highly ionized nitrogen, suppressing NII emission in those regions, and leaving a very bright NII equatorial ring behind. It is very unlikely that a density increase would be able to explain the ring since one would expect also enhancement of $H\alpha$ emission. Also, WD rotation prior the eruption might cause variation in surface metallicity, but it is hard to imagine that it would produce a thin localized NII ring instead of spreading NII all over its surface.

The high spatial and spectral resolution of the VIMOS-IFU spectrograph on the VLT is well suited for studying novae, more specifically the structure of the surrounding nebula and the geometry of the explosion, with a much higher precision than before. Observations were carried during the nights of 2011 April 9 and May 10, 27, 28, 30, 31, using the VIMOS-IFU placed at coordinates $\alpha_{J2000} = 18^h 31^m 31^s .6$, $\delta_{J2000} = 02^\circ 36' 49'' .5$. The overall exposure time of 8 hours on-source accumulated in 15 exposures, all taken with seeing $\lesssim 0''.9$, enables us to collect enough photons to reach good signal-to-noise ratios (S/N). A dither pattern with small offsets between the individual

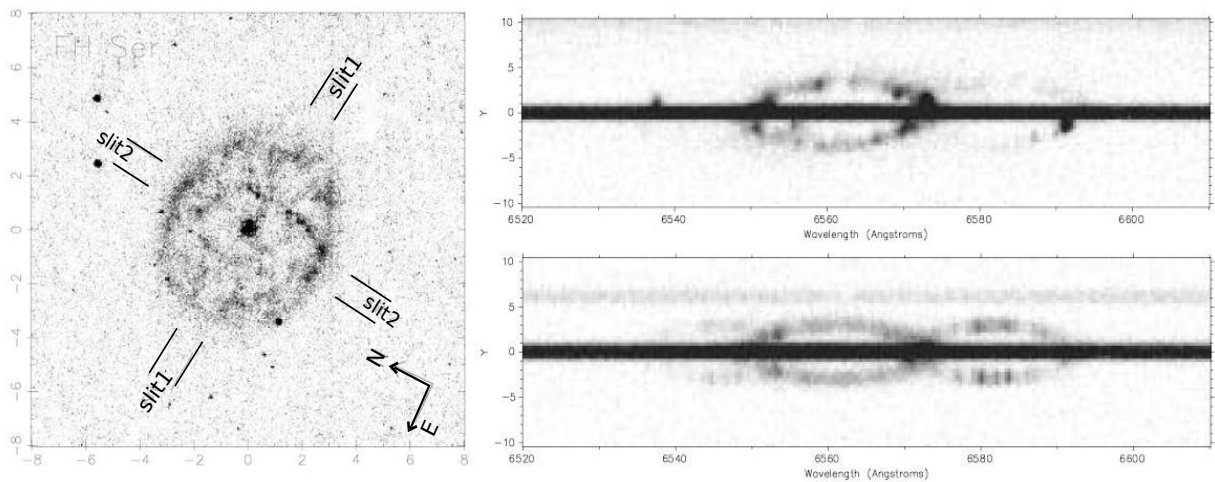


Figure 5.3: Left: HST/WFPC2/F656N image of the remnant around FH Ser, with (1''-wide) slit positions indicated. Right: WHT/ISIS Long-slit spectra for the shell of FH Ser in slit positions 1 (top) and 2 (bottom). For slit 1, west is to the top of the frame; for slit 2, north is to the top; Y labels the spatial direction (in arcsec). Both slits show velocity ellipses of the shell in the H α ($\lambda 6562.8 \text{ \AA}$) and weaker NII ($\lambda 6549, 6584 \text{ \AA}$) emission lines. Credit: Gill & O'Brien (2000).

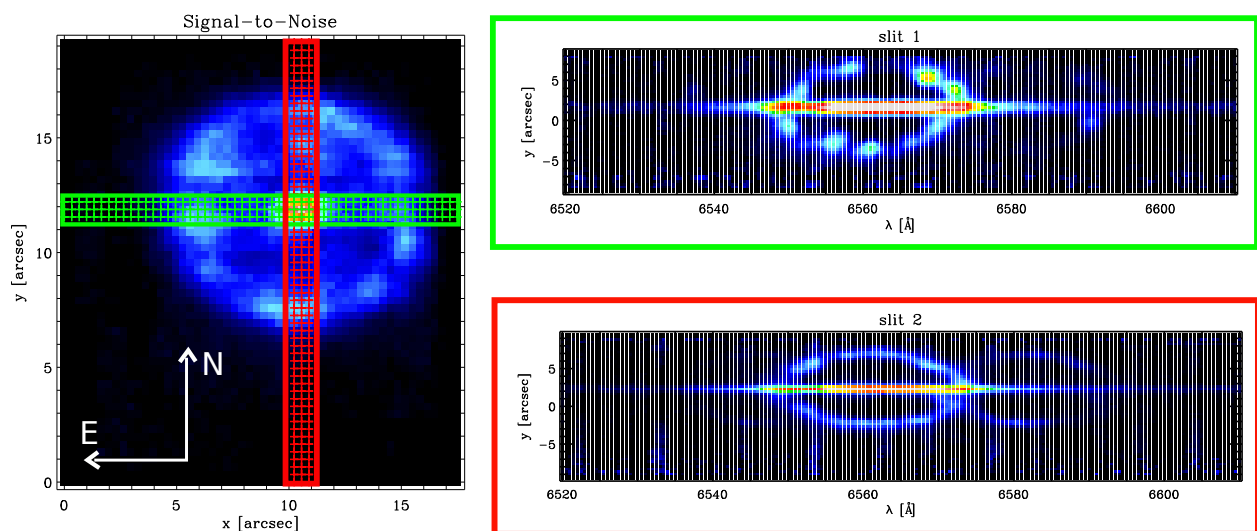


Figure 5.4: Left: VIMOS-IFU field-of-view of $13'' \times 13''$ covering the classical nova FH Ser. The plot shows signal-to-noise map overlaid by two slits: green referring to the WHT/ISIS slit1 and red to the WHT/ISIS slit2. Right: 1D spectra extracted from the green and red slits on the left showing velocity ellipses bright in H α and NII. Y-axis is in arcseconds where the zero point refers to the central object position.

exposures was applied in order to account for dead fibers. We used a spatial scale of $0''.33$ per pixel ($\approx 10^{-3}$ pc at the distance of 0.95 kpc) in combination with the HR-Orange grism providing

a field-of-view of $13'' \times 13''$ (see Figure 5.4) as well as a spectral resolution of $R \approx 2650$ within the wavelength range of $5250 \text{ \AA} \lesssim \lambda \lesssim 7400 \text{ \AA}$. Data have been reduced according to already described procedure in the Section 3.2 of Chapter 3.

We compare Gill & O'Brien (2000) and our observations by mimicking their $1''$ -wide slits positions (left panel in Figure 5.4), where the green (red) slit corresponds to WHT/ISIS slit 1 (slit 2). Each slit was centered at the central object's spaxel with the highest S/N. The width of the slits corresponds to 3 spaxels in our setup. The extracted spectra (right panel in Figure 5.4) show velocity ellipses similar to the ones in Figure 5.3, being bright in $H\alpha$ and NII where the $\text{NII} \lambda 6584 \text{ \AA}$ line is much brighter than the $\text{NII} \lambda 6548 \text{ \AA}$, but also revealing very similar clumpiness in the remnant's shell.

Figure 5.5 shows the FOV of the VIMOS-IFU entirely filled with the nova FH Ser. We see its central object, i.e., the unresolved binary system, together with the remnant's shell bright in $H\alpha + \text{NII}$. Due to the high spatial resolution of the instrument, we can separate the central object emission from the shell emission itself and study them separately. This is the first time that such a detailed, high-quality observations have been performed for a nova remnant and we will focus here on showing the resulting data complexity, leaving a more quantitative comparison with models for the future work.

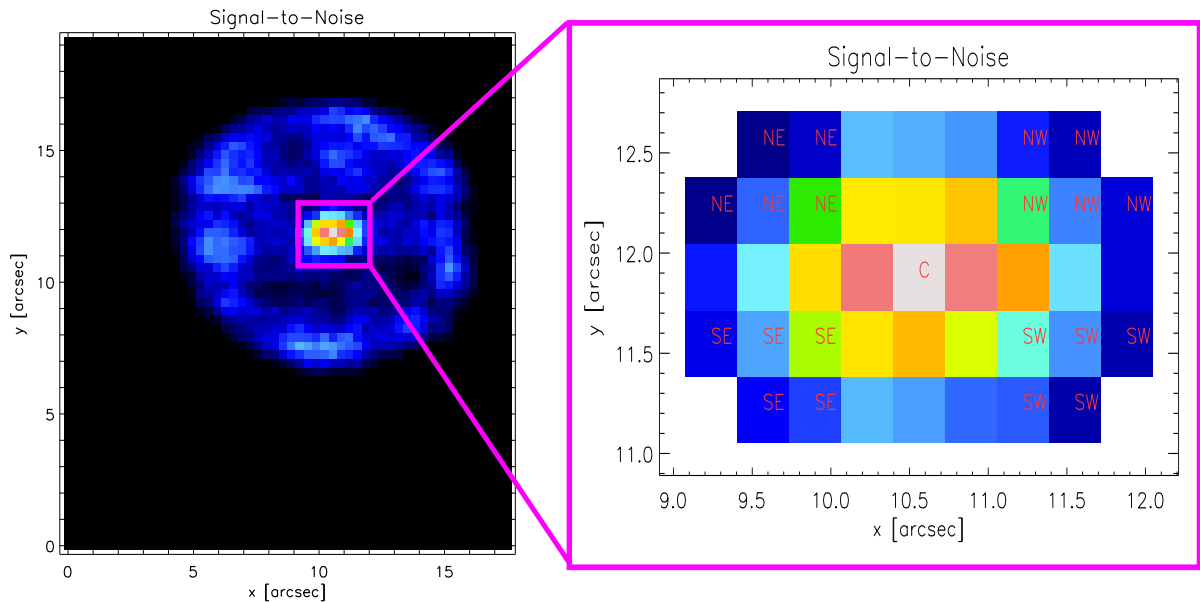


Figure 5.5: The left panel shows signal-to-noise map of FH Ser from our VIMOS-IFU observations. The right panel shows the zoomed-in central object where we indicated different off-center quadrants with *NE*, *SE*, *NW*, *SW* and the central part with *C*.

5.2.1 CENTRAL OBJECT EMISSION OF FH SER

Analyzing spectral profiles from each spaxel of the central object, we have noticed that spaxels around the *central part* (*C*) show similar profiles, which are distinct from the *off-center* profiles of spaxels *NE*, *NW*, *SE*, *SW* (right panel in Figure 5.5). According to this, we have separated the central object emission into 4 quadrants *NE*, *NW*, *SE*, *SW* plus center *C*. In order to test the symmetry of the emission, we start our analysis by extracting spectra from the summed-up spaxels in the eastern part (*SE+NE*) of the object and compared it with the western spectral profile (*SW+NW*). The same we did for the southern (*SE+SW*) and northern part (*NE+NW*). The observed profiles are shown in Figure 5.6. The very similar profiles imply close-to spherical symmetry.

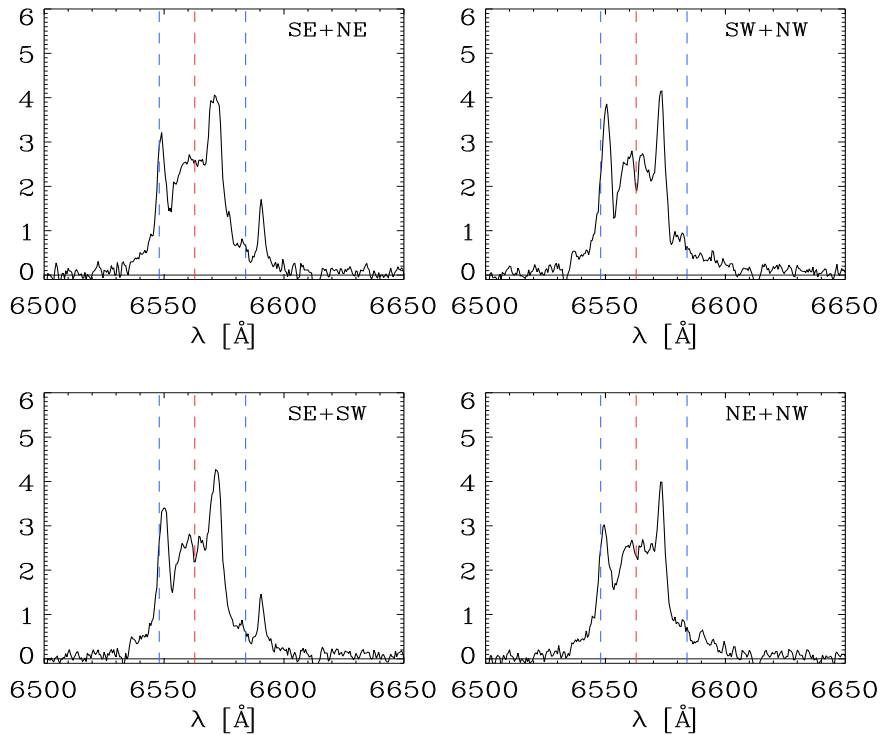


Figure 5.6: VIMOS-IFU observed eastern (*SE+NE*), western (*SW+NW*), southern (*SE+SW*) and northern (*NE+NW*) spectral profiles averaged over number of spaxels. Vertical dashed lines show rest frame $H\alpha$ $\lambda 6562.8$ Å (red) and NII $\lambda\lambda 6549, 6584$ Å (blue).

We have then refined our spatial coverage by extracting spectra from the regions *SE*, *NE*, *SW*, *NW* alone, and the central part *C*. The profiles, averaged over the number of spaxels, are shown in Figure 5.7, where we also show the spectrum of summed-up all spaxels of the entire central object (*all*) in black. For a better comparison, we have re-scaled all the intensities to match the latter combined $H\alpha$ $\lambda 6562.8$ Å intensity.

As pointed out by Della Valle et al. (1997), the central part emission (*C*-profile) might represent the emission of the accretion disk of the nova binary system, where we have a superposition of two components of approximately 420 km s^{-1} (FWHM). This value might indicate the rotational velocity of the accretion disc's outer edge. Since the inclination of the orbital plane to the line-of-sight is small, the contribution from the projection effects should also be very small. However, our spatial scale ($0''.33 \approx 10^{-3} \text{ pc}$) is around 5 orders of magnitude larger than a typical separation between the two components in a CBS, and, therefore, the accretion disc remains spatially unresolved. Since the spaxels around spaxel *C* have the same *C*-profiles, we doubt that the emission of the accretion disc has a large impact. As we will see in the next section, the geometry of a nova envelope ejection might be a more plausible explanation instead.

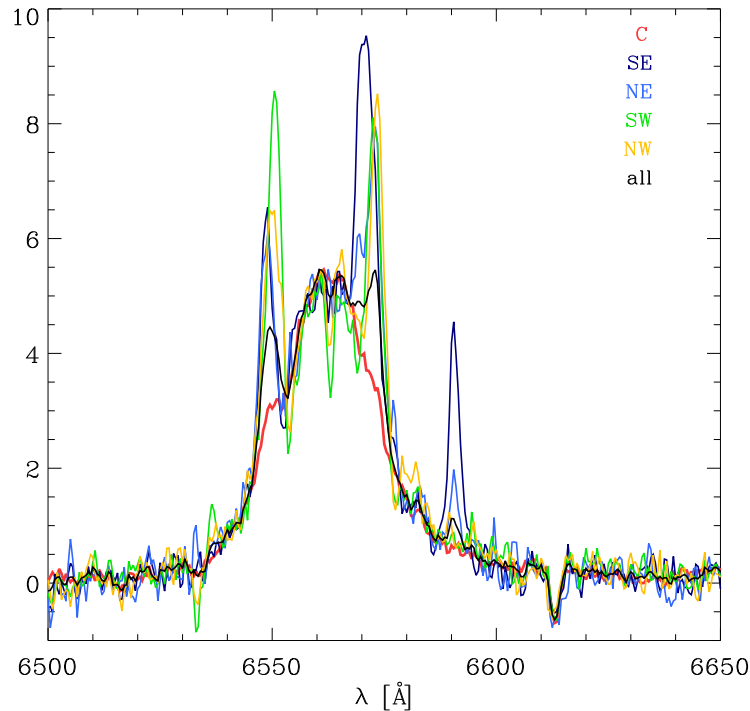


Figure 5.7: Overplotted observed *SE*, *NE*, *SW*, *NW* and *C* spectral profiles averaged over spaxel number, and re-scaled to the combined (*all*) spectrum in black.

5.2.1.1 GEOMETRY OF A NOVA EJECTION

Contrary to the *C*-profile, the *off-center* profiles are dominated by two distinct peaks at around 6550 \AA and 6570 \AA . Even though the first peak coincides with the $\text{NII} \lambda 6548 \text{ \AA}$ line, it is very unlikely to be the case especially since this line should be ≈ 3 times fainter than $\text{NII} \lambda 6584 \text{ \AA}$ line (see also Figure 5.4). We speculate that this emission-line structure arise from the geometry of the envelope ejection and the inclination of a prolate ellipsoid to the line-of-sight. Similar profiles were reported for the nova HR Del (Hutchings 1972) where the analysis included the geometry of polar blobs and equatorial ring (Figure 5.8).

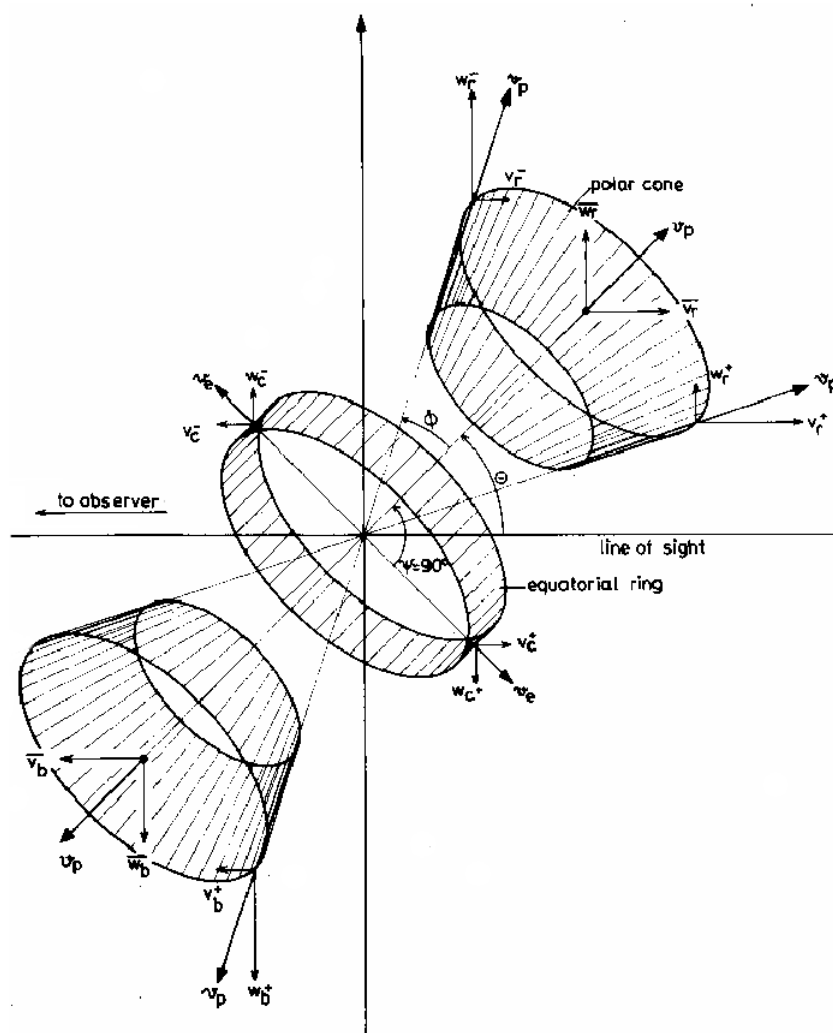


Figure 5.8: Illustration of the geometry of an envelope ejection in a nova which includes polar cones and equatorial ring. Credit: Hutchings (1972).

Hutchings (1972) modeled the profiles for different polar cone angles and a fixed inclination angle of 60° . The result is shown in Figure 5.9. Small cone angles 0° – 20° (30°) give double-peak profiles. Increasing the cone angle, the profile center starts filling in showing less prominent double peaks, and eventually forms the third peak. For very large cone angles ($\gtrsim 70^\circ$), line profile becomes single and rounded. In case the cone is partially filled with the expanding material 20° – 50° (30° – 70°), line profile shows more prominent three peaks (right column in Figure 5.9).

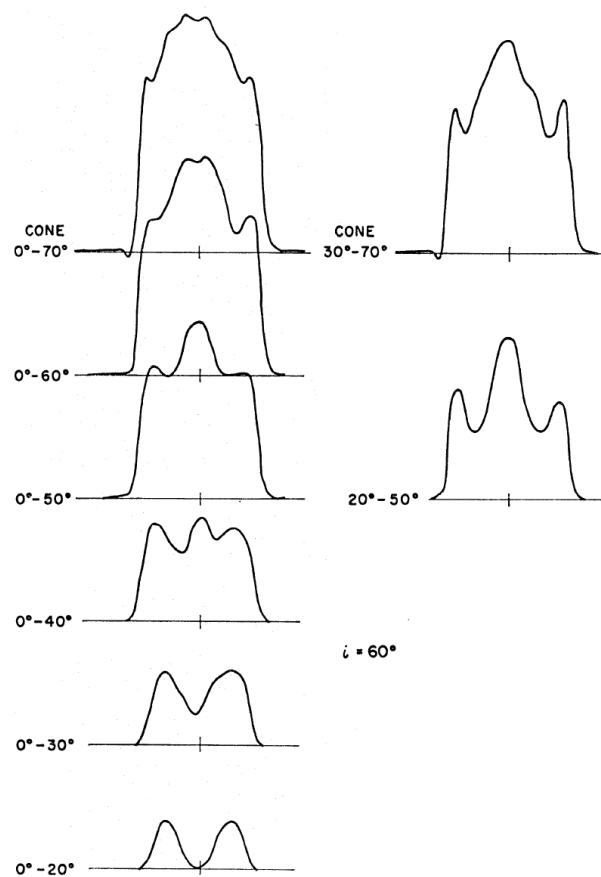


Figure 5.9: Polar cone profiles for uniform expansion velocity and inclination of 60° . Left (right) column shows profiles for entirely (partially) filled cones. Credit: Hutchings (1972).

Hutchings (1972) also modeled equatorial ring profiles for different inclination and ring angles, i.e., ring thickness (Figure 5.10). The ring model characteristics are the presence of double-peak profiles (for inclination angle $i > 10^\circ$) and a wide separation between them emerging with increasing inclination (left column) or making rings thinner (right column). Double-ring models give a possibility of four-peak line profiles. Uniform expansion velocity was assumed in all polar cone and equatorial ring models.

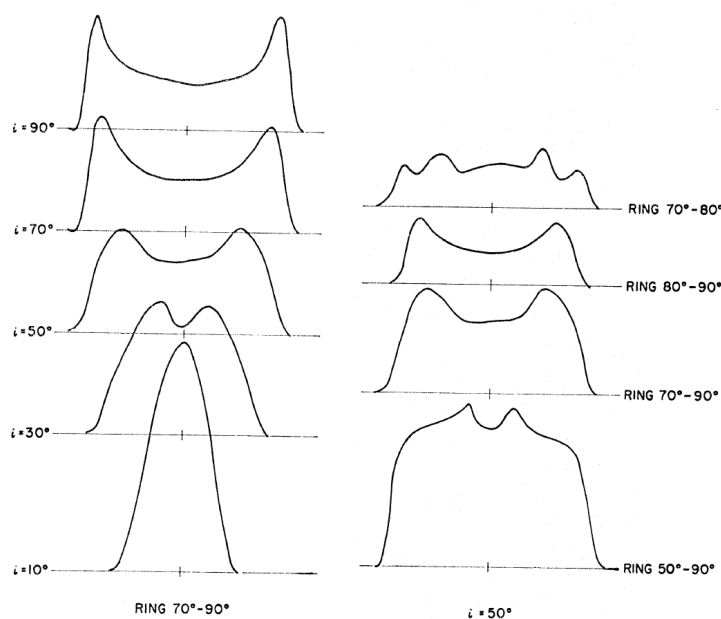


Figure 5.10: Equatorial ring profiles for uniform velocity expansion and different inclination (left column) and ring angles (right column). Credit: Hutchings (1972).

Comparing to our observations, we find that for inclination of 60° and uniform expansion velocity, polar cone angles of $0^\circ-60^\circ$ explain well our observed *C*-profile. Investigating *off-center* profiles, we find that the equatorial ring angles of $70^\circ-90^\circ$ together with the small contribution from the polar cone match reasonably well our observations.

To quantify the relative contribution of different envelope geometries, we measured in each spectrum (Figure 5.11), the flux for its inner part (green) and separately for the two peaks, one at 6550 \AA (blue) and the other at 6570 \AA (red) and show the results in Figure 5.12. The panels show relative contribution of each component (blue, green, red) to the overall line flux. The central spaxels are completely dominated by the green part, while the off-center spaxels show prominent blue and red peaks with the lower green part flux contribution.

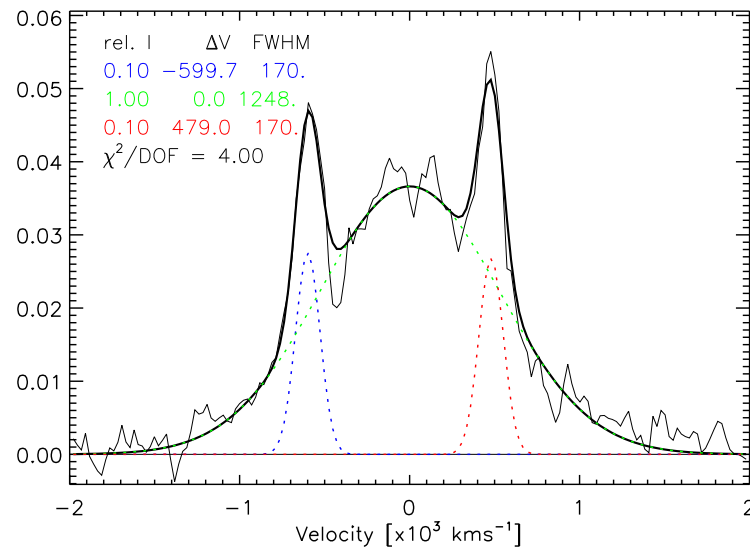


Figure 5.11: Example of fitting one of the spaxel profiles from the central object emission region. Green dotted line fits the inner part of the spectrum, blue and red dotted lines fit the blue peak at 6550 Å and the red peak at 6570 Å, respectively. Black solid line is the total fit. The blue and red peaks' widths were fixed to 170 km s⁻¹ in order to get reasonably good flux estimation in the peaks. Even though we see two blended components in the inner part, we used one-component fit because we are interested only in the total flux of the inner part. Velocity centroids ΔV and FWHM of the components are given in km s⁻¹. We also show relative intensities of the blue and red components with respect to the inner part intensity.

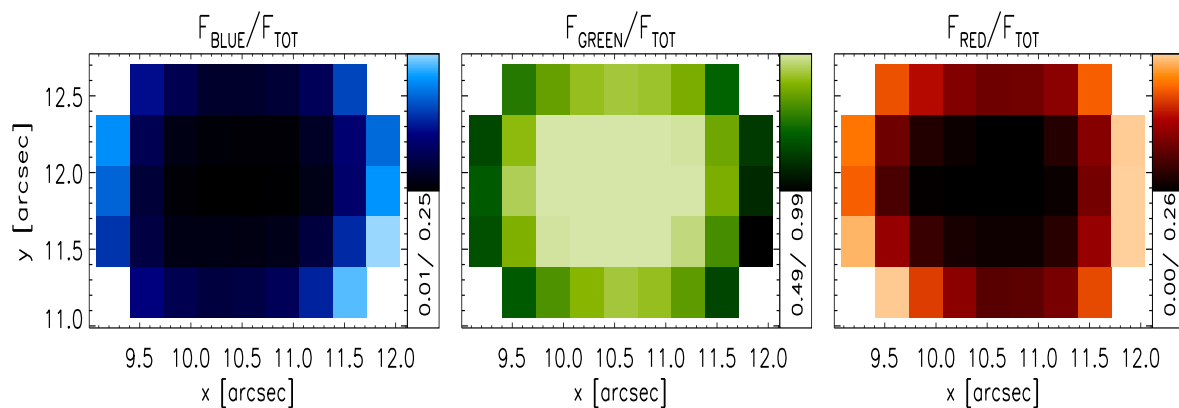


Figure 5.12: Relative flux contribution of the peak at 6550 Å, the inner part of the line profile and the peak at 6570 Å to the overall line flux, indicated as blue, green and red plots, respectively.

All previous conclusions/models are restricted to constant velocity and geometry playing major effects in shaping the line profiles. Once we construct the geometrical model which matches our observations, we will be able to investigate the density and velocity profiles of the ejected envelope.

5.2.1.2 DENSITY AND VELOCITY PROFILES

If we put aside ejection geometry effects and want to compare our observations with the predicted (theoretical) profiles for different density (ρ) and velocity (v) field profiles, we have the 5 different scenarios:

- I const v & const ρ
- II (a) const v & increasing ρ ($\rho \uparrow$)
(b) const v & decreasing ρ ($\rho \downarrow$)
- III (a) const ρ & increasing v ($v \uparrow$)
(b) const ρ & decreasing v ($v \downarrow$)
- IV (a) $v \uparrow$ & $\rho \uparrow$
(b) $v \downarrow$ & $\rho \downarrow$
- V (a) $v \uparrow$ & $\rho \downarrow$
(b) $v \downarrow$ & $\rho \uparrow$

In Figure 5.13 we present theoretical profiles for the above 5 scenarios for the summed-up spaxels in the whole central object (*whole sphere*³). Wherever we have (a) and (b) cases, we have plotted only (a), because (b) case gives the same final profiles. We show wavelength and thus velocity on the x-axis and flux as a linear function of density on the y-axis. The darkest color indicates the lowest velocity, while the faintest color gives the highest velocity. The final profile is the superposition of the colored boxes and is shown with the bordered black line. We have noticed three things here. First, the sign of gradient is degenerate. Second, we see that non-flat profiles imply non constant velocity. Finally, scenario IV and V show different peakiness as a result of a sign reversal. All this applies to *off-center* profiles as well, which should be the same as the *whole sphere* profiles, but narrower (Figure 5.14).

³Whole sphere (*all*) refers to theoretical (observed) profile of summed-up spaxels in the whole central object.

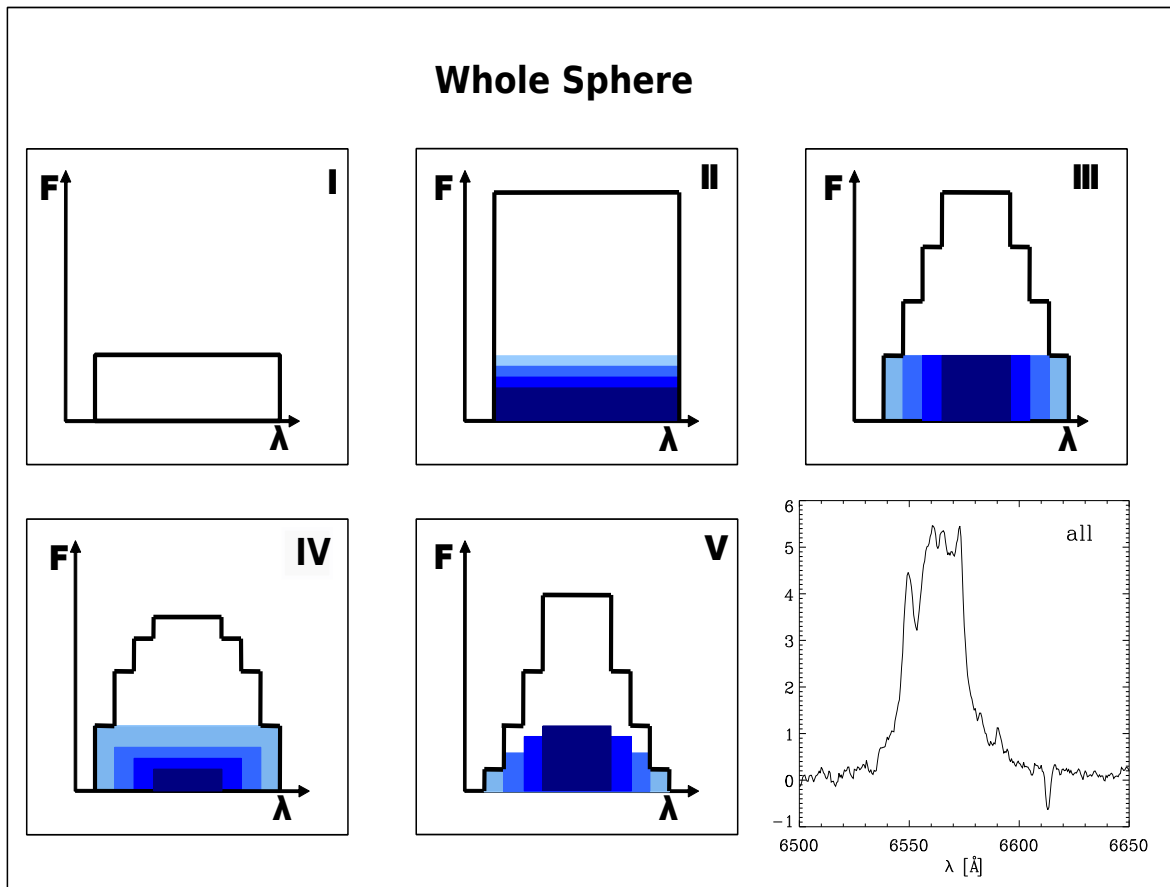


Figure 5.13: The expected line profiles for five different density and velocity profile behaviors in the case of the summed-up spaxels in the whole central object (here called *whole sphere*). The colored boxes represent v and ρ variations, where the darkest color indicates the lowest velocity dispersion, while the faintest color gives the highest velocity dispersion. The final profile is the superposition of the colored boxes and is shown with the bordered black line. The observed profile is shown in the bottom-right corner.

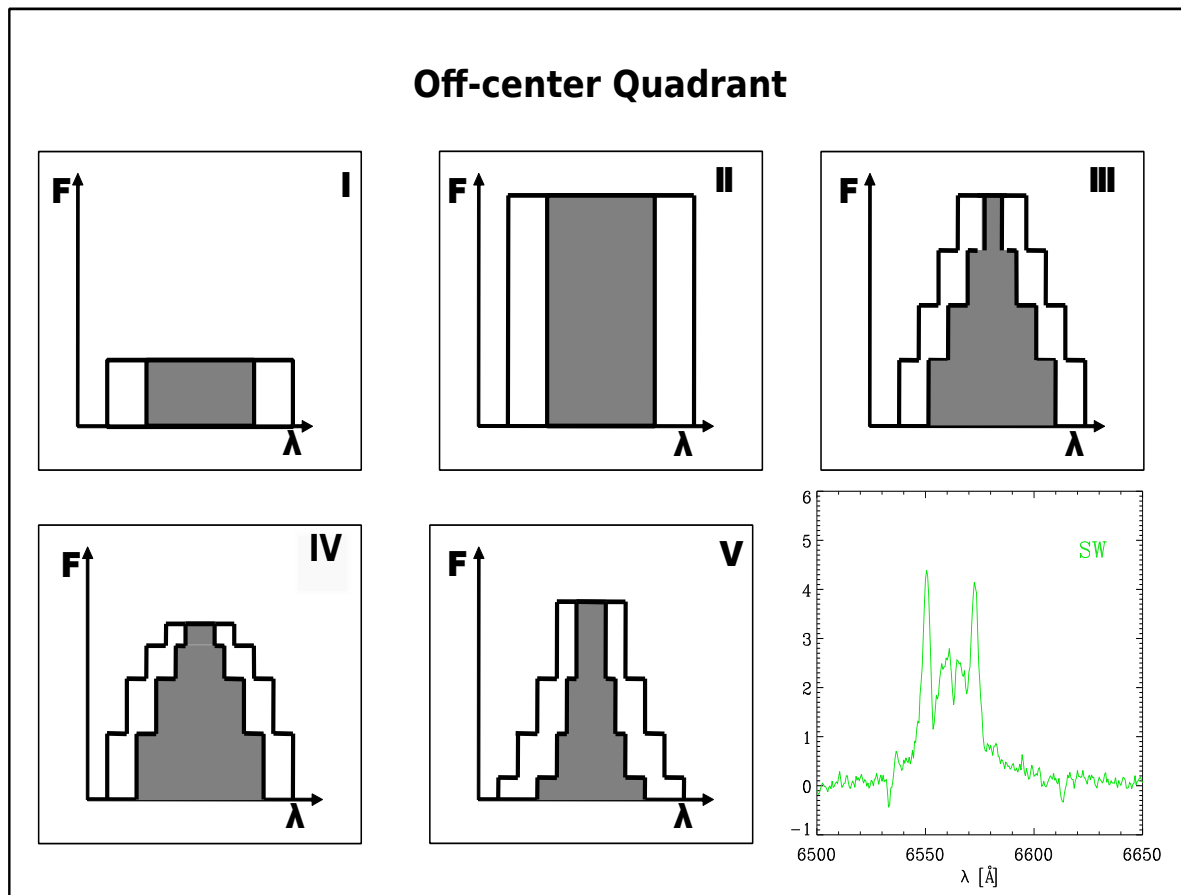


Figure 5.14: The *off-center quadrant* profiles from NE, NW, SE, SW (shaded regions) are expected to be the same in shape but narrower than the ones of the *whole sphere* (broader white region). The observed profile is shown in the bottom-right corner.

The situation is a bit different when looking into observed and predicted profiles for the central part emission (Figure 5.15). First of all, these profiles are less degenerate than those of the *whole sphere*, i.e., here we cannot distinguish only between *I* and *II* scenarios. Contrary to the *whole sphere* and the *off-center* quadrants where we cannot make any conclusion on the velocity and density profiles without taking into account geometric effects, the central part is well explained by scenario *V* of increasing velocity v and decreasing density ρ with radius.

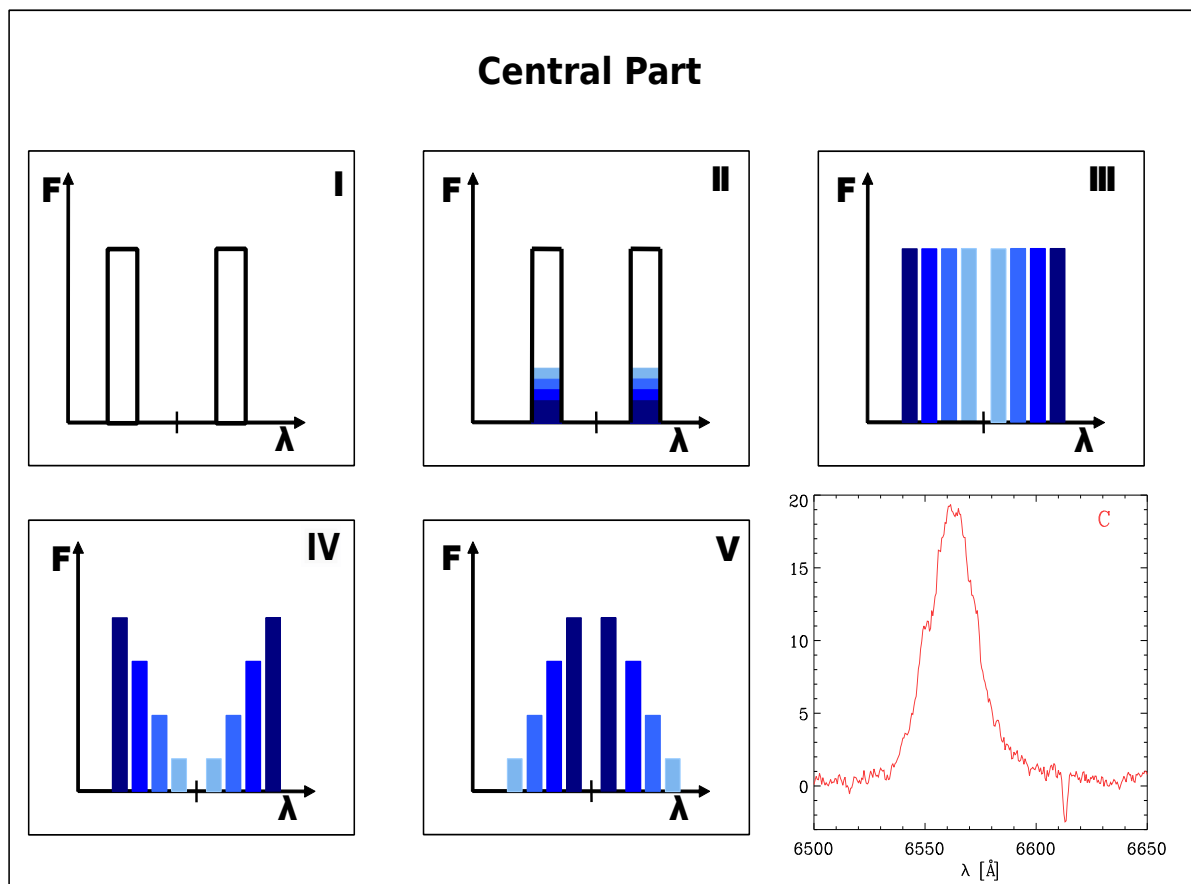


Figure 5.15: The expected C-profiles, with the coloring same as before.

Chevalier (1982) studied the interaction of a uniformly expanding gas and the stationary ambient medium with its application to explosive SN events. For SNe Ia, the model indicates steep power law density profile ($\rho \propto r^{-7}$) of the ejecta and uniform density profile of the ambient medium. This model has successfully been applied to Tycho's SNR, reproducing the basic dynamical and morphological properties of the remnant. In the case of SNe II, the ejecta interacts with the circumstellar material (regions of pre-supernova mass loss) with ambient density $\rho_0 \propto r^{-2}$. Also, in explosive events, one would expect an accelerating shock in the outer layers of the envelope.

The suggested envelope ejection scenario for FH Ser, which is classified as a slow nova, is radiation pressure rather than an explosion. If a common envelope would exist, the ambient density profile should be somewhat similar to the profile of circumstellar material. Several models of nova atmospheres (Bode & Evans 2008) yield $\rho \propto r^{-10}$ in the early phase of a nova outburst, and $\rho \propto r^{-(2-3)}$ in the latest phases. The velocity profile is usually a free parameter in these models, but generally it follows either a linear trend in the early phases or have wind profiles $V(r) = V_{\infty}(1 - a/r)^b$ in the later ones, where V_{∞} , a and b are the constants to be constrained from observations. Above qualitative comparison indicates that it will be feasible to infer both geometry and density and velocity profiles from our data. However, the construction of such detailed and complex models are beyond the current presentation of the data.

5.2.2 THE OUTER RIM EMISSION OF FH SER

The nature of binary system and the ejection mechanism define the shape of the remnant's shell prior to and within the first years from a nova outburst. A prolate ellipsoidal model of the expanding FH Ser nebula (Gill & O'Brien 2000) was based on the HST image and WHT long-slit spectroscopy. As shown in the previous section, the VIMOS-IFU high quality data provides a good opportunity to study the shape of the whole nebula in much more detail. It is not excluded that the central object emission and the outer rim emission of the remnant might follow different hydrodynamical models, especially given that material was ejected multiple times during the outburst. It was previously reported (Friedjung 1989) that during the first 60 days after the outburst the material was ejected at different velocities, 700 km s^{-1} and at a velocity increasing over this period from about 1300 to 1900 km s^{-1} seen through different absorption-line structures. Moreover, no one before has studied the central object emission of this remnant separately.

Remnants can be reshaped by their environments, but they also retain imprints from the geometry of their progenitors. Speed classes of novae and their shapes seem to correlate with each other. Faster novae produce approximately circular shells with random, discrete very bright and large clumps compared to the shell's radius. More structured shells with polar blobs and equatorial rings are characteristic for slower novae, like FH Ser. Slower novae spend more time in the common-envelope phase, which is believed to follow most of classical novae outbursts. Therefore, the orbital motion of the binary systems affects their remnants more.

5.2.2.1 MODELS OF CLASSICAL NOVA SHELLS

A series of hydrodynamical models of classical nova shells have been reviewed by Gill & O'Brien (1999) and compared to emission line profiles which we will summarize here. Figure 5.16 shows calculated line profiles for an ellipsoidal shell with one equatorial ring and two polar caps seen at four different inclination angles.

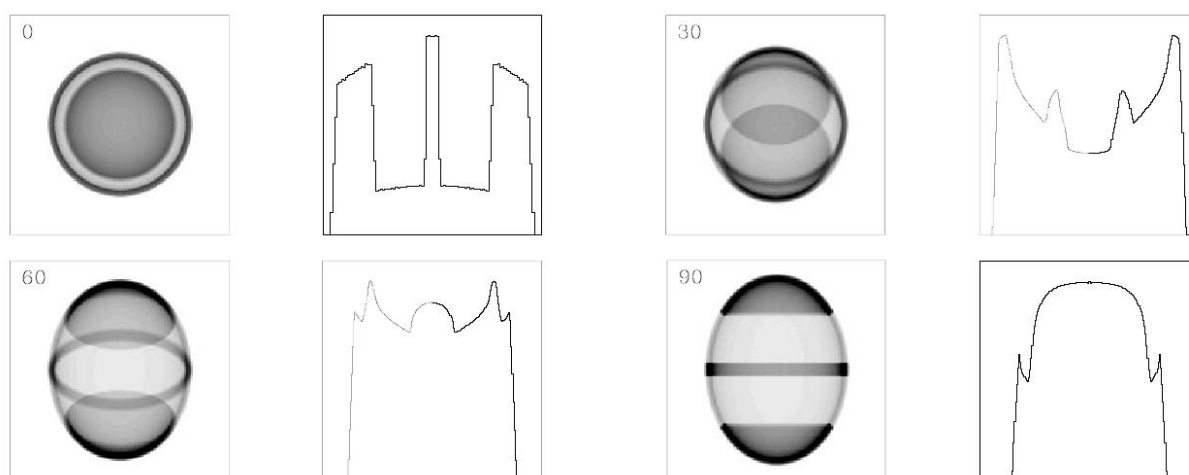


Figure 5.16: Ellipsoidal shell model with one equatorial ring and two polar caps shown for inclination angles of 0° , 30° , 60° , and 90° . The spectra present calculated line profiles in each case. Credit: Gill & O'Brien (1999).

Figure 5.17 compares the synthetic images of different simulations and the calculated line emission profiles for a fixed inclination angle of 60° . The top-left panel shows again the ellipsoidal shell model with one equatorial ring and two polar caps, while the top-right panel shows the ellipsoid with one equatorial ring and two polar rings. Lloyd et al. (1997) tested the effects of the binary system on the shape of the ejecta for different speed classes of classical novae. The outburst was modeled in the form of a wind with increasing velocity when passing over the WD's companion, which transfers energy and angular momentum into the envelope. This model showed that all speed classes tend to produce oblate ellipsoidal shells (lower-left panel in Figure 5.17) contrary to the observed prolate ellipsoids. Porter et al. (1998) extended the model of Lloyd et al. (1997) by including the effects of rotation of accreted matter on the WD (bottom-right panel in Figure 5.17). The model seems to be consistent with the observed prolate ellipsoid, where it becomes more prolate with increasing envelope rotation. This model yields similar results as the model of simple equatorial/polar rings (top-right panel in Figure 5.17), but shows a lower equatorial ring prominence and only four peaks.

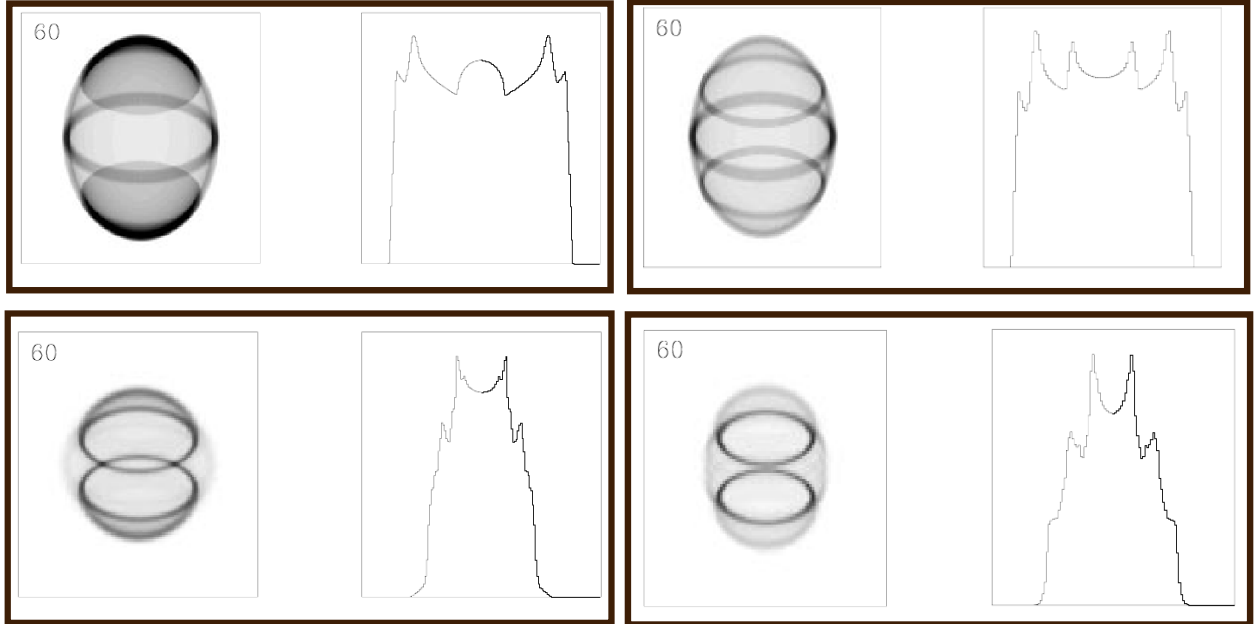


Figure 5.17: Comparison of different hydrodynamical models showing the derived synthetic images and calculated emission line profiles for an inclination angle of 60° . Top row shows ellipsoidal shell with one equatorial ring and two polar caps (top-left) or two polar rings (top-right). Bottom-left panel shows Lloyd et al. (1997) model for fast novae^a with the following parameters: velocity of the ejection $V_{ej}=600 \text{ km s}^{-1}$, velocity of the ejected material in the vicinity of the WD’s companion $V_{ej}^s=3000 \text{ km s}^{-1}$, WD mass $M_{WD}/M_\odot=0.9$, companion mass $M_c/M_\odot=0.45$, orbital period $P_{orb}=4 \text{ h}$, and distance between the components in the binary system $r=3\times 10^9 \text{ cm}$. Bottom-right panel shows the modified Lloyd et al. (1997) model by including the effects of rotation of accreted matter on the WD (Porter et al. 1998). Credit: Gill & O’Brien (1999).

^aEven though FH Ser is classified as a slow nova, similarities between the observed and calculated emission line profiles for Lloyd et al. (1997) model of slow novae are at least not visually obvious. The profiles more resemble to the model of fast novae instead and we decided to show those profiles here.

5.2.2.2 VIMOS-IFU OBSERVATIONS OF FH SER REMNANT’S SHELL

Excluding the central object emission from the rest of the remnant, we have used the software of Cappellari & Copin (2003) to combine neighbouring spectra into spatial Voronoi bins until we reached a signal-to-noise (S/N) of about 150. The result of the binning is shown in Figure 5.18. The numbers show the positions of the bins from which the spectra were extracted and which profiles are shown in Figure 5.19. The profiles of other Voronoi bins are illustrated in Figure 5.20 in the Appendix.

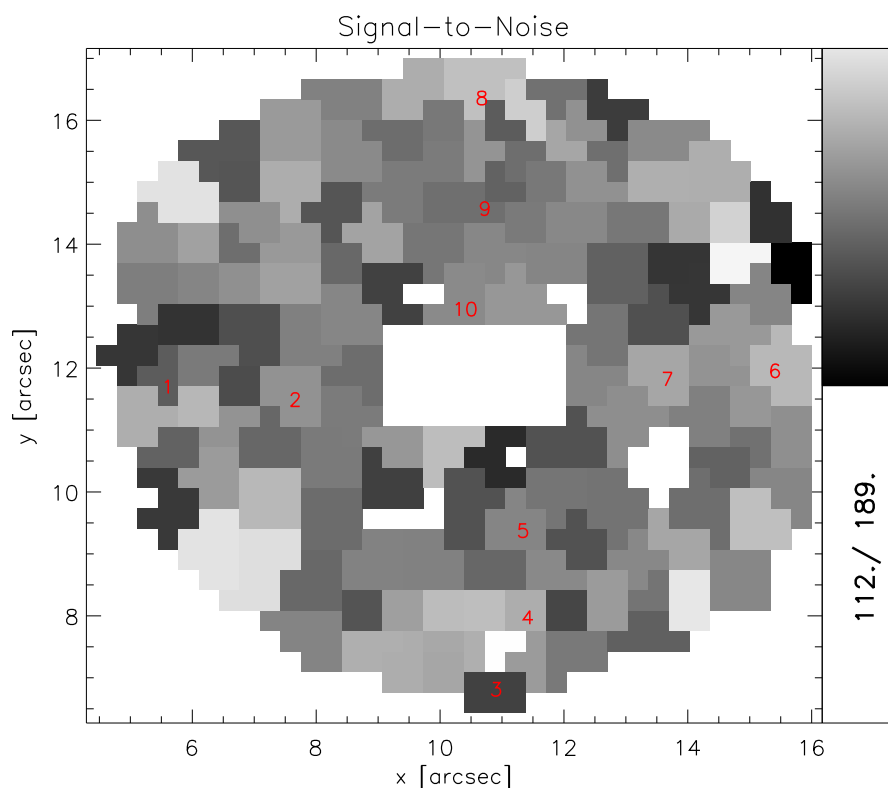


Figure 5.18: Signal-to-noise map of the Voronoi bins created from our VIMOS-IFU observations of FH Ser for the targeting S/N of 150. The numbers indicate the bins used to extract the spectral profiles shown in Figure 5.19.

The spectral profiles range from very simple ones with clear two prominent lines (e.g. bin 5 and 9) to very complex ones (e.g. bin 3 and 4) with multiple line components. Comparing our spectra to the calculated emission line profiles from the models discussed above, it is quite difficult to find similarities between them. Panels 3 and 8 show spectra which to a certain degree resemble to the profiles of an ellipsoid shell with one equatorial ring and two polar caps for an inclination angle of 90° (bottom-right spectrum in Figure 5.16). The same spectra resemble with an even lower degree to the bottom-row spectra in Figure 5.17, i.e., to [Lloyd et al. \(1997\)](#) and [Porter et al. \(1998\)](#) models of fast novae. Panel 4 shows similar line profile to the profile in the top-left panel in Figure 5.16, i.e., when the polar caps are seen pole-on. However, detailed analysis of the lines have to be performed to calculate properly the contribution from equatorial rings and polar caps discussed above. Also, as seen in Figure 5.3 and Figure 5.4, NII velocity rings are bright and have to be properly taken into account when analyzing the spectra. In some of the spectra the position of NII lines coincides with the $H\alpha$ lines from the equatorial ring, and should be disentangled.

Given our high quality data, as a next step we intend to improve the previous prolate ellipsoidal model of the nova nebula based on only two long-slit WHT/ISIS spectra. Next, we plan to use the state-of-the-art shock model of [van Adelsberg et al. \(2008\)](#) to estimate the shock velocity and quantify it all around FH Ser to obtain a three-dimensional velocity mapping of the nova outflow. Finally, in combination with archival HST images, the distance to FH Ser can be improved via the expansion parallax method, and compared to the distance measured by the nebular parallax through the radio images. Improved modeling of the remnant's shell is, thus, necessary in order to derive accurate expansion velocity, and distance to the remnant ([Wade et al. 2000](#)).

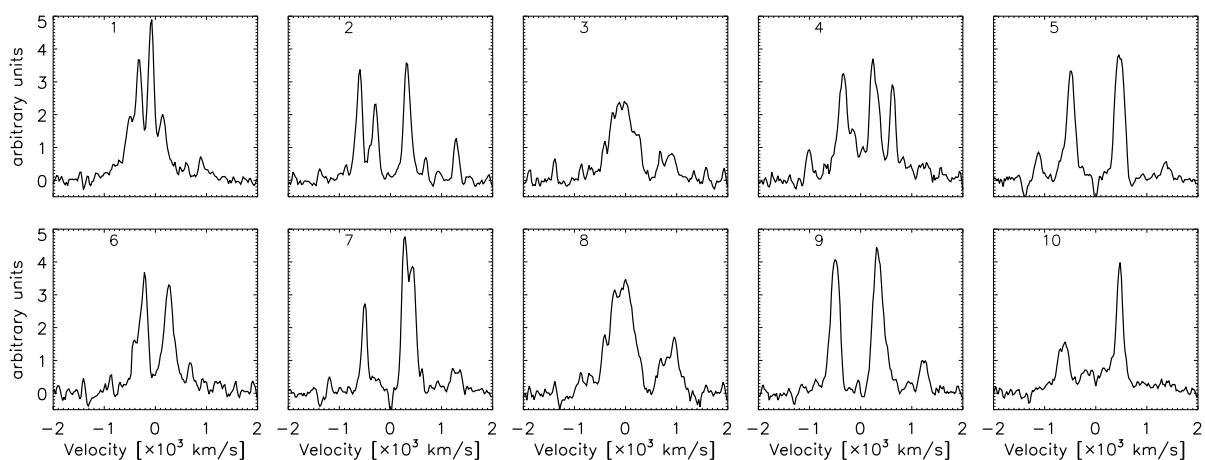


Figure 5.19: Spectra extracted from ten Voronoi bins indicated in Figure 5.18 showing complex line structure.

5.3 SUMMARY

The spectral analysis of the central object provides important information on the mechanisms responsible for the nova outbursts, which are further linked to the assumptions of mass transfer rates and binary progenitors. With the high quality VIMOS-IFU data we are not only able to resolve the central object emission, but with the spatial resolution of $0.''33$ ($\approx 10^{-3}$ pc) per pixel, we can actually analyze its internal parts. We have qualitatively compared the observed profiles with the ones predicted for different envelope ejection geometries on one side, and density and velocity profiles on the other. In order to make strong conclusion on the observed profiles, we need to take into account geometry, velocity and density profiles all together, which is the next step in our research. In addition, we plan to use our data to improve the current prolate ellipsoidal model of the nova nebula, making a three-dimensional velocity mapping of the nova outflow and set a better constraint on the distance to FH Ser.

5.4 APPENDIX

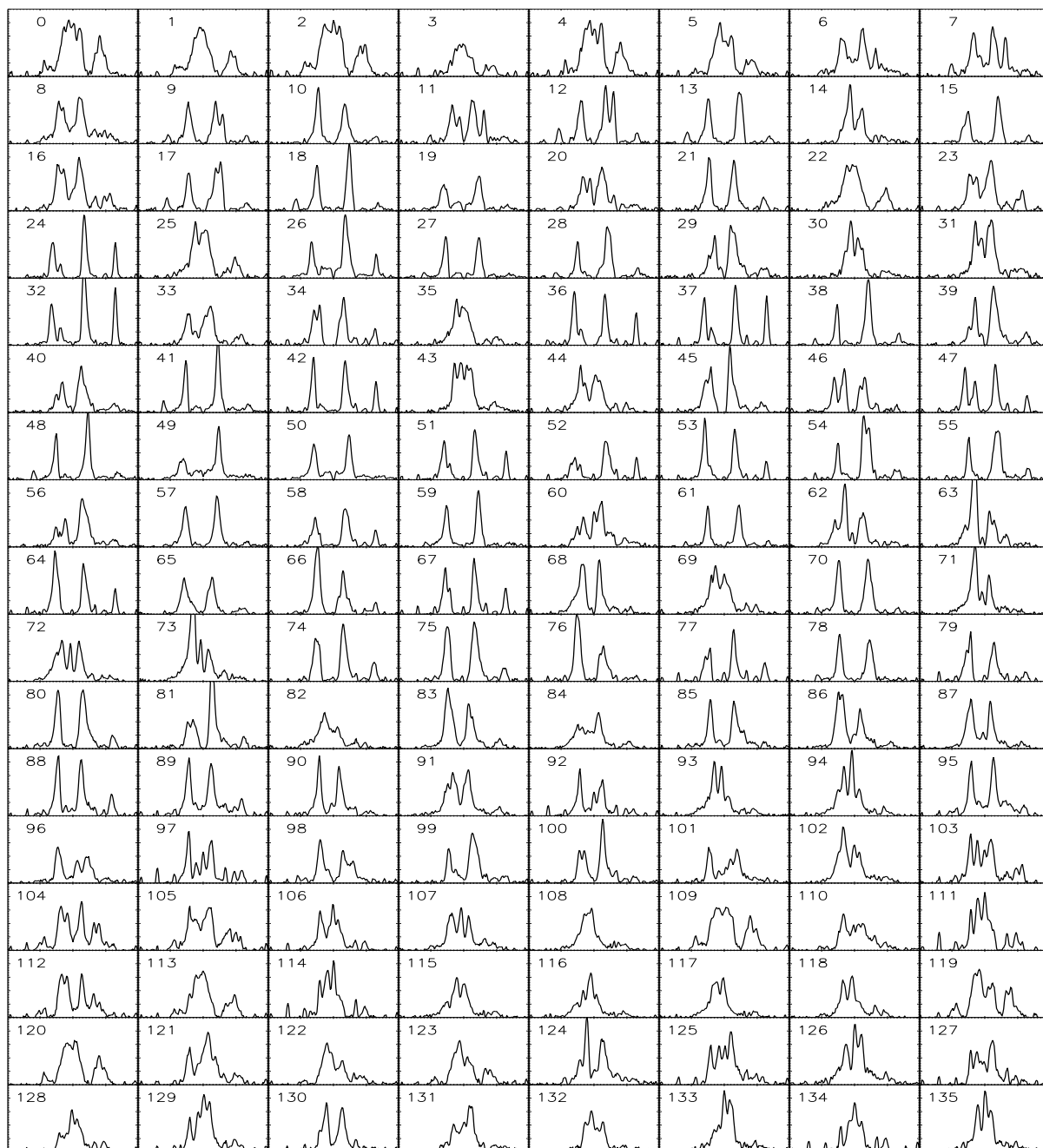


Figure 5.20: Montage of the H α line profiles in each of the 136 Voronoi bins in Figure 5.18. The horizontal axis represents wavelengths and vertical axis is in relative flux units. Note that numbers indicated in Figure 5.18 are different from those in the panels above.

SUMMARY AND OUTLOOK

The research presented in this thesis was centered on using the unique capabilities of high-spatial resolution spectrophotometric imaging to accurately trace and isolate optical shock fronts around different astrophysical objects. Motivation for this came from limited spatial resolution of previous observations which were neither able to explore small-scale spatial variations nor able to separate the contribution of geometric effects to the emission-line properties of the shock front. The derived physical parameters thus might be biased and in turn affect the conclusions drawn on the involved physical processes in the shock.

Our main interest was studying Balmer-dominated shocks around the remnants of supernovae and novae. Balmer-dominated shocks are characterized by strong $H\alpha$ -line emission, with a narrow $\sim 10 \text{ km s}^{-1}$ and a broad $\sim 1000 \text{ km s}^{-1}$ component. The widths and intensities of these components provide us with information on physical conditions, like temperature and thermal equilibration, in the region behind and ahead of the shock front. Moreover, prominent $H\alpha$ -line shocks are a powerful tool for inferring the presence of cosmic rays (CRs) in the shocks. CRs are expected to form a precursor which will compress and heat the pre-shock gas so that the overall shock structure and dynamics changes. Investigating the shape of the resulting two-component $H\alpha$ line has thus the potential to provide observational constraints on the CR precursor:

- (1) CRs will heat the cold neutrals in the interstellar medium before they are being ionized by the shock, resulting in a narrow $H\alpha$ line broadened beyond the thermal $10\text{--}20 \text{ km s}^{-1}$ gas dispersion;
- (2) CRs can carry away energy from the protons in the post-shock, so that the charge exchange between these protons and incoming neutrals from the pre-shock region give rise to a broad $H\alpha$ line with a smaller width than allowed by the fast shock velocity;
- (3) Because the CR precursor is typically spatially unresolved, its additional contribution to the narrow line $H\alpha$ emission results in a decreasing broad-to-narrow intensity line ratio;
- (4) The presence of CRs can cause the shape of the broad $H\alpha$ line to deviate from a Gaussian profile — an additional intermediate $H\alpha$ -line component ($\sim 150 \text{ km s}^{-1}$) might arise from a precursor

of broad neutrals.

We have presented three independent studies in this thesis all with high-spatial resolution spectrophotometric data. In the first of these, we have used an integral-field unit spectrograph targeted at the $H\alpha$ spectral region, to more efficiently and better spatially resolve the shock structure around the historical supernova remnant of SN 1006. Unlike the previous long-slit (one dimensional) technique and Fabry-Pérot interferometry (two dimensional), integral-field spectroscopy results in acquiring three dimensional maps in a single exposure (two dimensions of sky positions and one of wavelength). This novel approach in studying shock physics has put us in the position to minimize the shock geometry contribution to the obtained results. We analyzed spectral profiles at 133 different locations in a small ($\approx 30''$) region on the sky, in which previously only one integrated spectrum was available, and recorded the spatial variation of the broad line widths and broad-to-narrow line intensity ratios. The results point toward presence of suprathermal particles which can trigger particle acceleration processes and produce high energy CRs.

Second, we have used Fabry-Pérot spectroscopy to map narrow $H\alpha$ -line widths along a large part ($\approx 3'$) of another historical remnant, that of SN 1572, better known as Tycho's supernova remnant. Improvements to previous observations are in the better instrument efficiency and spatial scale while at the same time the large field-of-view allowed us to cover a large portion of the remnant. Our results show that the narrow $H\alpha$ line is not well represented by a single narrow Gaussian profile: it is either broadened to $\approx 20\text{-}60\text{ km s}^{-1}$, but more likely requires the contribution of an intermediate component. Additionally, we often find evidence for a second and offset (i.e. a double) narrow line. While the first and the third results can be interpreted either as a CR precursor contribution or geometric effect, the second result, i.e., the indication of an intermediate component implies the presence of a broad-neutral precursor. This precursor has been previously reported, but the regions where the spectra were extracted from had by far lower spatial resolution, i.e., large number of pixels contributed to the final analyzed line profile.

Finally, we have studied shocks around the classical nova FH Ser of 4-5 times lower velocity than around supernova remnants. Our unique high-quality integral-field spectroscopic data allowed us to separate the object in two parts, the central object emission (an unresolved binary system), and the outer nova nebula. Preliminary results revealed a complex structure, where the central object shows indications of two polar blobs plus presence of an equatorial ring, while the nebula, previously modeled as an prolate ellipsoid, needs a much more detailed analysis. Once we reconstruct the nova geometry, our aim is to study velocity and density profiles, which have a memory of a nova outburst history and hence enable us to constrain the nature of the nova progenitor.

In order to advance our understanding of the shock physics, we plan to compare our presented SN 1006 and Tycho data to recently developed state-of-the-art shock models which include a

broad-neutral and CR precursor. We want to see first if the model that includes only the broad neutral precursor can explain the observations, i.e., the observed line profiles and the low intensity ratios (in case of SN 1006) and an intermediate component (in case of Tycho). Then, we plan to see if the model with CR precursor can fit the data better for both cases. Moreover, we hope to constrain the ambient number density and ionization fraction, and see if the shock can be described by a single set of parameters, i.e., if it is homogeneous.

As follow-up observations, we plan to study the northeastern rim of SN 1006 which is ~ 10 times fainter than the northwestern rim which we studied in this thesis. This location we chose because $H\alpha$ emission in that part of the remnant occurs along with non-thermal X-ray emission (which is nearly absent in the northwestern rim), where efficient CR acceleration is likely to occur. The presence of non-thermal X-rays provides direct observational evidence of the presence and properties of CRs. Various science goals can be reached in this way. (i) By comparing shock velocities extracted from the broad $H\alpha$ components using [van Adelsberg et al. \(2008\)](#) model (shock model without any kind of precursor) with shock velocities constrained from non-thermal X-ray proper motions and an independent distance measurement, we can set limits on the CR acceleration efficiency. (ii) A recent theoretical model by [Morlino et al. \(2013b\)](#) that includes non-thermal CR physics will yield the intrinsic shock velocity from the $H\alpha$ observations directly. The intrinsic shock velocity together with the optical proper motion measurements in the northwestern rim of SN 1006 will in turn yield better constraints on the distance. (iii) Observed $H\alpha$ and existing thermal X-ray data in the northeastern rim can provide an independent handle on electron-proton temperature equilibration behind the shock front. The Morlino et al. model will also give electron-proton temperature ratios directly from $H\alpha$ lines which combined with the electron temperature constrained from thermal X-ray spectrum will yield the proton temperature behind the shock front. Having the intrinsic shock velocity and the proton temperature for the same location would enable us to estimate the compression factor. (iv) Knowing the compression factor and the mean energy channeled to CR protons, we can then constrain the fraction of the pressure induced by cosmic rays in the total post-shock pressure.

The northwestern limb of SN 1006 (of which data were presented in Chapter 3) is very unique because it is the brightest $H\alpha$ part of the remnant most likely due to a higher ambient density. On the other hand, other parts of the remnant are very similar in terms of $H\alpha$ brightness. Therefore, it would be worthwhile to observe the southeastern part of SN 1006 where $H\alpha$ emission is detected with the same brightness as in the northeastern rim mentioned in the paragraph above, but unlike there non-thermal X-ray emission is lacking. $H\alpha$ emission usually anticorrelates with non-thermal X-ray emission, and SN 1006 with these two spots both bright in $H\alpha$ might reveal the reason for the anticorrelation — (super)nova remnants are clearly unique laboratories for studying shock physics and CRs, now high-quality and high-spatial resolution spectrophotometric data like presented in this thesis are becoming available.

ACKNOWLEDGEMENTS

At the first place, I would like to thank my supervisor Glenn van de Ven on his enormous support and patience throughout these past four years. He introduced me to the exciting world of observers, completely new to me, wisely guided me through the same and helped me develop many important skills. He was always available for comments, suggestions, informal talks, responding to my silly questions, was there always to listen and understand, advise and support. There are no words in which I could thank him for everything he thought me and for being always there for me. I truly hope we will have the possibility to continue working together.

I am further grateful to Kevin Heng, my theoretical advisor and the person who selflessly shared his knowledge, experience, ideas and thoughts, and made my PhD adventure easier. I thank him very much for his support and continuous encouragement.

Ronald Läscher, what to say... A person who dedicated so much of his time and energy to help me out with the thesis that I will owe him for the rest of my life. I thank him for his ideas, comments, last minute thesis scientific and practical issues. His suggestions and our fruitful discussions contributed enormously to the quality of this work, but also my confidence.

I thank also Rahul Kannan for reviewing parts of my thesis and giving a few important comments that have significantly improved the thesis.

I am very happy that I had the opportunity to be a part of the IMPRS, and I thank Christian Fendt very much for taking care of all students' issues, organizing the school, parties, BBQs and overall support.

I want to thank all my friends who made my stay in Heidelberg unforgettable. Because of you, Heidelberg will always have a special place in my heart.

BIBLIOGRAPHY

- Abdo, A. A., et al. 2010, *Science*, 327, 1103
- Abraham, J., et al. 2010, *Physical Review Letters*, 104, 091101
- Acciari, V. A., et al. 2011, *ApJ*, 730, L20
- Acerro, F., e. 2010, *A&A*, 516
- Acerro, F., Ballet, J., & Decourchelle, A. 2007, *A&A*, 475, 883
- Ackermann, M., et al. 2013, *Science*, 339, 807
- Aharonian, F., Bergstrm, L., & Dermer, C. 2013, *Saas-Fee Advanced Course 40. Swiss Society for Astrophysics and Astronomy*
- Aharonian, F., et al. 2001, *A&A*, 370, 112
- . 2005, *A&A*, 437, 135
- . 2008, *A&A*, 481, 401
- . 2009, *ApJ*, 692, 1500
- Albert, J., et al. 2007, *ApJ*, 664, L87
- Allington-Smith, J., Content, R., & Haynes, R. 1998, *SPIE*, 3355, 196
- Amato, E., & Blasi, P. 2005, *MNRAS*, 364
- . 2006, *MNRAS*, 371, 1251
- Apel, W. D., et al. 2013, *Phys. Rev. D*, 87, 081101
- Axford, W. I., Leer, E., & Skadron, G. 1977, *International Cosmic Ray Conference*, 11, 132
- Baade, W., & Zwicky, F. 1934, *Proceedings of the National Academy of Science*, 20, 259
- Badenes, C., & Maoz, D. 2012, *ApJL*, 749
- Bamba, A., Yamazaki, R., Yoshida, T., Terasawa, T., & Koyama, K. 2005, *ApJ*, 621, 793
- Bath, G. T., & Shaviv, G. 1976, *MNRAS*, 175, 305
- Bedin, L. R., RuizLapuente, P., González Hernández, J. I., Canal, R., Filippenko, A. V., &

- Méndez, J. 2014, MNRAS, 439, 354
- Bell, A. R. 1978, MNRAS, 182, 443
- Bell, A. R., & Lucek, S. G. 2001, MNRAS, 321, 433
- Berezhko, E. G. 2008, ApJ, 684
- Berezhko, E. G., Ksenofontov, L. T., & Völk, H. J. 2002, A&A, 395, 943
- Berezhko, E. G., Ksenofontov, L. T., & Völk, H. J. 2003, A&A, 412
- Blair, W. P., Long, K. S., & Vancura, O. 1991, ApJ, 366, 484
- Blandford, R., & Eichler, D. 1987, Phys. Rep., 154, 1
- Blandford, R. D., & Ostriker, J. P. 1978, ApJ, 221
- Blasco-Herrera, J., et al. 2010, MNRAS, 407, 2519
- Blasi, P. 2013, A&A Rev., 21, 70
- Blasi, P., Morlino, G., Bandiera, R., Amato, E., & Caprioli, D. 2012, ApJ, 755, 121
- Bode, M. F., & Evans, A. 2008, Classical Novae, Cambridge Astrophysics Series 43, Second Edition
- Borkowski, K. J., Shull, J. M., & McKee, C. F. 1989, ApJ, 336, 979
- Boulares, A., & Cox, D. P. 1988, ApJ, 333, 198
- Burleigh, M. R., Heber, U., O'Donoghue, D., & Barstow, M. A. 2000, A&A, 356, 585
- Bychkov, K. V., & Lebedev, V. S. 1979, A&A, 80, 167
- Cappellari, M., & Copin, Y. 2003, MNRAS, 342, 345
- Cappellaro, E., & Turatto, M. 1997, Thermonuclear Supernovae, ed. P. Ruiz-Lapuente et al. (Kluwer, Dordrecht)
- Caprioli, D., & Spitkovsky, A. 2013, ApJ, 765
- Cargill, P. J., & Papadopoulos, K. 1988, ApJ, 329
- Cassam-Chenaï, G., Hughes, J. P., Reynoso, E. M., Badenes, C., & Moffett, D. 2008, ApJ, 680, 1180
- Cesarsky, C. J. 1980, ARAA, 18, 289
- Chevalier, R. A. 1982, ApJ, 258, 790
- Chevalier, R. A., Kirshner, R. P., & Raymond, J. C. 1980, ApJ, 235, 186
- Chevalier, R. A., & Raymond, J. C. 1978, ApJ, 225
- Chiotellis, A., Schure, K. M., & Vink, J. 2012, A&A, 537
- Colgate, S. A., & White, R. H. 1966, ApJ, 143, 626
- Cox, D. P. 1972, ApJ, 178, 159
- Darnley, M. J., Bode, M. F., & Kerins, E. J. et al. 2006, MNRAS, 369, 257
- Della Valle, M., Gilmozzi, R., Bianchini, A., & Esenoglu, H. 1997, A&A, 325, 1151
- Della Valle, M., & Livio, M. 1995, ApJ, 452, 704
- Dilday, B., et al. 2012, Science, 337, 942
- Downes, R. A., & Duerbeck, H. W. 2000, AJ, 120, 2007

- Downes, R. A., Duerbeck, H. W., & Delahodde, C. E. 2001, *J. Astron. Data*, 7, 6
- Drain, B. T., & McKee, C. F. 1993, *ARA&A*, 31, 373
- Drury, L. 1983, *Reports on Progress in Physics*, 46, 973
- Drury, L., Aharonian, F. A., Malyshev, D., & Gabici, S. 2009, *A&A*, 496, 16
- Edwards, Z. I., Pagnotta, A., & Schaefer, B. E. 2012, *ApJ*, 747
- Ellison, D. C., Patnaude, D. J., Slane, P., & Raymond, J. 2010, *ApJ*, 712, 287
- Enomoto, R., et al. 2002, *Nature*, 416, 823
- Fermi, E. 1949, *Physical Review*, 75, 1169
- Filippenko, A. V. 1997, *ARA&A*, 35, 309
- Fowler, W. A., & Hoyle, F. 1964, *ApJS*, 9, 201
- Friedjung, M. 1989, in *Classical Novae*, ed. M. F. Bode & A. Evans, 187–214
- Friedman, H. W., Linson, L. M., Patrick, R. M., & Petschek, H. E. 1971, *Ann. Rev. Fluid Mech.*, 3, 63
- Gallagher, J. S., & Code, A. D. 1974, *ApJ*, 189, 303
- Gallagher, J. S., & Starrfield, S. G. 1976, *MNRAS*, 176, 53
- Geisel, S. L., Kleinmann, D. E., & Low, F. J. 1970, *ApJ*, 161
- Ghavamian, P., Laming, J. M., & Rakowski, C. E. 2007, *ApJ*, 654
- Ghavamian, P., Raymond, J., Smith, R. C., & Hartigan, P. 2001, *ApJ*, 547, 995
- Ghavamian, P., Raymond, J. C., Hartigan, P., & Blair, W. P. 2000, *ApJ*, 535, 266
- Ghavamian, P., Winkler, P. F., Raymond, J. C., & Long, K. S. 2002, *ApJ*, 572, 888
- Gill, C. D., & O'Brien, T. J. 1999, *MNRAS*, 307, 677
- . 2000, *MNRAS*, 314, 175
- Giordano, F., et al. 2012, *ApJ*, 744, L2
- González Hernández, J. I., RuizLapuente, P., Filippenko, A. V., Foley, R. J., GalYam, A., & Simon, J. D. 2009, *ApJ*, 691, 1
- González Hernández, J. I., RuizLapuente, P., Tabernero, H. M., Montes, D., Canal, R., Méndez, J., & Bedin, L. R. 2012, *Nature*, 489, 533
- Hamilton, A. J. S., & Fesen, R. A. 1988, *ApJ*, 327, 178
- Hamilton, A. J. S., Fesen, R. A., & Blair, W. P. 2007, *MNRAS*, 381, 771
- Heald, G. H., Rand, R. J., Benjamin, R. A., & Bershady, M. 2007, *ApJ*, 663, 933
- Helder, E. A., Kosenko, D., & Vink, J. 2010, *ApJ*, 719, L140
- Helder, E. A., Vink, J., Bleeker, J. A. M., Burrows, D. N., Ghavamian, P., & Yamazaki, R. 2013, *MNRAS*, 435, 910
- Helder, E. A., Vink, J., Bykov, A. M., Ohira, Y., Raymond, J. C., & Terrier, R. 2012, *Space Sci. Rev.*, 173, 369
- Helder, E. A., et al. 2009, *Science*, 325, 719
- Heng, K. 2010, *PASA*, 27, 23

- Heng, K., & McCray, R. 2007, *ApJ*, 654, 923
- Heng, K., van Adelsberg, M., McCray, R., & Raymond, J. C. 2007, *ApJ*, 668, 275
- Hernandez, O., et al. 2008, ArXiv e-prints
- Hester, J. J., Raymond, J. C., & Blair, W. P. 1994, *ApJ*, 420, 721
- Hewitt, J. W., Yusef-Zadeh, F., & Wardle, M. 2009, *ApJ*, 706
- Hillebrandt, W., & Niemeyer, J. C. 2000, *ARA&A*, 38, 191
- Honda, M. 1970, *IAU Circ*, 2214
- Hörandel, J. R. 2006, *Journal of Physics Conference Serie*, 47, 41
- Hoyle, F., & Fowler, W. A. 1960, *ApJ*, 132, 565
- Hubble, E. P. 1929, *ApJ*, 69, 103
- Husemann, B., Kamann, S., Sandin, C., Sanchez, S. F., Garcia-Benito, R., & Mast, D. 2012, *A&A*, 545
- Hutchings, J. B. 1972, *MNRAS*, 158, 177
- Hwang, U., Decourchelle, A., Holt, S. S., & Petre, R. 2002, *ApJ*, 581, 1101
- Hyland, A. R., & Neugebauer, G. 1970, *ApJL*, 160
- Iben, I., & Tutukov, A. V. 1984, *ApJS*, 54, 335
- Kamper, K. W., & van den Bergh, S. 1978, *ApJ*, 224, 851
- Kang, H., Jones, T. W., & Gieseler, U. D. J. 2002, *ApJ*, 579, 337
- Katsuda, S., Petre, R., Hughes, J. P., Hwang, U., Yamaguchi, H., Hayato, A., Mori, K., & Tsunemi, H. 2010, *ApJ*, 709, 1387
- Kerzendorf, W. E., Schmidt, B. P., & Asplund, M., e. 2009, *ApJ*, 701, 1665
- Kerzendorf, W. E., Schmidt, B. P., Laird, J. B., Podsiadlowski, P., & Bessell, M. S. 2012, *ApJ*, 159, 7
- Kerzendorf, W. E., Yong, D., & Schmidt, B. P., e. 2013, *ApJ*, 774, 99
- Kjaer, K., Leibundgut, B., Fransson, C., Gröningsson, P., Spyromilio, J., & Kissler-Patig, M. 2007, *A&A*, 471, 617
- Kohta, M., D., D. C., Takami, H., & Migliori, G. 2012, *ApJ*, 749, 63
- Koyama, K., Kinugasa, K., Matsuzaki, K., Nishiuchi, M., Sugizaki, M., Torii, K., Yamauchi, S., & Aschenbach, B. 1997, *PASJ*, 49
- Koyama, K., Petre, R., Gotthelf, E. V., Hwang, U., Matsuura, M., Ozaki, M., & Holt, S. S. 1995, *Nature*, 378, 255
- Krymskii, G. F. 1977, *Akademiia Nauk SSSR Doklady*, 234, 1306
- Laming, J. M., Raymond, J. C., McLaughlin, B. M., & Blair, W. P. 1996, *ApJ*, 472, 267
- Lee, J.-J., Koo, B.-C., Raymond, J. C., Ghavamian, P., Pyo, T.-S., Tajitsu, A., & Hayashi, M. 2007, *ApJ*, 659
- Lee, J.-J., Koo, B.-C., & Tatematsu, K. 2004, *ApJ*, 605, L113
- Lee, J.-J., Raymond, J. C., Park, S., Blair, W. P., Ghavamian, P., Winkler, P. F., & Korreck, K.

- 2010, *ApJ*, 715, L146
- Lim, A. J., & Raga, A. C. 1996, *MNRAS*, 280, 103
- Liu, J., Di Stefano, R., Wang, T., & Moe, M. 2012, *ApJ*, 749, 141
- Lloyd, H. M., O'Brien, T. J., & Bode, M. F. 1997, *MNRAS*, 284, 137
- Long, K. S., Reynolds, S. P., Raymond, J. C., Winkler, P. F., Dyer, K. K., & Petre, R. 2003, *ApJ*, 586, 1162
- Lucek, S. G., & Bell, A. R. 2000, *MNRAS*, 314, 65
- Lyke, J. E., & Campbell, R. D. 2009, *ApJ*, 138, 1090
- Malkov, M., & Drury, L. 2001, *Reports on Progress in Physics*, 64, 429
- McLaughlin, D. B. 1945, *PASP*, 57, 69
- . 1960, in *Stellar Atmospheres*, ed. J.L. Greenstein. Chicago: University of Chicago Press
- Minkowski, R. 1958, *Rev. Mod. Phys.*, 30, 1048
- Miralda-Escudé, J., & Waxman, E. 1996, *ApJ*, 462
- Morlino, G., Bandiera, R., Blasi, P., & Amato, E. 2012, *ApJ*, 760, 137
- Morlino, G., Blasi, P., Bandiera, R., & Amato, E. 2013a, *A&A*, 558, A25
- Morlino, G., Blasi, P., Bandiera, R., Amato, E., & Caprioli, D. 2013b, *ApJ*, 768, 148
- Morse, J. A., et al. 1996, *AJ*, 112, 509
- Nagano, M. 2009, *New J. Phys.*, 11, 065012
- Nikolić, S., van de Ven, G., Heng, K., Kupko, D., Husemann, B., Raymond, J. C., Hughes, J. P., & Falcón-Barroso, J. 2013, *Science*, 340, 45
- Nomoto, K. 1982, *ApJ*, 253, 798
- O'Connell, L., Duffy, P., & Kirk, J. G. 1996, *A&A*, 309, 1002
- Ohira, Y. 2012, *ApJ*, 758, 97
- Paczyński, B. 1976, in Eggleton, P. P., Mitton, S., Whelan, J., eds. *Structure and Evolution of Close Binaries*. Kluwer, Dordrecht, p. 75.
- Pakmor, R., Röpkke, F. K., Weiss, A., & Hillebrandt, W. 2008, *A&A*, 489, 943
- Payne-Gaposchkin, C. 1957, *The Galactic Novae*, Amsterdam: North-Holland
- Perlmutter, S., et al. 1999, *ApJ*, 517, 565
- Petruk, O., et al. 2009, *MNRAS*, 393, 1034
- Porter, J. M., O'Brien, T. J., & Bode, M. F. 1998, *MNRAS*, 296, 943
- Rakowski, C. E., Ghavamian, P., & Hughes, J. P. 2003, *ApJ*, 590, 846
- Raymond, J. C. 1979, *APJS*, 39, 1
- Raymond, J. C., Blair, W. P., Fesen, R. A., & Gull, T. R. 1983, *ApJ*, 275, 636
- Raymond, J. C., Isenberg, P. A., & Laming, J. M. 2008, *ApJ*, 682, 408
- Raymond, J. C., Korreck, K. E., Sedlacek, Q. C., Blair, W. P., Ghavamian, P., & Sankrit, R. 2007, *ApJ*, 659, 1257
- Raymond, J. C., Vink, J., Helder, E. A., & de Laat, A. 2011, *ApJ*, 731

- Raymond, J. C., Winkler, P. F., Blair, W. P., Lee, J.-J., & Park, S. 2010, *ApJ*, 712, 901
- Reynolds, S. P. 2008, *ARA&A*, 46, 89
- Reynolds, S. P., & Ellison, D. C. 1992, *ApJ*, 399, L75
- Reynolds, S. P., & Keohane, J. W. 1999, *ApJ*, 525, 368
- Reynoso, E. M., Velázquez, P. F., Dubner, G. M., & Goss, W. M. 1999, *AJ*, 117, 1827
- Riess, A. G., et al. 1998, *AJ*, 116, 1009
- Rothenflug, R., Ballet, J., Dubner, G., Giacani, E., Decourchelle, A., & Ferrando, P. 2004, *A&A*, 425, 121
- Ruiz-Lapuente, P., Comeron, F., & Méndez, J., e. 2004, *Nature*, 431, 1069
- Schaefer, B. E., & Pagnotta, A. 2012, *Nature*, 481, 164
- Sedov, L. I. 1959, *Similarity and Dimensional Methods in Mechanics*, Academic Press, New York
- Sharp, R., & Birchall, M. N. 2010, *PASA*, 27, 91
- Silverman, J. M., et al. 2013, *ApJS*, 207, 3
- Smith, R. C., Kirshner, R. P., Blair, W. P., & Winkler, P. F. 1991, *ApJ*, 375, 662
- Smith, R. C., Raymond, J. C., & Laming, J. M. 1994, *ApJ*, 420, 286
- Sokolsky, P., & Thomson, G. B. 2007, *Journal of Physics G Nuclear Physics*, 34, 401
- Sollerman, J., Ghavamian, P., Lundqvist, P., & Smith, R. C. 2003, *A&A*, 407, 249
- Sparks, W. M. 1969, *ApJ*, 156, 569
- Spitzer, L. 1968, *Diffuse matter in space* (New York: Wiley)
- Stroman, W., & Pohl, M. 2009, *ApJ*, 696, 1864
- Taam, R. E. 1980, *ApJ*, 237, 142
- Tanaka, T., et al. 2008, *arXiv: 0806.1490v1*
- Tian, W. W., & Leahy, D. A. 2011, *ApJ*, 729, L15
- Tuohy, I. R., Dopita, M. A., Mathewson, D. S., Long, K. S., & Helfand, D. J. 1982, *ApJ*, 261, 473
- van Adelsberg, M., Heng, K., McCray, R., & Raymond, J. C. 2008, *ApJ*, 689, 1089
- van den Bergh, S. 1988, *ApJ*, 327, 156
- van den Heuvel, E. P. J., Bhattacharya, D., Nomoto, K., & Rappaport, S. A. 1992, *A&A*, 262, 97
- Vancura, O., et al. 1992, *ApJ*, 401, 220
- Vink, J. 2012, *Astron. Astrophys. Rev.*, 20, 49
- Vink, J., & Laming, J. M. 2003, *ApJ*, 584, 758
- Wade, R. A., Harlow, J. J. B., & Ciardullo, R. 2000, *PASP*, 112, 614
- Wagner, A. Y., Lee, J.-J., Raymond, J. C., Hartquist, T. W., & Falle, S. A. E. G. 2009, *ApJ*, 690, 1412
- Wang, B., & Han, Z. 2012, *arXiv:1204.1155v2*
- Warren, J. S., et al. 2005, *ApJ*, 634, 376

- Wentzel, D. G. 1974, *ARAA*, 12, 71
- Whelan, J., & Iben, I. J. 1973, *ApJ*, 186, 1007
- Williams, B. J., Borkowski, K. J., Ghavamian, P., Hewitt, J. W., Mao, S. A., Petre, R., Reynolds, S. P., & Blondin, J. M. 2013, *ApJ*, 770, 129
- Williams, R. E. 1992, *AJ*, 104, 725
- . 2012, arXiv:1208.0380
- Winkler, P. F., Gupta, G., & Long, K. S. 2003, *ApJ*, 585, 324
- Woosley, W. A., & Weaver, T. A. 1986, *ARA&A*, 24, 205
- Zel'dovich, Y. B., & Raizer, Y. P. 1966, *Physics of Shock Waves and High-Temperature Phenomena* (New York, Academic)